Advanced Coatings for Corrosion Protection

Edited by
Wolfram Fürbeth

Printed Edition of the Special Issue Published in *Materials*

www.mdpi.com/journal/materials

Advanced Coatings for Corrosion Protection

Advanced Coatings for Corrosion Protection

Editor

Wolfram Fürbeth

MDPI • Basel • Beijing • Wuhan • Barcelona • Belgrade • Manchester • Tokyo • Cluj • Tianjin

Editor
Wolfram Fürbeth
Frankfurt am Main
Germany

Editorial Office
MDPI
St. Alban-Anlage 66
4052 Basel, Switzerland

This is a reprint of articles from the Special Issue published online in the open access journal *Materials* (ISSN 1996-1944) (available at: https://www.mdpi.com/journal/materials/special_issues/advanced_coatings).

For citation purposes, cite each article independently as indicated on the article page online and as indicated below:

LastName, A.A.; LastName, B.B.; LastName, C.C. Article Title. *Journal Name* **Year**, *Volume Number*, Page Range.

ISBN 978-3-03943-921-8 (Hbk)
ISBN 978-3-03943-922-5 (PDF)

Contents

About the Editor

Wolfram Fürbeth has a diploma in Chemistry from the University of Dortmund and received a Ph.D. in Materials Sciences from the University of Erlangen-Nuremberg in 1997. He joined DECHEMA as a research scientist in 1997 and has been head of the corrosion research group since 2005. In 2012, he obtained a habilitation in Materials Technology at RWTH Aachen Technical University. He served as Adjunct Professor at RWTH in 2018, and since March 2017, he has been a member of the Institute Directorate of the DECHEMA Research Institute. Since 2017, he has served as Head of the Scientific Advisory Board of the German Corrosion Society, as well as Chairman of the European Federation of Corrosion Science and Technology Advisory Committee since 2017 and Chairman of Working Party Coatings since 2012.

materials

MDPI

Editorial

Special Issue: Advanced Coatings for Corrosion Protection

Wolfram Fürbeth

DECHEMA Research Institute, Theodor-Heuss-Allee 25, 60486 Frankfurt am Main, Germany; wolfram.fuerbeth@dechema.de; Tel.: +49-69-7564-398

Received: 29 July 2020; Accepted: 30 July 2020; Published: 1 August 2020

Abstract: Corrosion is an important issue in many industrial fields. Among others, coatings are by far the most important technology for corrosion protection of metallic surfaces. The special issue "Advanced Coatings for Corrosion Protection" has been launched as a means to present recent developments on any type of advanced coatings for corrosion protection. Fifteen contributions have been collected on metallic, inorganic, polymeric and nanoparticle enhanced coatings providing corrosion protection as well as partly other functionalities.

Keywords: metallic coatings; anodizing layers; passivation; polymeric coatings; laser cladding; PVD; superhydrophobic coatings; composite coatings

Corrosion is an important issue in many industrial fields. It leads to high economic losses of 3–4% of the GDP of an industrialized country year by year. Adequate corrosion protection is therefore essential in many applications. Among others, coatings are by far the most important technology for corrosion protection of metallic surfaces.

In the very traditional field of coatings for corrosion protection in the last years a deeper understanding of mechanisms of the protective action and corrosion mechanisms of and below protective coatings has been gained. This was necessary due to upcoming environmental and health issues for some well-established compounds used in former coating systems, e.g., lead or chromates, which have been banned from industrial application. This lead as well to a large amount of research in the field of advanced coating systems for corrosion protection.

This situation is the case for all the different types of protective coatings that are typically used. Novel metallic coatings, e.g., novel zinc alloys are under development, as well as novel pretreatment systems or passivating chemicals avoiding the use of chromates. The upcoming chemical nanotechnology fosters the development of hybrid or inorganic sol-gel coatings, as well as of nanoparticles and nanocapsules to be used as fillers in coating systems. This has also led, in recent years, to the development of novel self-healing and smart coatings. Furthermore, nowadays, bio-based substances are becoming increasingly used for organic coatings. Last but not least, new anodizing processes have also been developed in the frame of an increased use of light metals for light weight construction.

The special issue "Advanced Coatings for Corrosion Protection" has been proposed as a means to present recent developments on any of these types of advanced coatings for corrosion protection. Thus, 15 contributions have been collected on metallic, inorganic, polymeric and nanoparticle enhanced coatings providing corrosion protection as well as partly other functionalities.

Among all of them, inorganic coatings stand out for the number of contributions being submitted to this special issue; however, these are of many different types and for different applications. The thinnest but often quite effective type of an inorganic coating may be a passivating oxide layer. The most commonly used passivating agent to develop such an oxide layer is nitric acid. Lara-Banda et al. investigated an environmentally friendly alternative for the passivation of 15-5 and 17-5PH stainless

steels based on citric acid [1]. It could be shown that, for both types of steel, the passive layer formed in citric acid as passivating solution had very similar characteristics to that formed with nitric acid.

Much thicker oxide layers can be obtained by anodizing techniques especially on light metals. Besides the conventional anodizing treatment at rather low voltages plasma-electrolytic oxidation (PEO) or micro arc oxidation (MAO), leading to ceramic oxide layers, has become an increasingly important alternative, being the topic of three contributions in this special issue [2–4]. Yao et al. prepared different MAO coatings on the magnesium alloy AZ91D [2]. It was found that especially a brown coating doped with Cu is able to significantly reduce the corrosion of magnesium parts in marine environments. Magnesium alloys to be used as biodegradable implant materials are the background of the paper by Anawati et al. [3]. Therefore, they investigated not only the corrosion resistance of PEO coatings, but also their ability to form bone mineral apatite. It was concluded that the alloying element Ca should be limited to 1 wt% as the excess tended to degrade the corrosion resistance and apatite-forming ability of the PEO coating. Kyziol et al. investigated the influence of MAO coatings on the stress corrosion cracking susceptibility of an AlMg6 alloy [4]. The pores in the MAO coating were insignificant and of limited depth. Therefore, the coating could increase the corrosion resistance.

Furthermore, inorganic coatings may be obtained from metal carbides [5], nitrides [6] or borides [7]. Jiang et al. used carburizing by a spark plasma sintering technique to enhance the erosion-corrosion resistance of tungsten in flowing coolant water [5]. W-Cr-C clad tungsten showed a different corrosion behavior than bare tungsten. Ti2AlN coatings were obtained by physical vapor deposition on ferritic steels and submitted to oxidation at a temperature of 700 °C by Gröner et al. [6]. The oxide scale of α-alumina was able to reduce the permeability for hydrogen significantly. Hu et al. obtained boride cermet coatings on carbon steel by a laser cladding process to improve the corrosion and wear resistance [7].

Polymeric coatings are widely used in corrosion protection and several contributions deal with this type of coatings as well [8–12]. Aging of the coating in terms of chain scission and phase separation may change the protective properties with time, as shown by Che et al. for polyurea coatings in marine atmosphere [8]. A wide variety of polymeric and hybrid systems can be chosen for protective coatings. Miela et al. showed how materials analysis and molecular dynamics simulation may help to identify the best performing coating system for erosion and corrosion protection of hydraulic water valves [9]. Polymeric coatings may also be used to add further functionalities to a barrier-type protective coating. As such, superhydrophobic properties were generated by Ou et al. on a zinc coating [10] and by Zhang et al. on the aluminum alloy AA5083 [11], providing water-repelling and long-term corrosion resistant surfaces. A very classical application of organic coatings is the insulation of buried pipelines. The paper by Hong et al. addresses this application, focusing on the additional cathodic protection design for a pre-insulated pipeline in a district heating system using computational simulation [12].

Finally, metallic coatings are widely used as noble barrier layers or as sacrificial layers providing cathodic protection to the substrate. One of the latter has been described by Tong et al. [13]. They produced a ZnAl diffusion layer on carbon steel by a mechanical energy aided diffusion method and characterized its corrosion behavior. On the other hand, barrier-type coatings may be reinforced by incorporation of nanoparticles into the coating matrix. Xu et al. demonstrated that the mechanical properties and the corrosion resistance of an aluminum foam can be improved by the electrodeposition of a NiMo coating that has been reinforced by SiC/TiN nanoparticles [14]. Furthermore, Fu et al. studied the effect of doping a NiFeCoP coating with cerium dioxide nanoparticles [15]. With an increased concentration of nano-CeO_2 in the composite coating, its corrosion resistance increased as well.

Conflicts of Interest: The authors declare no conflict of interest.

References

1. Lara-Banda, M.; Gaona-Tiburcio, C.; Zambrano-Robledo, P.; Delgado-E, M.; Cabral-Miramontes, J.; Nieves-Mendoza, D.; Maldonado-Bandala, E.; Estupiñan-López, F.; Chacón-Nava, J.G.; Almeraya-Calderón, F. Alternative to Nitric Acid Passivation of 15-5 and 17-4PH Stainless Steel Using Electrochemical Techniques. *Materials* **2020**, *13*, 2836. [CrossRef] [PubMed]
2. Yao, Y.; Yang, W.; Liu, D.; Gao, W.; Chen, J. Preparation and Corrosion Behavior in Marine Environment of MAO Coatings on Magnesium Alloy. *Materials* **2020**, *13*, 345. [CrossRef] [PubMed]
3. Anawati, A.; Asoh, H.; Ono, S. Corrosion Resistance and Apatite-Forming Ability of Composite Coatings formed on Mg-Al-Zn-Ca Alloys. *Materials* **2019**, *12*, 2262. [CrossRef] [PubMed]
4. Kyziol, L.; Komarov, A. Influence of Micro-Arc Oxidation Coatings on Stress Corrosion of AlMg6 Alloy. *Materials* **2020**, *13*, 356. [CrossRef] [PubMed]
5. Jiang, Y.; Yang, J.; Xie, Z.; Fang, Q. Enhanced Erosion–Corrosion Resistance of Tungsten by Carburizing Using Spark Plasma Sintering Technique. *Materials* **2020**, *13*, 2719. [CrossRef] [PubMed]
6. Gröner, L.; Mengis, L.; Galetz, M.; Kirste, L.; Daum, P.; Wirth, M.; Meyer, F.; Fromm, A.; Blug, B.; Burmeister, F. Investigations of the Deuterium Permeability of As-Deposited and Oxidized Ti2AlN Coatings. *Materials* **2020**, *13*, 2085. [CrossRef] [PubMed]
7. Hu, Z.; Li, W.; Zhao, Y. The Effect of Laser Power on the Properties of M3B2-Type Boride-Based Cermet Coatings Prepared by Laser Cladding Synthesis. *Materials* **2020**, *13*, 1867. [CrossRef] [PubMed]
8. Che, K.; Lyu, P.; Wan, F.; Ma, M. Investigations on Aging Behavior and Mechanism of Polyurea Coating in Marine Atmosphere. *Materials* **2019**, *12*, 3636. [CrossRef] [PubMed]
9. Mlela, M.K.; Xu, H.; Sun, F.; Wang, H.; Madenge, G.D. Material Analysis and Molecular Dynamics Simulation for Cavitation Erosion and Corrosion Suppression in Water Hydraulic Valves. *Materials* **2020**, *13*, 453. [CrossRef] [PubMed]
10. Ou, J.; Zhu, W.; Xie, C.; Xue, M. Mechanically Robust and Repairable Superhydrophobic Zinc Coating via a Fast and Facile Method for Corrosion Resisting. *Materials* **2019**, *12*, 1779. [CrossRef] [PubMed]
11. Zhang, B.; Xu, W.; Zhu, Q.; Yuan, S.; Li, Y. Lotus-Inspired Multiscale Superhydrophobic AA5083 Resisting Surface Contamination and Marine Corrosion Attack. *Materials* **2019**, *12*, 1592. [CrossRef] [PubMed]
12. Hong, M.S.; So, Y.S.; Kim, J.G. Optimization of Cathodic Protection Design for Pre-Insulated Pipeline in District Heating System Using Computational Simulation. *Materials* **2019**, *12*, 1761. [CrossRef] [PubMed]
13. Tong, J.; Liang, Y.; Wei, S.; Su, H.; Wang, B.; Ren, Y.; Zhou, Y.; Sheng, Z. Microstructure and Corrosion Resistance of Zn-Al Diffusion Layer on 45 Steel Aided by Mechanical Energy. *Materials* **2019**, *12*, 3032. [CrossRef] [PubMed]
14. Xu, Y.; Ma, S.; Fan, M.; Zheng, H.; Chen, Y.; Song, X.; Hao, J. Mechanical and Corrosion Resistance Enhancement of Closed-Cell Aluminum Foams through Nano-Electrodeposited Composite Coatings. *Materials* **2019**, *12*, 3197. [CrossRef] [PubMed]
15. Fu, X.; Ma, W.; Duan, S.; Wang, Q.; Lin, J. Electrochemical Corrosion Behavior of Ni-Fe-Co-P Alloy Coating Containing Nano-CeO_2 Particles in NaCl Solution. *Materials* **2019**, *12*, 2614. [CrossRef] [PubMed]

materials

MDPI

Article

Alternative to Nitric Acid Passivation of 15-5 and 17-4PH Stainless Steel Using Electrochemical Techniques

María Lara-Banda [1], Citlalli Gaona-Tiburcio [1], Patricia Zambrano-Robledo [1], Marisol Delgado-E [1], José A. Cabral-Miramontes [1], Demetrio Nieves-Mendoza [2], Erick Maldonado-Bandala [2], Francisco Estupiñan-López [1], José G. Chacón-Nava [3] and Facundo Almeraya-Calderón [1,*]

[1] Universidad Autonoma de Nuevo Leon, FIME—Centro de Investigación e Innovación en Ingeniería Aeronáutica (CIIIA), Av. Universidad s/n. Ciudad Universitaria, San Nicolás de los Garza, Nuevo León 66455, Mexico; marialarabanda@yahoo.com.mx (M.L.-B.); citlalli.gaonatbr@uanl.edu.mx (C.G.-T.); patricia.zambranor@uanl.edu.mx (P.Z.-R.); marisol__1706@hotmail.com (M.D.-E); jose.cabralmr@uanl.edu.mx (J.A.C.-M.); francisco.estupinanlp@uanl.edu.mx (F.E.-L.)

[2] Facultad de Ingeniería Civil, Universidad Veracruzana, Xalapa, Veracruz 91000, Mexico; dnieves@uv.mx (D.N.-M.); eemalban@gmail.com (E.M.-B.)

[3] Centro de Investigación en Materiales Avanzados (CIMAV), Miguel de Cervantes 120, Complejo Industrial Chihuahua, Chihuahua, Chih 31136, Mexico; jose.chacon@cimav.edu.mx

* Correspondence: falmeraya.uanl.ciiia@gmail.com

Received: 5 May 2020; Accepted: 8 June 2020; Published: 24 June 2020

Abstract: Increasingly stringent environmental regulations in different sectors of industry, especially the aeronautical sector, suggest the need for more investigations regarding the effect of environmentally friendly corrosion protective processes. Passivation is a finishing process that makes stainless steels more rust resistant, removing free iron from the steel surface resulting from machining operations. This results in the formation of a protective oxide layer that is less likely to react with the environment and cause corrosion. The most commonly used passivating agent is nitric acid. However, it is know that high levels of toxicity can be generated by using this agent. In this work, a study has been carried out into the electrochemical behavior of 15-5PH (precipitation hardening) and 17-4PH stainless steels passivated with (a) citric and (b) nitric acid solutions for 60 and 90 min at 49 °C, and subsequently exposed to an environment with chlorides. Two electrochemical techniques were used: electrochemical noise (EN) and potentiodynamic polarization curves (PPC) according to ASTM G199-09 and ASTM G5-13, respectively. The results obtained indicated that, for both types of steel, the passive layer formed in citric acid as passivating solution had very similar characteristics to that formed with nitric acid. Furthermore, after exposure to the chloride-containing solution and according with the localization index (LI) values obtained, the stainless steels passivated in citric acid showed a mixed type of corrosion, whereas the steels passivated in nitric acid showed localized corrosion. Overall, the results of the R_n values derived show very low and similar corrosion rates for the stainless steels passivated with both citric and nitric acid solutions.

Keywords: stainless steel; passivated; electrochemical noise; precipitation hardening

1. Introduction

Corrosion in the aeronautical industry remains a major problem that directly affects safety, economic, and logistical issues. Stainless steel alloys have found increasing application in aircraft components that require great strength but can handle the increased weight. The high corrosion and temperature resistances found in stainless steel in harsh environments make it suitable for a range of

aircraft parts such as fasteners, actuators and landing gear components [1–3]. Passivation is a chemical process to remove surface contamination, i.e., small particles of iron-containing shop dirt and iron particles from cutting tools that can act as initiation sites for corrosion. This process also can remove sulfides exposed on the surface of free-machining stainless alloys. In other words, by chemically removing free contaminants from the surface of stainless steel, the passivation process adds a thin oxide layer. More chromium available from a clean surface means a thicker chromium oxide layer at the top of the stainless steel surface. Moreover, this chemically non-reactive surface means more protection against corrosion [4–10].

Precipitation hardening (PH) stainless steels (SS) are a family of corrosion resistant alloys some of which can be heat treated to provide tensile strengths of 850 to 1700 MPa and yield strengths of 520 MPa to over 1500 MPa. These alloys contain 11–18% chromium, 3–4% nickel, and smaller counts of additional metals, including aluminum, niobium, molybdenum, titanium and tungsten. Nevertheless, chromium is the alloying element responsible for the formation of the passive film [11–14]. The family of precipitation hardening stainless steels can be divided into three main types—low carbon martensitic, semi-austenitic and austenitic. These stainless steels are widely used in aerospace structural applications due to its good corrosion resistance and high strength and toughness obtained by the formation of precipitates from age-hardening treatments. Previous investigations on aeronautical-aerospace sector has shown that 15-5PH and 17-4PH steels have good corrosion resistance regarding other stainless steels [15–20].

Back in 1997, the specification QQ-P-35 for passivation of stainless steel parts was withdrawn, and replaced by specification SAE-QQ-P-35, also withdrawn in 2005. The latter was replaced by specification ASTM A967-17. This indicates that both, citric and nitric acid can be used as passivating agents for stainless steels. To be effective, the nitric acid must be highly concentrated. However, many questions has been done regarding the production of harmful to health toxic vapors generated by the use of nitric acid in passivation baths [21,22]. On the other hand, citric acid is a biodegradable alternative that does no generate hazardous waste. Although the citric acid benefits as a passivating agent are well-established, technical information about the passivation process is scarce [23,24]. In 2003, Boeing Company evaluate the use of citric acid as an alternative for steel passivation in the aeronautic industry [6]. In 2008, the National Aeronautics and Space Administration (NASA) began a research program focused on the evaluation of the use of nitric acid in the passivation process of welded parts, using the salt chamber technique [10]. Later, NASA evaluated the use of citric acid on specimens exposed under atmospheric corrosion conditions using adherence tests [21].

It is well know that aggressive ions, especially chloride ions Cl-, affect the protecting nature of the passive film on stainless steels causing its breakdown. This leads to localized attack, mainly pitting corrosion [25,26]. In the study of corrosion mechanisms, a number of electrochemical techniques such as potentiodynamic, potentiostatic, and galvanostatic polarization tests, electrochemical impedance (EIS) and electrochemical noise (EN) are widely used. For instance, the evaluation of important parameters such as passive range, pitting potentials, corrosion rates and transpassive regions are studied using potentiodynamic polarization curves (PPC). Bragaglia et al. [27] studied the potentiodynamic polarization behavior of passivated citric and nitric acid baths) and unpassivated AISI 304 stainless steel samples after 1 h in 3.5 wt. % NaCl solution. The passivation treatment largely increased the pitting potential, particularly in the case of nitric acid. After 24 h exposure, electrochemical behavior for the nitric acid and the citric acid passivated samples were almost identical.

Electrochemical noise is a technique that does not alter the natural state of the system, since no external disturbance is applied [28]. This technique reflect random or spontaneous events of current and/or potential fluctuations. Under open-circuit conditions, these fluctuations appear to be related to variations in the rates of anodic and cathodic reactions causing small transients as a result of stochastic processes such as breakdown and repassivation of passive films and formation and propagation of pits. The fluctuations of current between two nominally identical electrodes as well as their potential versus a reference electrode (three electrode system) are recorded as time series, and by using several

methods to analyze noise data, an understanding of the corrosion process occurring can be determined. The EN data can be analyzed by several methods. Perhaps the most commonly used are those related to frequency domain (power density spectral or spectral analysis), time domain (statistical methods as skewness, kurtosis, localization index (LI), and the variation of signal amplitude with time) and time-frequency domains [29,30]. Suresh and Mudali [31] studied the corrosion of UNS S30403 stainless steel in 0.05 M ferric chloride ($FeCl_3$) by spectral, statistical, and wavelet methods to deduce the corrosion mechanism. They found a good correlation of roll-off slopes derived from power spectral analysis and statistical parameters such as standard deviation, localization index (LI), and kurtosis with pitting as the corrosion mechanism. These authors reported a localization index (LI) in the range from 0.7 and 1. LI values of 0.1 to 1 has been attributed to pitting corrosion and hence the mechanism of corrosion was attributed to pitting attack [X]. Ortiz Alonso et al. [32], studied the stress corrosion cracking (SCC) behavior of a supermartensitic stainless steel by EN. They found that the LI value increased during the straining of specimens (in the range from 0.1 to 1), indicating the presence of localized events such as pits or cracks regardless of the susceptibility of the steel to stress corrosion cracking. In spite of some of its drawbacks, other studies also have found a good relationship between the LI parameter and pitting corrosion [33,34]

The aim of the present work is the study of the electrochemical behavior of 15-5PH and 17-4PH stainless steels passivated in nitric and citric acid and exposed to a 5 wt. % NaCl aqueous solution by PPC and EN.

2. Materials and Methods

2.1. Materials and Samples Preparation

The materials used in this work were 15-5PH and 17-4PH stainless steels used in the as received condition. The chemical composition of these steels was obtained by atomic absorption spectrometry, see Table 1.

Table 1. Chemical composition of the used stainless steels (wt. %).

Stainless Steel	Elements										
	C	**Mn**	**P**	**S**	**Si**	**Cr**	**Ni**	**Mo**	**Nb**	**Cu**	**Fe**
15-5PH	0.024	0.817	0.007	0.004	1.569	14.410	3.937	0.383	0.308	3.558	Bal.
17-4PH	0.022	0.827	0.023	0.029	1.637	15.204	3.050	0.340	0.144	3.908	Bal.

Stainless steel samples were machined as cylindrical coupons, according to ASTM A380-17 [35]. The specimens were polished with SiC grit paper till 4000 grade, followed by ultrasonic cleaning in ethanol and deionized water for about 10 min each.

2.2. Passivation Process

The passivation process was carried out under the specification ASTM A967-17 [36]. Gaydos et al. [21] reported that extended passivation treatments give a better protection against corrosion for a series of stainless steels. In the present work, two passivation baths (a) nitric acid (20%v) and (b) citric acid (15%v) solutions were used. A constant temperature of 49 °C was maintained along the passivation process. Specimens were immersed in the solutions for 60 and 90 min. Table 2 show the passivation exposure conditions for each type of steel.

Table 2. Passivation at a temperature of 49 °C.

Stainless Steel	Citric Acid ($C_6H_8O_7$)		Nitric Acid (HNO_3)	
	Passivated Time (min)			
	60	90	60	90
15-5PH	X	X	X	X
17-4PH	X	X	X	X

2.3. Electrochemical Techniques

In order to assess the corrosion behavior of passivated specimens (exposed area 4.46 cm^2), two electrochemical techniques were used: EN and PPC. The electrolyte was a 5 wt. % NaCl aqueous solution and all tests were carried out at room temperature.

2.3.1. Electrochemical Noise (EN)

This technique was carried out under ASTM G199-09 standard [37]. The experimental setup for EN measurements is schematically depicted in Figure 1. Here, two nominally identical electrodes (passivated stainless steels) as working electrodes (WE1 and WE2) were connected to measure the electrochemical current noise (ECN), whereas the electrochemical potential noise (EPN) was measured by connecting one working electrode to a saturated calomel reference electrode.

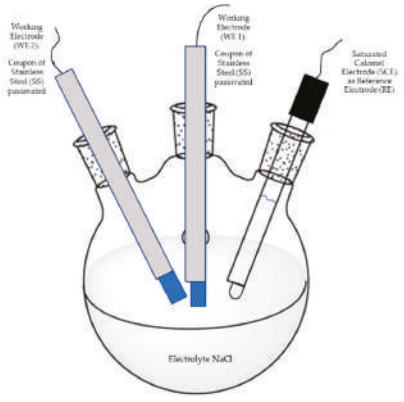

Figure 1. Experimental set up for electrochemical noise (EN) measurements.

The current and potential electrochemical noise was monitored as a function of time under open circuit condition for each particular electrode–electrolyte combination, using a Gill-AC (Alternating Current) potentiostat/galvanostat/ZRA (Zero Resistance Ammeter) from ACM Instruments. Electrochemical noise measurements started one after the open circuit potential stabilized (about 1 h after immersion in the electrolyte). Since the EN technique involves mostly non-stationary signals, trend removal was carried out. In each experiment, 1024 data were measured with a scanning speed of 1 data/s. The time series in current and potential were visually analyzed to interpret the signal transients and define the behavior of the frequency and amplitude of the fluctuations as a function of time. Resistance noise (*Rn*) data were obtained and used to calculate the corrosion rate according to Equation (1),

$$R_n = \frac{\sigma_E}{\sigma_I} \quad (1)$$

where σ_E is the standar deviation of potential noise, and σ_I is the standar deviation of current noise after trend removal. The LI, defined by Equation (2), is a parameter used to estimate, as a first approximation,

the type of corrosion occurring in a given system [38–40]. LI values approaching zero, indicates uniform (general) corrosion; values in the range from 0.01 to 0.1 indicates mixed corrosion, whereas values from 0.1 to 1 correspond to pitting corrosion.

$$IL = \frac{\sigma_I}{I_{RMS}} \tag{2}$$

where I_{RMS} is the root mean square value of the corrosion current noise.

2.3.2. Potentiodynamic Polarization Curves (PPC)

This technique was carried out according to ASTM G5-13 [41] and ASTM G102-89 standards [42]. Here, a conventional three-electrode cell configuration was used, see Figure 2.

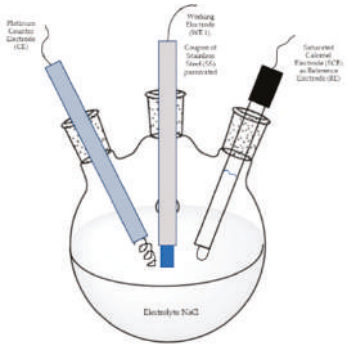

Figure 2. Conventional three-electrode cell configuration used in the potentiodynamic polarization curves (PPC) tests.

Potentiodynamic polarization curves were recorded in 5 wt. % NaCl aqueous solution at room temperature in a Gill-AC potentiostat/galvanostat from ACM Instruments. The potential scan was carried out from −1000 mV to +1200 mV, at a scan rate of 60 mV/min. A saturated calomel electrode (SCE) and a platinum wire were used as reference electrode and counter electrode, respectively. The working electrode (passivated sample) was hold for about 1 h at open circuit potential before tests.

3. Results

3.1. Electrochemical Noise

Figures 3 and 4 show the current and potential time series recorded for 15-5PH and 17-4PH stainless steel passivated in citric and nitric acid solutions at 60 and 90 min, respectively. Figure 2 shows that under passivation conditions at 60 and 90 min in citric acid, the passivated 15-5PH and 17-4PH stainless steel specimens did not present current fluctuations in time, this indicating that the specimens are in passive conditions; also, the potential noise signals remained constant without fluctuations in time (Figure 3a). The 17-4PH sample passivated for 60 min has higher current demand with low amplitude and high frequency transients, while the potential for this alloy has more active potentials (Figure 3d). For both types of stainless steel, the current-potential time series after 1000 s it has a tendency towards passivation.

Windowing analysis of electrochemical current noise between 0 and 200 s (Figure 3b) show no current increase for the 15-5PH samples passivated at 60 and 90 min. The 17-4PH steel passivated for 60 min, shows some transients of low amplitude and frequency, while for the 90 min passivation treatment only one anodic transient of high amplitude and low frequency was recorded 20 s after the start of the test. Another windowing analysis of current noise signal was performed between 900 and

1024 s (Figure 3c). For both types of stainless steel, irrespective of passivation conditions, no current fluctuations were observed. In some way, this behavior indicates stability of the passive layer.

For both types of stainless steel under passivation conditions, windowing analysis from 0 to 200 s and from 900 to 1024 s did not show frequency or amplitude transients, confirming the stability of potentials (Figure 3e,f). It is worth noting that the potentials of the 17-4PH samples are more negative than those recorded for the 15-5PH samples.

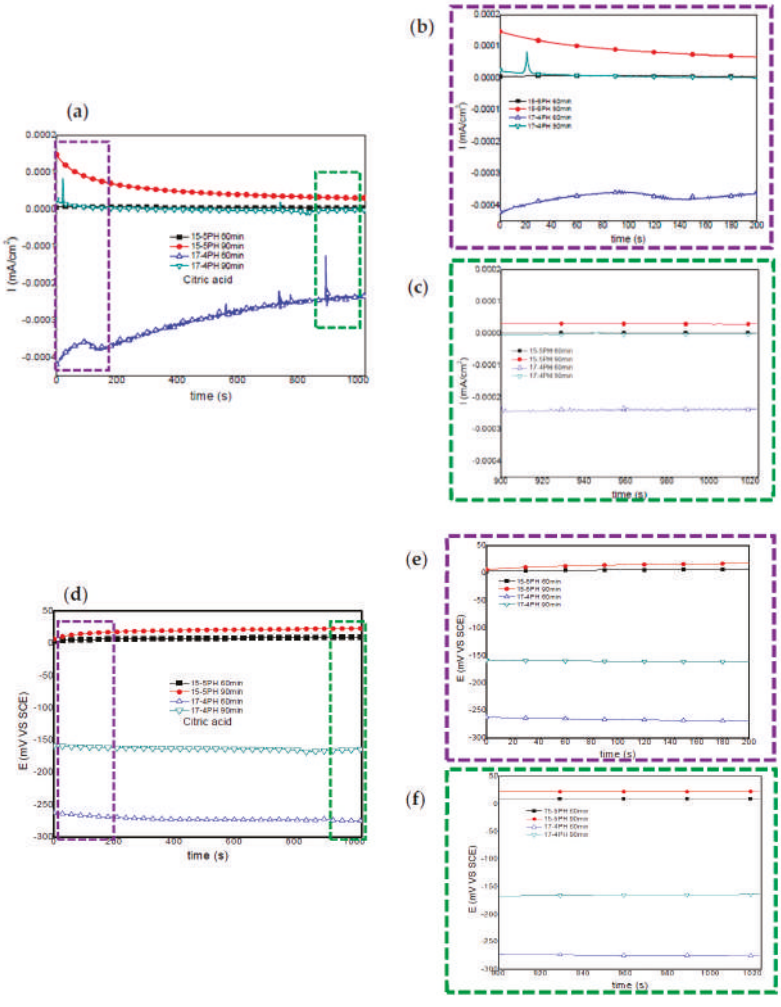

Figure 3. Electrochemical current and potential noise-time series for 15-5PH and 17-4PH samples passivated in citric acid at 49 °C, exposed in a 5 wt.% NaCl solution (**a**,**d**). Windowing of electrochemical current noise (ECN) from 0–200 and 900–1024 s (**b**,**c**); windowing of electrochemical potential noise (EPN) from 0–200 and 900–1024 s (**e**,**f**).

For the 15-5PH and 17-4PH stainless steels passivated in nitric acid, Figure 4 shows the current and potential noise time series recorded. The 17-4PH sample passivated for 90 min, show a decreases in current noise as a function of time; while the potential noise shifts to noble values, indicating stability of the passive layer. A similar behavior was observed for the 15-5PH samples passivated for 60 min.

The 15-5PH and 17-4PH samples passivated for 90 and 60 min show a small current demand during the first 300 and 700 s. Afterwards, no significant current or potential fluctuations (transients) were recorded, indicating stabilization of the passive layer (Figure 4a,d).

Windowing analysis of electrochemical current noise between 0 and 200 s (Figure 4b), shows a small increase in in current demand for the 15-5PH and 17-4PH samples passivated for 90 and 60 min, respectively (Figure 4b). From 900 to 1024 s, a windowing analysis of current noise did not show current transients (Figure 4c). Windowing analysis from 0 to 200 s and from 900 to 1024 s did not show frequency or amplitude transients, confirming the stability of potentials (Figure 4e,f). It is interesting to note that, irrespective of the time of passivation treatment, more noble potentials were attained by the 15-5PH stainless steel, in comparison with the 17-4PH steel.

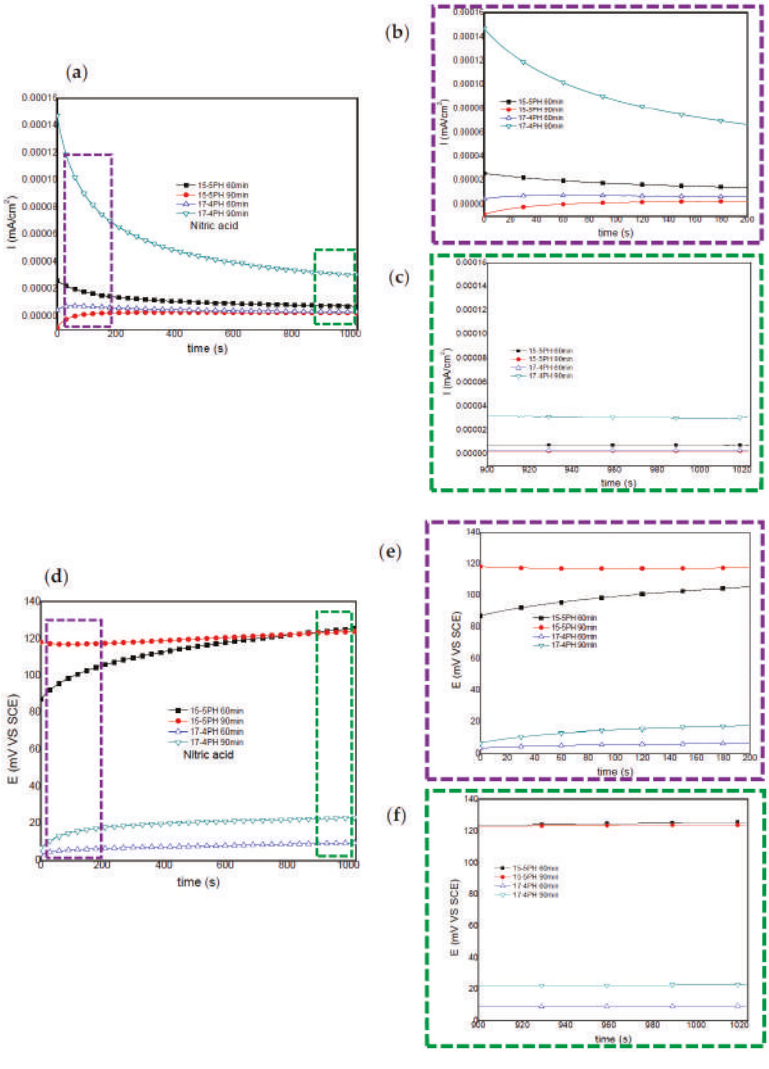

Figure 4. Electrochemical current and potential noise-time series for 15-5PH and 17-4PH samples passivated in nitric acid at 49 °C, exposed in a 5 wt. % NaCl solution (**a**,**d**). Windowing of ECN from 0–200 and 900–1024 s (**b**,**c**); windowing of EPN from 0–200 and 900–1024 s (**e**,**f**).

The EN parameters derived from the statistical analysis of current and potential time series measurements are shown in Table 3. The i_{corr} value obtained from noise resistance (*Rn*) for the samples passivated in citric acid is in the order of 10^{-4} (mA/cm^2), whereas for the samples passivated in nitric, i_{corr} values about 10^{-5} (mA/cm^2) were recorded. The very low values for i_{corr} obtained for both passivating agents indicate that citric acid could be a potential replacement for nitric acid as passivating agent. Information regarding the type of corrosion that could be occurring is given by the LI parameter. As can be seen from Table 3, the stainless steels passivated in citric acid solution mainly show a mixed corrosion type, whereas the stainless steels passivated in nitric acid solution the LI values indicates localized corrosion.

Table 3. Electrochemical noise parameters at various conditions in 5 wt. % NaCl at 49 °C.

Passivated Agent	Stainless Steel	Time (min)	*Rn* (Ω/cm^2)	i_{corr} (mA/cm^2)	LI	Corrosion Type
Citric acid	15-5PH	60	8.01×10^{-4}	6.49×10^{-4}	0.0862	Mixed
		90	5.00×10^{-5}	1.04×10^{-4}	0.0308	Mixed
	17-4PH	60	5.76×10^{-4}	4.51×10^{-4}	0.2492	Localized
		90	3.27×10^{-5}	1.59×10^{-4}	0.0900	Mixed
Nitric acid	15-5PH	60	2.35×10^{-6}	1.1×10^{-5}	0.1871	Localized
		90	1.51×10^{-6}	1.72×10^{-5}	0.1077	Localized
	17-4PH	60	1.03×10^{-6}	2.52×10^{-5}	0.1485	Localized
		90	1.34×10^{-6}	1.94×10^{-4}	0.1727	Localized

3.2. Potenciodynamic Polarization

The corrosion kinetic behaviour using potentiodynamic polarization can be observed through cathodic and anodic reactions in polarization curves. Corrosion rate in terms of penetration (mm/sec) is one of the main parameters obtained by potentiodynamic polarization curves, according to Faraday's law (Equation (3)) [40,42–44].

$$Corrosion\ rate = K_1 \frac{i_{corr}}{\delta} E.W \quad (3)$$

The potentiodynamic polarization curves obtained for the 15-5PH and 17-4PH stainless steels passivated for 60 min and 90 min in (a) citric acid and (b) nitric acid, and immersed in 5 wt. % NaCl solution are shown in Figure 5.The results for citric acid passivation (Figure 5a) show that the lower E_{corr} value was recorded for the 17-4PH sample passivated for 90 min, while the 15-5PH sample passivated for 90 min has the highest E_{corr}. Pitting potentials (E_{pitt}) were in the range from 42 mV up to 147 mV. This last value was recorded for the 15-5PH steel passivated for 90 min, this being the best treatment for nitric acid passivation, also corroborated by the lower corrosion rate obtained. For nitric acid passivation conditions, Figure 4b show that the E_{pitt} was largely improved, particularly for the 15-5PH steel passivated for 90 min, and also has the lower corrosion rate in this condition. The lower E_{pitt} value recorded was given by the 17-4PH passivated during 90 min, also giving the highest corrosion rate. On the whole, irrespective of the type of PH stainless steel used, the nitric acid passivation treatment largely increases the pitting potentials compared with the citric acid treatment.

The parameters (E_{corr}, E_{pitt}, $i_{corr,}$ and corrosion rate (C.R.)) obtained from the polarization potentiodynamic curves are summarised in Table 4. Very low values of corrosion rate (within the same order of magnitude) were recorded for both 15-5PH and 17-4PH steels, irrespective of the passivation treatment conditions.

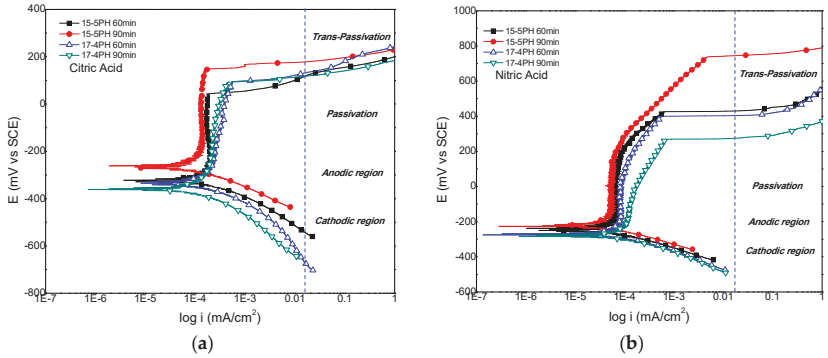

Figure 5. Potentiodynamic polarization curves of 15-5PH and 17-4PH stainless steel passivated in (**a**) citric acid and (**b**) nitric acid, exposed in a 5 wt. % NaCl solution at 49 °C.

Table 4. Potentiodynamic polarization parameters in stainless steels passivated at 49 °C, in 5 wt. % NaCl.

Passivated Agent	Stainless Steel	Time (Min)	E_{corr} (mV)	E_{pit} (mV)	i_{corr} (mA/cm^2)	C. R. (mm/Year)
Citric Acid	15-5PH	60	−323	42	5.26×10^{-5}	5.54×10^{-7}
		90	−266	147	4.50×10^{-5}	4.75×10^{-7}
	17-4PH	60	−335	91	9.22×10^{-5}	9.64×10^{-7}
		90	−360	97	5.38×10^{-5}	5.63×10^{-7}
Nitric Acid	15-5PH	60	−228	467	2.16×10^{-5}	2.28×10^{-7}
		90	−228	765	2.27×10^{-5}	2.39×10^{-7}
	17-4PH	60	−271	439	3.51×10^{-5}	3.67×10^{-7}
		90	−279	323	4.41×10^{-5}	4.61×10^{-7}

4. Discussion

Several EN procedures correlating timed dependent fluctuation of current and potential during the corrosion process have been used to indicate the type of corrosion occurring. For instance, it is well recognized that the main source of electrochemical noise is the passive film breakdown process and repassivation process [45–49].

For the passivated 15-5PH and 17-4PH stainless steels in this work, the electrochemical potential time series recorded under nitric acid passivation show a passive region from 0 to 120 mV, whereas for citric acid passivation conditions, the passive region goes from −300 to 25 mV. Thus, passivation in nitric acid occurs at more positive (noble) potentials that in citric acid solutions. To some extent, this might indicate that the passive layer is more stable at more noble potentials [25]. Hence, higher corrosion resistance (*Rn*) values could be expected for passivation in nitric acid solutions [50]. To some extent, the results of *Rn* in Table 3 confirm this.

As a first approach, to assess the more likely type of corrosion occurring for the 15-5PH and 17-4PH stainless steels passivated in both citric acid and nitric acid solutions, the LI parameter was evaluated from the electrochemical noise data, and was found to be in the range from 0.03 to 0.249, see Table 3. From the LI values obtained for each passivating bath, the corrosion type occurring in citric acid passivation conditions can be attributed to mixed corrosion, whereas for nitric acid passivation conditions, the corrosion type could be attributed to pitting corrosion. LI has been used by several research groups for determining corrosion types under several conditions [51–56].

The use of LI to determine corrosion types has been the subject of many discussions among investigators on the data treatment and interpretations using LI [29,30,38,57–59]. Since the mean of the noise data (detrended) would be negligible, the standard deviation and root mean square current

noise would converge to the same value and, hence, the LI evaluated from the data would be unity, irrespective of the corrosion type. Cottis [60] indicated that LI for identification of localization of corrosion is unduly influenced by the mean current and hence less reliable. In the present study, and as a first attempt, the LI parameter was estimated. Of course, it is recognized that in the study of stainless steels such as those in the present work, investigation of procedures based on the frequency domain and time-frequency domain deserves further attention.

The potentiodynamic polarization curves show passivation behavior for the 15-5PH and 17-4PH steels passivated in citric and nitric acid solutions. The passive zones on stainless steels are commonly made up of primary and secondary zones, which are formed before and after transpassivation, respectively. Potentials above E_{pitt} causes a rapid dissolution [61–63]. The passive zone involves the formation of iron and chromium oxide films [61,64,65]. Hence, selective dissolution on the surface of the alloy generates a surface enrichment of Cr^{3+} giving rise to $Cr(OH)_3$, as shown in Equation (4). Further dissolution of the hydroxide leads to the formation of a continuum layer of Cr_2O_3, according Equation (5) [66,67].

$$Cr^{3+} + 3OH^- \rightarrow Cr(OH)_3 + 3e^- \quad (4)$$

$$Cr(OH)_3 + Cr + 3OH^- \rightarrow Cr_2O_3 + 3H_2O + 3e^- \quad (5)$$

It has been argued that the anodic reactions during the film growth period are mainly from the oxidation of iron and chromium The following equations indicate the oxidation reactions of iron [68]:

$$3Fe + 8OH^- \rightarrow Fe_3O_4 + 4H_2O + 8e^- \quad (6)$$

$$2Fe_3O_4 + 2OH^- + 2H_2O \rightarrow 6FeOOH + 2e^- \quad (7)$$

$$2Fe_3O_4 + 2OH^- \rightarrow 3Fe_2O_3 + H_2O + 2e^- \quad (8)$$

For the nitric acid passivation treatment, the transpassive region is above 200 mV vs. ECS, whereas for citric acid passivation conditions, the transpassive region is above 50 mV vs. ECS. The passive film formed under nitric acid passivation conditions has higher E_{pitt} values, in comparison with the E_{pitt} values obtained under citric acid passivation conditions. This fact can be seen as a potential disadvantage for the citric acid treatment. Nevertheless, the corrosion rates obtained for both passivation treatments (Table 4) are very low and similar. Thus, for the PH stainless steel used in this work, citric acid passivation treatments can be as effective as nitric acid passivation treatments.

5. Conclusions

In this work, samples of 15-5PH and 17-4PH stainless steel were passivated in (a) citric acid and (b) nitric acid baths and exposed in a 5 wt. % NaCl solution. Their electrochemical behavior was studied by electrochemical noise and potentiodynamic polarization.

EN results show that, for citric solution passivation baths, the stabilization of the passive layer occurs at more active potentials compared to the stabilization potentials for nitric acid passivation baths. From noise resistance (*Rn*) data, very low corrosion rate values were derived for the PH stainless steels passivated in both (citric and nitric) passivating treatments.

Statistical evaluation of the time record was carried out and the localization index (LI) parameter was evaluated. According to the LI results, the PH stainless steels passivated in citric acid solution mainly show a mixed corrosion type, whereas LI values for the PH stainless steels passivated in nitric acid solution indicates localized corrosion.

In general, potentiodynamic polarization results indicated that, irrespective of the type of PH stainless steel used, the nitric acid passivation treatment largely increases the pitting potentials in comparison with the citric acid treatment. Also, for both passivation treatments, very low corrosion rate values (in the order of 10^{-7} mm/year) were recorded for both 15-5PH and 17-4PH steels.

On the whole, citric passivation treatments on PH stainless steels could be a green alternative route to the currently employed nitric passivation treatments.

Author Contributions: Conceptualization, M.L.-B., F.A.-C.; Methodology, P.Z.-R., M.D.-E, F.E.-L., E.M.-B.; Data Curation, C.G.-T., J.A.C.-M., and D.N.-M.; Formal analysis, J.G.C.-N., and F.A.-C.; Writing—Review and Editing, M.L.-B., J.G.C.-N., F.A.-C. All authors have read and agreed to the published version of the manuscript.

Funding: This research was funded by the Conacyt, Proyect "Estudio de las propiedades electroquímicas y mecanismos de crecimiento de la película de pasivación de aceros inoxidables endurecibles por precipitación en ambientes ácidos", con clave No. A1-S-8882 and UANL (Dirección de Investigación).

Acknowledgments: The authors acknowledge The Academic Body UANL—CA-316 "Deterioration and integrity of composite materials".

Conflicts of Interest: All authors of this article declare no conflicts of interest.

References

1. Siddiqui, T. *Aircraft Materials and Analysis*; McGraw Hill Education: New York, NY, USA, 2015; pp. 127–136.
2. ASM International. *ASM Handbook*; Corrosion Environments and Industries; Cramer, S.D., Covino, B.S., Jr., Eds.; ASM International: Materials Park, OH, USA, 2006; Volume 13, p. 27, Corrosion Environments and Industries.
3. Schorr, M.; Valdez, B.; Salinas, R.; Ramos, R.; Nedey, N.; Curiel, M. Corrosion control in military assets. *MRS Online Proc. Libr. Arch.* **2016**, *1815*. [CrossRef]
4. Lara-Banda, M.; Ortiz, D.; Gaoan-Tiburcio, C.; Zambrano, P.; Cabral-Miramontes, J.C.; Almeraya-Calderon, F. Citric Acid Passivation of 15-5PH and 17-4PH Stainless Steel Used in the Aeronautical Industry. In *International Materials Research Congress*; Springer: Cham, Switzerland, 2016; pp. 95–104.
5. Lopes, J.C. Material selection for aeronautical structural application. *Sci. Technol. Adv. Mat.* **2008**, *20*, 78–82.
6. Lewis, P.; Kolody, M. Alternative to Nitric Acid Passivation of Stainless Steel Alloys. In *Technology Evaluation for Environmental Risk Mitigation Compendium, Proceedings of the NASA Technology Evaluation for Environmental Risk Mitigation Principal Center (TEERM)*; Department od Defense (DoD) and NASA: Merritt Island, FL, USA, 2008.
7. Calle, L.M. Coatings on Earth and Beyond. In Proceedings of the Coatings Summit 2015, Cocoa Beach, FL, USA, 21–23 January 2015.
8. O'Laoire, C.; Tmmins, B.; Kremer, L.; Holmes, J.D.; Morris, M.A. Analysis of the acid passivation of stainless steel. *Anal. Lett.* **2006**, *39*, 2255–2271. [CrossRef]
9. Olsson, C.O.; Landolt, D. Passive films on stainless steels-chemistry, structure and growth. *Electrochim. Acta* **2003**, *48*, 1093–1104. [CrossRef]
10. Yasensky, D.; Reali, J.; Larson, C.; Carl, C. Citric acid passivation of stainless steel. In Proceedings of the Aircraft Airworthiness and Sustainment Conference, San Diego, CA, USA, 18–21 April 2009.
11. Lo, K.H.; Shek, C.H.; Lai, J.K.L. Recent developments in stainless steels. *Mater. Sci. Eng. R.* **2009**, *65*, 39–104. [CrossRef]
12. Cobb, H.M. *The History of Stainless Steel*; ASM International: Cleveland, OH, USA, 2010; pp. 189–192.
13. Ha, H.Y.; Jang, J.H.; Lee, T.H.; Won, C.; Lee, C.H.; Moon, J.; Lee, C.G. Investigation of the localized corrosion and passive behavior of type 304 stainless steels with 0.2–1.8 wt% B. *Materials* **2018**, *11*, 2097. [CrossRef] [PubMed]
14. Schmuki, P. From bacon to barriers: A review on the passivity of metal and alloys. *J. Solid State Electr.* **2002**, *6*, 145–164. [CrossRef]
15. Abdelshehid, M.; Mahmodieh, K.; Mori, K.; Chen, L.; Stoyanov, P.; Davlantes, D.; Foyos, J.; Ogren, J.; Clark, R., Jr.; Es-Said, O.S. On the correlation between fracture toughness and precipitation hardening heat treatments in 15-5PH stainless steel. *Eng. Fail. Anal.* **2007**, *14*, 626–631. [CrossRef]
16. Esfandiari, M.; Dong, H. The corrosion and corrosion–wear behaviour of plasma nitrided 17-4PH precipitation hardening stainless steel. *Surf. Coat. Technol.* **2007**, *202*, 466–478. [CrossRef]
17. Dong, H.; Esfandiari, M.; Li, X.Y. On the microstructure and phase identification of plasma nitrided 17-4PH precipitation hardening stainless steel. *Surf. Coat. Technol.* **2008**, *202*, 2969–2975. [CrossRef]
18. Hsiao, C.N.; Chiou, C.S.; Yang, J.R. Aging reactions in a 17-4 PH stainless steel. *Mater. Chem. Phys.* **2002**, *74*, 134–142. [CrossRef]
19. Gladman, T. Precipitation hardening in metals. *Mater. Sci. Technol.* **1999**, *15*, 30–36. [CrossRef]

20. Schade, C.; Stears, P.; Lawley, A.; Doherty, R. Precipitation Hardening PM Stainless Steels. *Adv. Powder Part.* **2006**, *1*, 7.
21. Gaydos, S.P. Passivation of aerospace stainless parts with citric acid solutions. *Plat. Surf. Finish.* **2003**, *90*, 20–25.
22. Shibata, T. Stochastic studies of passivity breakdown. *Corros. Sci.* **1990**, *31*, 413–423. [CrossRef]
23. Ashassi-Sorkhabi, H.; Seifzadeh, D.; Raghibi-Boroujeni, M. Analysis of electrochemical noise data in both time and frequency domains to evaluate the effect of ZnO nanopowder addition on the corrosion protection performance of epoxy coatings. *Arab. J. Chem.* **2016**, *9*, S1320–S1327. [CrossRef]
24. Isselin, J.; Kasada, R.; Kimura, A. Effects of aluminum on the corrosion behavior of 16% Cr ODS ferritic steels in a nitric acid solution. *J. Nucl. Sci. Techmol.* **2011**, *48*, 169–171. [CrossRef]
25. Estupiñán, F.H.; Almeraya, F.; Margulis, R.B.; Zamora, M.B.; Martínez, A.; Gaona, C. Transient analysis of electrochemical noise for 316 and duplex 2205 stainless steels under pitting corrosion. *Int. J. Electrochem. Sci.* **2011**, *6*, 1785–1796.
26. Upadhyay, N.; Pujar, M.G.; Sekhar, S.S.; Gopala, K.N.; Mallika, C.; Kamachi, M.U. Evaluation of the Effect of Molybdenum on the Pitting Corrosion Behavior of Austenitic Stainless Steels Using Electrochemical Noise Technique. *Corrosion* **2017**, *73*, 1320–1334. [CrossRef]
27. Bragaglia, M.; Cherubini, V.; Cacciotti, I.; Rinaldi, M.; Mori, S.; Soltani, P.; Nanni, F.; Kaciulis, S.; Montesperelli, G. Citric Acid Aerospace Stainless Steel Passivation: A Green Approach. In Proceedings of the CEAS Aerospace Europe Conference 2015, Delft, The Netherlands, 7–11 September 2015.
28. Huet, F. Electrochemical Noise Technique. In *Analytical Methods in Corrosion Science and Engineering*; Marcus, P., Florian, B., Eds.; Mansfeld CRC Taylor & Francis: Boca Raton, FL, USA, 2006; Chapter 14, pp. 507–570.
29. Suresh, G.U.; Kamachi, M.S. Electrochemical Noise Analysis of Pitting Corrosion of Type 304L Stainless Steel. *Corrosion* **2014**, *70*, 283–293. [CrossRef]
30. Homborg, A.M.; Cottis, R.A.; Mol, J.M.C. An integrated approach in the time, frequency and time-frequency domain for the identification of corrosion using electrochemical noise. *Electrochim. Acta* **2016**, *222*, 627–640. [CrossRef]
31. Nazarnezhad, B.M.; Neshati, J.; Hossein, S.M. Development of Time-Frequency Analysis in Electrochemical Noise for Detection of Pitting Corrosion. *Corrosion* **2019**, *75*, 183–191.
32. Ortiz, A.C.J.; Lucio–Garcia, M.A.; Hermoso-Diaz, I.A.; Chacon-Nava, J.G.; Martínez-Villafañe, A.; Gonzalez-Rodriguez, J.G. Detection of Sulfide Stress Cracking in a Supermartensitic Stainless Steel by Using Electrochemical Noise. *Int. J. Electrochem. Sci.* **2014**, *9*, 6717–6733.
33. Al-Zanki, I.A.; Gill, J.S.; Dawson, J.L. Electrochemical Noise Measurements on Mild Steel in 0.5 M Sulphuric Acid. *Mater. Sci. Forum* **1986**, *8*, 463–476. [CrossRef]
34. Cuevas-Arteaga, C.; Porcayo-Calderón, J. Electrochemical noise analysis in the frequency domain and determination of corrosion rates for SS-304 stainless steel. *Mater. Sci. Eng. A* **2006**, *435–436*, 439–446. [CrossRef]
35. *Standard Practice for Cleaning, Descaling and Passivation of Stainless-Steel Parts, Equipment, and Systems*; ASTM A380-17; ASTM International: West Conshohocken, PA, USA, 1999.
36. *Standard Specification for Chemical Passivation Treatments for Stainless Steel Parts*; ASTM A967-17; ASTM International: West Conshohocken, PA, USA, 1999.
37. *Standard Guide for Electrochemical Noise Measurement*; ASTM G199-09; ASTM International: West Conshohocken, PA, USA, 2009.
38. Mansfeld, F.; Sun, Z. Localization index obtained from electrochemical noise analysis. *Corrosion* **1999**, *55*, 915–918. [CrossRef]
39. Sanchez, J.M.; Cottis, R.A.; Botana, F.J. Shot noise and statistical parameters for the estimation of corrosion mechanisms. *Corros. Sci.* **2005**, *47*, 3280–3299. [CrossRef]
40. Kelly, R.G.; Inman, M.E.; Hudson, J.L. Analysis of electrochemical noise for type 410 stainless steel in chloride solutions. In *Electrochemical Noise Measurement for Corrosion Applications*; ASTM International: West Conshohocken, PA, USA, 1996.
41. *Standard Reference Test Method for Making Potentiostaticc and Potentiodynamic Anodic Polarization Measurements*; ASTM-G5-13E2; ASTM International: West Conshohocken, PA, USA, 2013.
42. *Standard Practice for Calculation of Corrosion Rates from Electrochemical Measurements*; ASTM-G102-89; ASTM International: West Conshohoken, PA, USA, 2010.
43. Ha, H.Y.; Kang, J.Y.; Yang, J.; Yim, C.D.; You, B.S. Limitations in the use of the potentiodynamic polarisation curves to investigate the effect of Zn on the corrosion behaviour of as-extruded Mg–Zn binary alloy. *Corros. Sci.* **2013**, *75*, 426–433. [CrossRef]

44. Treseder, R.S. *NACE Corrosion Engineers Reference Book*, 2nd ed.; NACE International: Houston, TX, USA, 1991.
45. Bertocci, U.; Yang-Xiang, Y. An examination of current fluctuations during pit initiation in Fe-Cr alloys. *J. Electrochem. Soc.* **1984**, *131*, 1011–1017. [CrossRef]
46. Bertocci, U.; Koike, M.; Leigh, S.; Qiu, F.; Yang, G. A statistical analysis of the fluctuations of the passive current. *J. Electrochem. Soc.* **1986**, *133*, 1782. [CrossRef]
47. Miyata, Y.; Handa, T.; Takazawa, H. An analysis of current fluctuations during passive film breakdown and repassivation in stainless alloys. *Corros. Sci.* **1990**, *31*, 465–470. [CrossRef]
48. Savas, T.P.; Wang, A.Y.L.; Earthman, J.C. The effect of heat treatment on the corrosion resistance of 440C stainless steel in 20% HNO_3 + 2.5% $Na_2Cr_2O_7$ solution. *J. Mater. Eng. Perform.* **2003**, *12*, 165–171. [CrossRef]
49. Heyn, A.; Goellner, J.; Bierwirth, M.; Klapper, H. Recent applications of electrochemical noise for corrosion testing-Benefits and restrictions. In *CORROSION 2007, Proceedings of the Corrosion NACE Expo2007, Nashville, TN, USA, 11–15 March 2007*; NACE International: Houston, TX, USA, 2007.
50. Eden, A.D.; John, G.D.; Dawson, J.L. Corrosion Monitoring. International Patent WO1987007022A1, 19 November 1987.
51. Brennenstuhl, A.M.; Palumbo, G.; Gonzalez, F.S.; Quirk, P.G. The Use of Electrochemical Noise to Investigate the Corrosion Resistance of UNS Alloy N04400 Nuclear Heat Exchanger Tubes. In *Electrochemical Noise Measurement for Corrosion Applications*; ASTM International: West Conshohocken, PA, USA, 1996.
52. Padilla-Viveros, A.; Garcia-Ochoa, E.; Alazard, D. Comparative electrochemical noise study of the corrosion process of carbon steel by the sulfate-reducing bacterium *Desulfovibrio alaskensis* under nutritionally rich and oligotrophic culture conditions. *Electrochim. Acta* **2006**, *51*, 3841–3847. [CrossRef]
53. Webster, S.; Nathanson, L.; Green, A.G.; Johnson, B.V. The Use of Electrochemical Noise to Assess Inhibitor Film Stability. In *UK Corrosion 1992*; Institute of Corrosion: Manchester, UK, 1992.
54. Rothwell, A.N.; Edgemon, G.L.; Bell, G.E.C. *Data Processing for Current and Potential Logging Field Monitoring Systems*; CORROSION/1999, paper no. 192; NACE: Houston, TX, USA, 1999.
55. Girija, U.; Mudali, K.; Khatak, H.S.; Raj, B. The application of electrochemical noise resistance to evaluate the corrosion resistance of AISI type 304 *SS* in nitric acid. *Corros. Sci.* **2007**, *49*, 4051–4068. [CrossRef]
56. Homborg, A.M.; Tinga, T.; Van Westing, P.M.; Zhang, X.; Ferrari, G.M.; de Wit, J.H.W.; Mol, J.M.C. A Critical Appraisal of the Interpretation of Electrochemical Noise for Corrosion Studies. *Corrosion* **2014**, *70*, 971–987. [CrossRef]
57. Cottis, R.A.; Al-Awadhi, M.A.A.; Al-Mazeedi, H.; Turgoose, S. Measures for the detection of localized corrosion with electrochemical noise. *Electrochim. Acta.* **2001**, *46*, 3665–3674. [CrossRef]
58. Jurak, T.; Jamali, S.S.; Yue Zhao, Y. Theoretical analysis of electrochemical noise measurement with single substrate electrode configuration and examination of the effect of reference electrodes. *Electrochim. Acta* **2019**, *3011*, 377–389. [CrossRef]
59. Cottis, R.A. Interpretation of Electrochemical Noise Data. *Corrosion* **2001**, *57*, 265–285. [CrossRef]
60. Betova, I.; Bojinov, M.; Laitinen, T.; Mäkelä, K.; Pohjanne, P.; Saario, T. The transpassive dissolution mechanism of highly alloyed stainless steels: I. Experimental results and modelling procedure. *Corros. Sci.* **2002**, *44*, 2675–2697. [CrossRef]
61. Ye, W.; Li, Y.; Wang, F. The improvement of the corrosion resistance of 309stainless steel in the transpassive region by nano-crystallization. *Electrochem. Acta* **2009**, *54*, 1339–1349. [CrossRef]
62. Man, C.; Dong, C.; Cui, Z.; Xiao, K.; Yu, Q.; Li, X. A comparative study of primary and secondary passive films formed on AM355 stainless steel in 0.1 M NaOH. *Appl. Surf. Sci.* **2018**, *427*, 763–773. [CrossRef]
63. Bojinov, M.; Betova, I.; Fabricius, G.; Laitinen, T.; Saario, T. The stability of the passive state of iron–chromium alloys in sulphuric acid solution. *Corros. Sci.* **1999**, *41*, 1557–1584. [CrossRef]
64. Bojinov, M.; Fabricius, G.; Kinnunen, P.; Laitinen, T.; Mäkelä, K.; Saario, T.; Sundholm, G. The mechanism of transpassive dissolution of Ni–Cr alloys in sulphate solutions. *Electrochem. Acta* **2000**, *45*, 2791–2802. [CrossRef]
65. Lara Banda, M.; Gaona-Tiburcio, C.; Zambrano-Robledo, P.; Cabral, M.J.A.; Estupinan, F.; Baltazar-Zamora, M.A.; Almeraya-Calderon, F. Corrosion Behaviour of 304 Austenitic, 15-5PH and 17-4PH Passive Stainless Steels in acid solutions. *Int. J. Electrochem. Sci.* **2018**, *13*, 10314–10324. [CrossRef]
66. Huang, J.; Wu, X.; Han, E.H. Electrochemical properties and growth mechanism of passive films on Alloy 690 in high-temperature alkaline environments. *Corros. Sci.* **2010**, *52*, 3444–3452. [CrossRef]

67. Calinski, C.; Strehblow, H.H. ISS depth profiles of the passive layer on Fe/Cr alloys. *J. Electrochem. Soc.* **1989**, *36*, 1328–1331. [CrossRef]
68. Radhakrishnamurty, P.; Adaikkalam, P. pH-potential diagrams at elevated temperatures for the chromium/water systems. *Corros. Sci.* **1982**, *22*, 753–773. [CrossRef]

materials

MDPI

Article

Preparation and Corrosion Behavior in Marine Environment of MAO Coatings on Magnesium Alloy

Yuhong Yao [1,*], Wei Yang [1,*], Dongjie Liu [2], Wei Gao [1] and Jian Chen [1]

[1] School of Materials Science and Chemical Engineering, Xi'an Technological University, Xi'an 710032, China; eifa@sina.com (W.G.); chenjian@xatu.edu.cn (J.C.)

[2] School of Materials Science and Engineering, Xi'an University of Technology, Xi'an 710048, China; liudongjie@xaut.edu.cn

* Correspondence: yyhong0612@yahoo.com (Y.Y.); yangwei_smx@163.com (W.Y.)

Received: 1 December 2019; Accepted: 10 January 2020; Published: 12 January 2020

Abstract: To improve the corrosion performance of magnesium alloys in the marine environment, the MAO, MAO–$Cu_2CO_3(OH)_2{\cdot}H_2O$ and MAO–$Cu_2P_2O_7$ ceramic coatings were deposited on AZ91D magnesium alloys in basic electrolyte and the discoloration mechanism of the Cu-doped MAO coatings and the corrosion behavior of the three MAO coatings in the artificial seawater solution were investigated by SEM, EDS and XPS. The results indicated that the formation and discoloration mechanism of the brown MAO ceramic coatings were attributable to the formation of Cu_2O in the coatings. Though the three MAO coatings had a certain protective effect against the corrosion of AZ91D substrate in the artificial seawater, the distinctive stratification phenomenon was found on the MAO–$Cu_2P_2O_7$ coated sample and the corrosion model of the MAO–$Cu_2P_2O_7$ coatings in the immersion experiment was established. Therefore, the brown Cu-doped MAO coatings were speculated to significantly reduce the risk of the magnesium parts in marine environments.

Keywords: magnesium alloy; MAO coating; corrosion behavior; stratification phenomena; marine environments

1. Introduction

The magnesium alloy is the lightest structure metal material, and is considered as the green engineering material in the 21st century [1]. Now it is widely applied to the electronic industry, aerospace industry, and auto industry [2,3]. However, for its poor corrosion resistance, magnesium alloy, particularly as the magnesium alloy parts for outdoor applications, is confronted with great challenges [4–7]. Many literatures have verified that the surface modification technique, such as chemical conversion coatings, anodic oxidation, micro arc oxidation (MAO), organic coatings, vapor phase processes, etc, is an effective way to change the surface composition and improve its corrosion resistance of magnesium alloy [8–12]. MAO is a newly developed technology for the preparation of ceramic coatings on aluminum, magnesium or titanium alloys to improve the corrosion resistance [10,13–16]. At present, the synthesis of white MAO coatings on magnesium alloy is a mature and universal technology [16], but it has the same disadvantage as the chemical conversion coating technology, which often causes the formation of the light spots on the surfaces of magnesium diecast components and hardly meets the market demand of 3C (computer, communication and consumer) electronic products. It has been reported that the colored MAO coatings can be formed by adding metal salts in the electrolytes [17–24]. The black MAO coating containing V_2O_3 can be obtained on an aluminum alloy surface by adding ammonium metavanadate into the commonly used $(NaPO_3)_6$ (sodium hexametaphosphate) and Na_2SiO_3 solution [21] and the black MAO coating with excellent properties can also be prepared in the electrolyte with dichromate addition [22]. Moreover, it has been reported that by adding potassium fluotitanate or sodium stannate into the base electrolyte, a yellow or grey MAO coating can be formed on the surface of Mg alloys, respectively [23,24].

Brown is a very important and common decorative color. Lee et al. [25] has reported that with the addition of 3% and 5% Cu in the base electrolyte, the color of the MAO coating changes from brown to dark brown and the corrosion resistance of the AZ91 alloy is significantly improved after being treated with the micro-arc oxidation process, but the corrosion process and coloring mechanism of this brown MAO coating are still not clear. Furthermore, the magnesium alloy parts with MAO coating for lightweight are sometimes exposed to marine environment and the marine corrosion behavior of the coatings has not been clarified. As a result, the application of magnesium alloy in a marine environment is seriously restricted. In this study, a convenient process to fabricate the MAO coatings with brown color on Mg alloys is introduced by adding alkaline copper carbonate and copper pyrophosphate in the electrolyte and the white and two brown MAO coatings are prepared. Then, the microstructure, formation mechanism and seawater corrosion behaviors of the coatings are investigated in detail. Finally, the seawater corrosion mechanism of the MAO coatings is revealed, which is helpful for the surface protection of magnesium alloy applied in marine environments.

2. Materials and Methods

AZ91D magnesium alloys were used as the substrate discs in the size of ϕ30 mm × 5 mm and its nominal chemical composition (in wt. %) was Al 8.5–9.5 %, Zn 0.5–0.9 %, Mn 0.17–0.27 %, Cu ≤0.01, Ni ≤0.01, Si ≤0.01, Fe ≤0.004 and Mg balance. Before the micro arc coatings, the specimens were prepared by means of standard metallographic procedure, such as coarse grinding, accurate grinding, polishing with alumina waterproof abrasive paper up to 1200 grit and then ultrasonically degreased in acetone for 10 min followed by rinsing with distilled water.

The MAO coatings were prepared on the specimen surface by using of micro arc oxidation equipment (JHMAO-60, China) with the constant voltage of 420 V, the frequency of 400 Hz, the duty cycle of 10% and the treatment time of 8 min. The base electrolyte solution was composed of 8.0 g/L sodium silicate ($Na_2SiO_3{\cdot}9H_2O$), 5.0 g/L potassium hydroxide (KOH), 5.0 g/L potassium fluoride (KF), 1.0 g/L EDTA ($C_{10}H_{16}N_2O_8$) and 3.5 g/L potassium sodium tartrate ($C_4H_4O_6KNa{\cdot}4H_2O$). The two Cu-doped brown coatings were prepared by respectively adding 2.5 g/L basic copper carbonate ($Cu_2CO_3(OH)_2{\cdot}H_2O$) and 2.5 g/L copper pyrophosphate (Cu2P2O7) into the base solution and the temperature of the electrotype with pH of about 13 was kept below 35 °C during the MAO process.

The thickness of the MAO coatings was measured by using TT240 eddy current thickness meter with an accuracy of 0.1 μm. Six measurements were carried out evenly on the whole sample surface. The surface morphologies and element distribution of the MAO coatings were analyzed by scanning electron microscope (SEM) with Oxford Inca X-Max energy dispersive spectrometry (EDS). X-ray photoelectron spectroscopy (XPS) with Al (mono) Kα irradiation at pass energy of 160 eV (AXIS UTLTRADLD) was used to characterize the chemical bonds of the coatings. The binding energies were referenced to the C 1 s line at 284.6 eV from adventitious carbon. The corrosion behavior of the coated AZ91D magnesium alloy was evaluated by the immersion tests in the artificial seawater, whose composition was shown in Table 1. Before the immersion test, the three MAO-coated specimens were treated with epoxy resin to avoid the effect of defects at the edge of the samples, then immersed in the artificial seawater solution for 14 days and the corrosion morphologies of the samples were observed by SEM.

Table 1. Composition of artificial seawater in immersion test.

Chemical Reagents	Concentration (g/L)
NaCl	24.53
$MgCl_2{\cdot}6H_2O$	11.11
Na_2SO_4	4.09
$CaCl_2$	1.16
KCl	0.70
$NaHCO_3$	0.20
KBr	0.10

3. Results and Discussions

The MAO–$Cu_2CO_3(OH)_2{\cdot}H_2O$ and MAO–$Cu_2P_2O_7$ coatings on AZ91D magnesium alloys in Figure 1 are prepared with the thicknesses of 8.4 μm, 9.1 μm and 9.6μm, respectively. It reveals that for the more intense micro arc discharge many defects are observed at the edge of the sample in Figure 1b. The microstructures of the three MAO coatings are given in Figure 2. It can be seen from Figure 2 that the surfaces of the three MAO coatings are characterized by lots of micropores with the size range from submicron to several micro scale, and different from the MAO and MAO–$Cu_2P_2O_7$ coatings, there are some bumps on the MAO–$Cu_2CO_3(OH)_2{\cdot}H_2O$ coating surface, which are formed by the spark discharge and gas bubbles throughout the discharge channels during MAO process [26,27]. So it reveals that the addition of $Cu_2CO_3(OH)_2{\cdot}H_2O$ into the base electrolyte results in a strongly intense micro arc discharge, which promotes the formation of large molten deposits (Figure 2c,d). The elemental compositions of the three MAO coatings are examined by EDS in Table 2. Carbon (C) is considered to be an impurity from the atmosphere or the electrolyte, F and Na are also presumed to originate from the electrolyte or the AZ91D alloy substrate, P and Si are from the electrolyte and Zn comes from the substrate which indicates that the thickness of the three MAO coatings is very thin. Thus the three MAO coatings are mainly composed of Mg, O, Si and a little amount of C, F, Na species. The presence of Si and O reveals that the components of the electrolyte have intensively incorporated into the micro arc oxidation reactions to from the ceramic coatings [16]. Moreover, by addition of $Cu_2CO_3(OH)_2{\cdot}H_2O$ or $Cu_2P_2O_7$ into the electrolyte, a very small amount of Cu or Cu, P has been respectively doped into the MAO–$Cu_2CO_3(OH)_2{\cdot}H_2O$ and MAO–$Cu_2P_2O_7$ coatings to make the color of the coatings change from white to brown. The discoloration mechanism of the MAO coatings will be further discussed by using SEM + EDS and XPS.

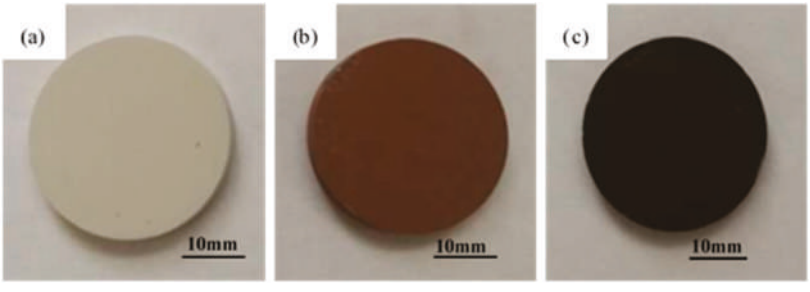

Figure 1. Macrograph of three MAO coatings on AZ91D magnesium alloy, (**a**) MAO, (**b**) MAO–$Cu_2CO_3(OH)_2{\cdot}H_2O$ and (**c**) MAO–$Cu_2P_2O_7$.

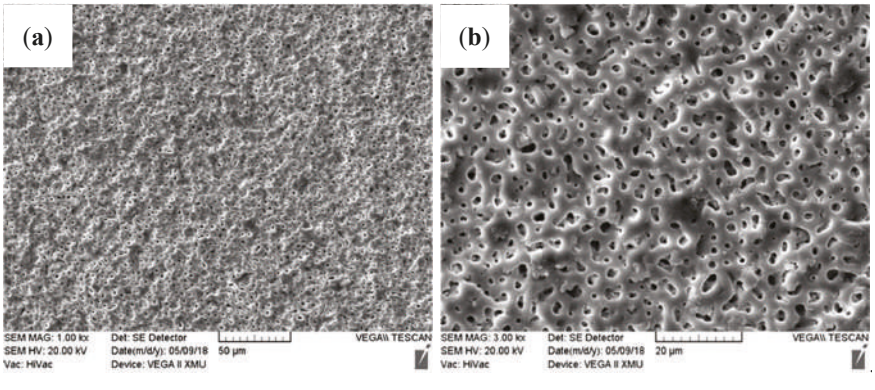

Figure 2. *Cont.*

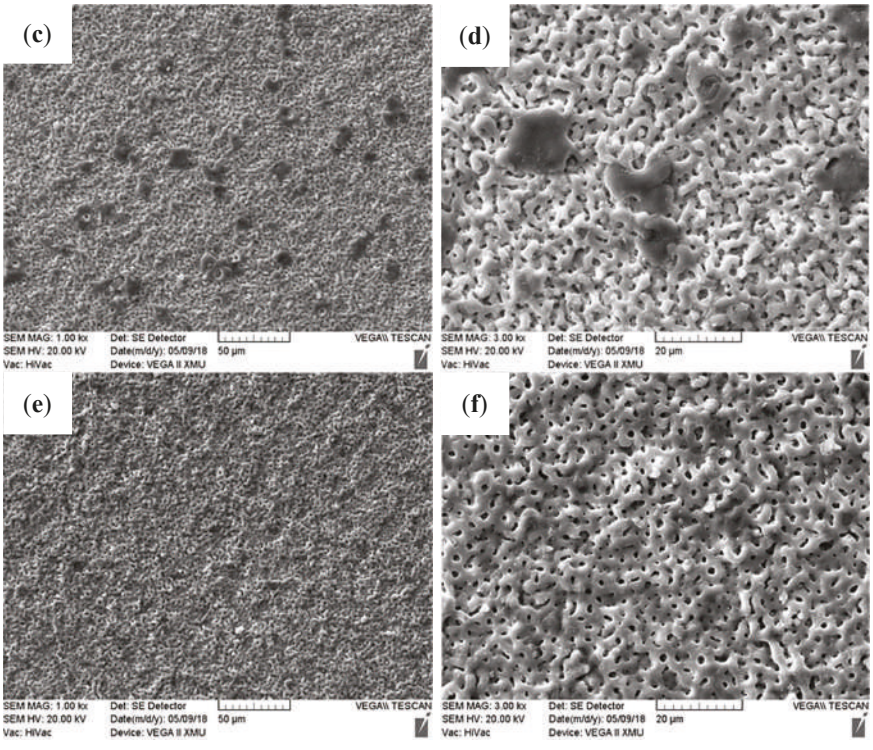

Figure 2. Surface morphologies of three MAO coatings on AZ91D magnesium alloy, (**a**) and (**b**) MAO, (**c**) and (**d**) MAO–$Cu_2CO_3(OH)_2{\cdot}H_2O$ and (**e**) and (**f**) MAO–$Cu_2P_2O_7$.

Table 2. EDS results of the MAO, MAO–$Cu_2CO_3(OH)_2{\cdot}H_2O$ and MAO–$Cu_2P_2O_7$ coatings on AZ91D magnesium alloy (at. %).

Coatings	C	O	F	Na	Mg	Si	Zn	Cu	P
MAO	1.84	49.64	3.63	0.46	33.98	9.78	0.67	-	-
MAO–$Cu_2CO_3(OH)_2{\cdot}H_2O$	2.95	48.18	3.76	0.86	35.28	8.05	0.39	0.53	-
MAO–$Cu_2P_2O_7$	2.35	49.42	4.45	0.21	32.42	7.27	1.17	0.74	2.81

The surface morphologies of the MAO–$Cu_2CO_3(OH)_2{\cdot}H_2O$ coatings formed at different oxidation times are shown in Figure 3 and the corresponding EDS analysis results are listed in Table 3. As shown in Figure 3a and Table 3, when the oxidation time is about 70 s, the surface morphology of the AZ91D substrate is inhomogeneous at the moment of starting arc with two distinct regions: region I with a damaged area caused by electrical break-down involving amount of O, F, Si and Cu elements from the electrolyte and Mg and Zn alloying species from the substrate, and region II with a smooth surface morphology and the scratches in the substrate including lower content of O, Si, Cu and much higher content of Mg than those in region I, which indicates that the electrical breakdown phenomenon does not occur in region II. With the prolongation of oxidation time, the surface of the samples presents a typical porous feature and the pore size of the MAO coatings increases with the oxidation time in Figure 3b–d; a similar micro arc process and the mechanism of the pore initiation and the pore development are reported by some literatures [10,21]. However, it is worth noting that the concentrations of O, F, Si, Cu, Mg and Zn elements are similar in the MAO–$Cu_2CO_3(OH)_2{\cdot}H_2O$ coatings, the color of the coatings gradually becomes deeper with oxidation time, so it is very meaningful to analyze the discoloration mechanism of the coatings.

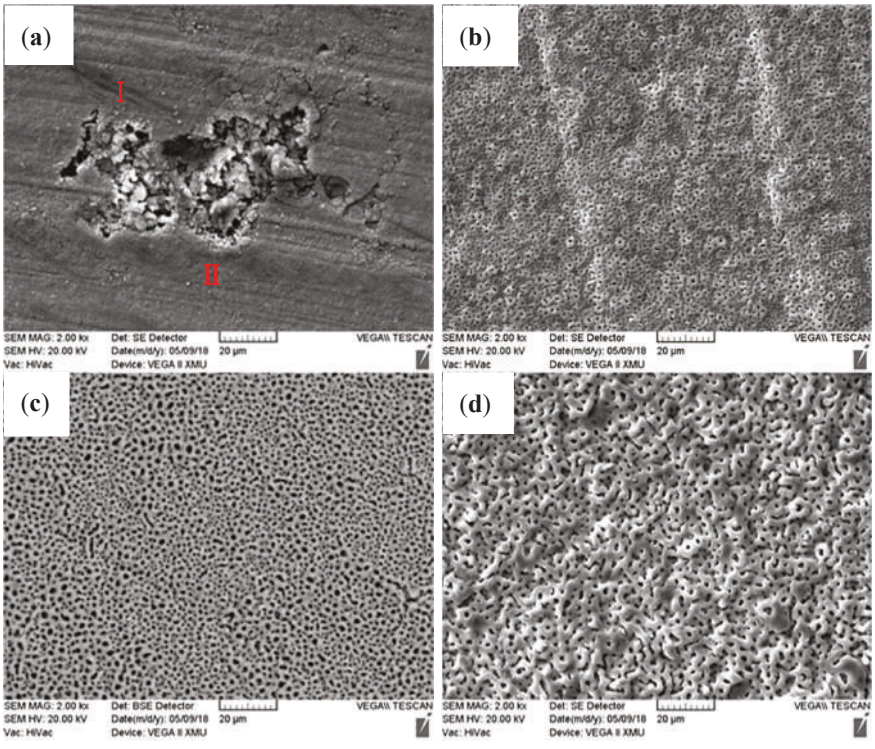

Figure 3. Surface morphologies of MAO–$Cu_2CO_3(OH)_2{\cdot}H_2O$ coatings formed with different oxidation time on AZ91D magnesium alloy, (**a**) 70 s, (**b**) 100 s, (**c**) 120 s and (**d**) 180 s.

Table 3. EDS results of MAO–$Cu_2CO_3(OH)_2{\cdot}H_2O$ coatings formed with different oxidation time on AZ91D magnesium alloy (at. %).

Oxidation Time	C	O	F	Mg	Si	Cu	Zn
70 s—I	2.92	45.97	4.45	36.30	7.73	0.26	2.37
70 s—II	2.05	29.67	2.77	60.81	2.45	-	1.76
100 s	1.04	49.26	5.97	34.99	7.71	0.28	0.75
120 s	1.00	52.41	5.80	32.41	7.65	0.28	0.45
180 s	1.80	50.68	4.55	34.28	8.16	0.12	0.40

The chemical states of Cu, Mg and Si are investigated by using XPS in Figure 4. From the wide spectra demonstrated in Figure 4a, Mg, O, Si and F elements are all found in the three MAO coatings and Cu is detected in the MAO coating with MAO–$Cu_2CO_3(OH)_2{\cdot}H_2O$ or $Cu_2P_2O_7$ addition by XPS. The Cu2p3/2 spectrum consists of two peaks at the binding energies of 932 eV associated with Cu_2O and 939.7 eV corresponding to CuF_2 in the brown MAO coating with $Cu_2CO_3(OH)_2{\cdot}H_2O$ addition in Figure 4b. Figure 4c,d illustrate that the Mg2p peak at the binding energy of 47.8 eV and the Si2p peak of 100.25 eV are individually assigned to MgO and SiO2. So, it can be concluded that the solute ions (such as Cu and Si) from the electrolyte are involved in the growth process of the MAO coatings, and the same results are found in the growth process of the MAO coatings on Ti substrate [28,29]. Therefore, it is the formation of the red Cu_2O in the MAO coatings with MAO–$Cu_2CO_3(OH)_2{\cdot}H_2O$ addition that results in the discoloration of the coatings.

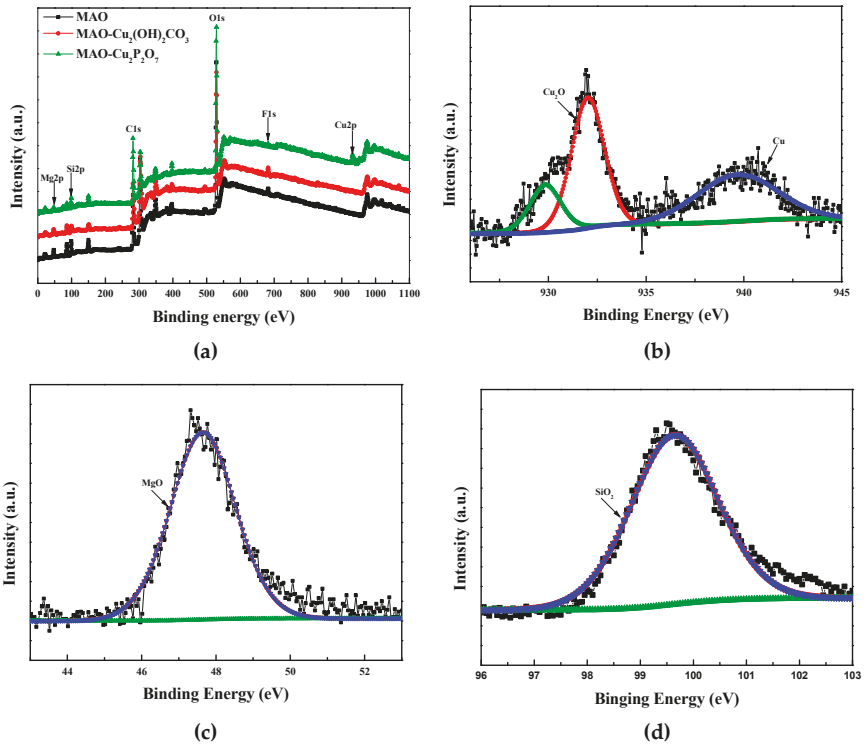

Figure 4. (**a**) XPS survey spectra of three MAO coatings, (**b**) Cu2p, (**c**) Mg2p and (**d**) Si2p typical high-resolution XPS spectrum of MAO–$Cu_2CO_3(OH)_2{\cdot}H_2O$ coatings.

Figures 5 and 6 are the macro and micro surface appearances of the three MAO coatings immersed in the artificial seawater solution for 14 days, respectively. Compared with Figure 1, it can be observed from Figure 5 that the color of the three MAO coatings obviously changes and some corrosion products are formed on the immersed coatings. The corrosion is more serious at the edge of the three MAO samples due to the defects caused by micro arc discharge (Figure 1b) or the damage during the embedding. It has been reported that once the corrosion reaction is initiated on the sample through a pit or minute pore, the corrosive medium can come into contact with the substrate to form some corrosion pits [30]. The elemental compositions of the three MAO coatings detected by EDS after the immersion test are listed in Table 4. The three corroded MAO coatings are mainly composed of Mg from the substrate and the artificial seawater and O from the electrolyte during the micro arc discharge, and Si, Cu and F from the electrolytes and Cl, K and Ca elements from the artificial seawater are also found in the corroded MAO coatings, which indicate that the MAO coatings are not completely destroyed. From Figure 6, it is quite clear that the microstructures of the MAO coatings have a significant change before and after the immersion test. The white MAO coating exhibits a relatively uniform surface appearance with a high degree of porosity, some cracks and corrosion products as shown in Figure 6a, which indicates that the AZ91D substrate is still protected by the coatings. The MAO–$Cu_2CO_3(OH)_2{\cdot}H_2O$ coatings are relatively rougher and exhibit a stacking structure with limited number of pores in Figure 6b. For the MAO–$Cu_2P_2O_7$ coatings, besides many micropores and some micro-cracks, there is a sedimentary layer with a lot of cracks in the coatings in Figure 6c and SEM morphology and EDS analysis results of this MAO coating after the immersion test are shown in detail in Figure 7 and Table 5. It can be seen from Figure 7 that the corroded coatings are divided into three regions: region I (the inner layer near the Mg substrate), region II (the middle layer attached to the

surface coating) and region III (the top layer). From Table 5, Mg, O, F and Si elements are found in the region I and the atom percentage of these elements is similar to those in the MAO coating before the immersion test. Moreover, Cl and Ca elements from the artificial seawater are not observed, indicating that the MAO ceramic coatings in region I have not been destroyed. Region II is a dense layer attached to the MAO coating, where the contents of Mg, Si and F elements dramatically decrease whereas the contents of O element significantly increase compared with that in region I; both Cl and Ca elements have been detected. It indicates that there is the interaction between the MAO coating and the corrosive medium. In the case of region III, this layer is relatively thick and composed of some loose and porous structure sediments, mainly containing O and Ca elements. It is well known that the deposition of corrosion products can hinder the transfer of the charge and increase the inhibition of corrosion, so it is believed that this thick sediment layer is very helpful to improve the corrosion behavior of the MAO–$Cu_2P_2O_7$ coatings in artificial seawater.

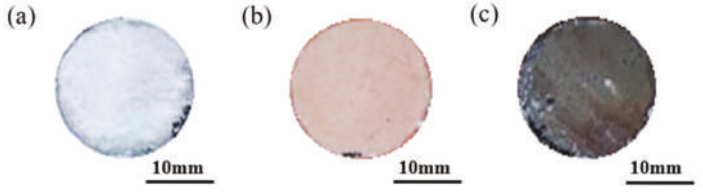

Figure 5. Macrograph of three MAO coatings, (**a**) MAO, (**b**) MAO–$Cu_2CO_3(OH)_2{\cdot}H_2O$ and (**c**) MAO–$Cu_2P_2O_7$, on AZ91D magnesium alloy after 14 days immersion test in the artificial seawater.

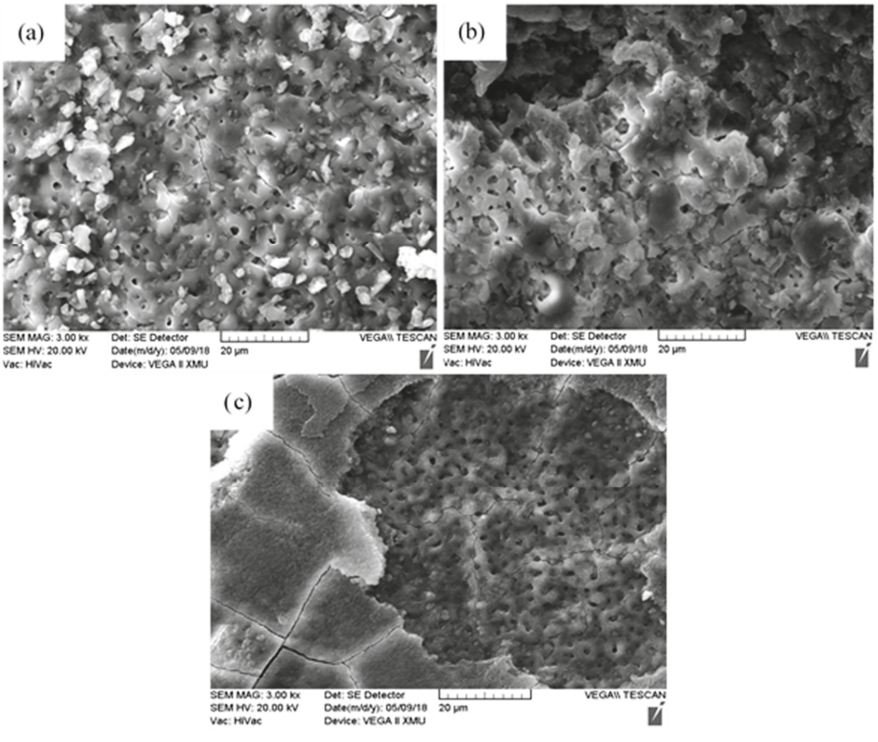

Figure 6. Micro morphologies of three MAO coatings by SEM after immersion test in the artificial seawater for 14 days, (**a**) MAO, (**b**) MAO–$Cu_2CO_3(OH)_2{\cdot}H_2O$ and (**c**) MAO–$Cu_2P_2O_7$.

Table 4. EDS results of the three MAO coatings immersed in artificial seawater for 14 days (at. %).

Coatings	O	Mg	Zn	Cu	Si	F	Cl	K	Ca
MAO	48.03	29.17	1.66	-	5.72	7.05	0.35	0.26	0.81
MAO–$Cu_2CO_3(OH)_2{\cdot}H_2O$	35.25	38.13	2.02	-	4.07	5.92	0.41	-	-
MAO–$Cu_2P_2O_7$	57.89	27.09	0.82	1.04	6.30	-	0.59	-	0.55

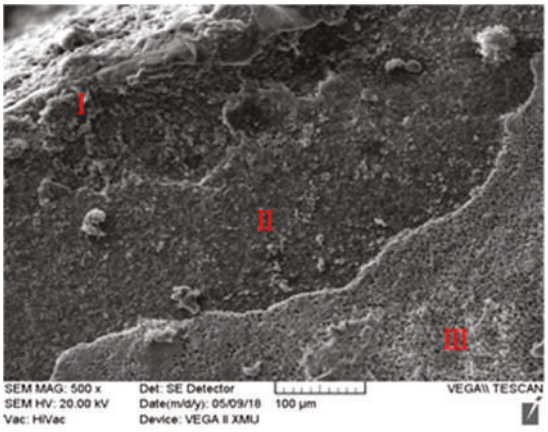

Figure 7. SEM surface morphologies and EDS results of MAO–$Cu_2P_2O_7$ coating after immersion test.

Table 5. EDS results of the three layers of the MAO–$Cu_2P_2O_7$ coatings immersed in artificial seawater for 14 days (at. %).

Regions	O	Mg	Si	F	Cl	Ca
Region I	47.08	30.15	5.72	7.05	-	-
Region II	60.47	25.42	2.37	-	0.73	2.57
Region III	71.34	0.61	-	-	-	22.09

From Figure 7 and Table 5, it has been learnt that the inner layer of the coatings is not destroyed near the substrate during the corrosion process, a middle dense layer is formed in the corrosion solution and the top thick deposition layer is of porous characteristics. Thus, a schematic diagram of the MAO–$Cu_2P_2O_7$ coatings during the immersion corrosion in the artificial seawater solution is shown in Figure 8. Due to the eruption and condensation of molten materials caused by micro arc discharge, the MAO coating normally has porous characteristics [31]. As a result, some interconnected micro closed-pores exist inside the MAO ceramic layer in Figure 8a. As shown in Figure 8b, the corrosion medium, especially Cl-, can seep into the interface between the electrolyte and the coatings through the micropores during the corrosion process; these micropores are exposed to the corrosive medium due to the oxygen concentration polarization between the interior holes and the interface. Then the corrosion products accumulate in the micropores and form a dense corrosion product layer on the MAO coating with the prolonging of the immersion corrosion time to prevent further corrosion of the coatings. Finally, the further interaction between the substrate and the artificial seawater has effectively been prevented by the corrosion product layer and the top calcium oxide-like thick porous layer forming on the middle dense layer in the following corrosion process in Figure 8c, which can further prevent the corrosion medium into the substrate to enhance its corrosion performance in the artificial seawater. Thus, it can be concluded that the stratification phenomena have been found on the MAO–$Cu_2P_2O_7$-coated sample and similar results have also been reported in the literatures [32,33]. However, although there is no Mg detected in the top sedimentary layer, for its loose and porous structure there is maybe a risk of corrosion for AZ91D substrate with further extension of the corrosion process.

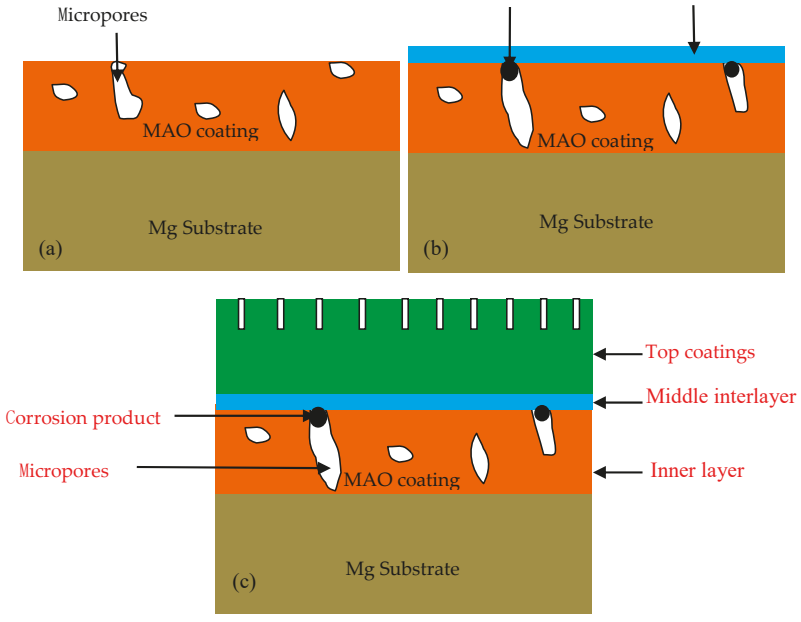

Figure 8. Schematic diagrams of the immersion corrosion of MAO–$Cu_2P_2O_7$ coating in the artificial seawater. (**a**) Morphology of MAO coating before corrosion, (**b**) Morphology of MAO coating at the initial stage of corrosion, (**c**) Morphology of MAO coating at the latter stage of corrosion.

4. Conclusions

(1) Brown MAO coatings on magnesium alloy can be prepared in the Na_2SiO_3 alkaline electrolyte with copper pyrophosphate or copper carbonate as the colorant, and for strongly intense micro arc discharge, some bumps appear on the Cu-doped MAO coatings.

(2) With the increase of reaction time, Cu in the colorant is fully involved in the formation of the MAO–$Cu_2CO_3(OH)_2{\cdot}H_2O$ and MAO–$Cu_2P_2O_7$ coatings on AZ91D magnesium alloys, and the discoloration mechanism of these coatings are attributed to the formation of Cu_2O in the coatings.

(3) After immersion in seawater for 14 days, the stratification corrosion microstructure with the three layers named the inner layer, the middle dense layer and the top calcium oxide-like layer are formed on the MAO–$Cu_2P_2O_7$ coated sample, which is helpful to prolong the service life of AZ91D magnesium alloys in artificial seawater.

Author Contributions: Designing the experiments, Y.Y., and W.Y.; performing the experiments, Y.Y., W.Y., D.L., and W.G.; contributing the reagents, materials and analysis tools, J.C.; analyzing the data, Y.Y., W.Y., D.L., and W.G.; writing—original draft preparation, Y.Y., and W.Y.; writing—review and editing, W.Y, and Y.Y. All authors have read and agreed to the published version of the manuscript.

Funding: This research was funded by the Key Research and Development Plan of Shaanxi Province—Industrial project (Grant No. 2018GY-127).

Conflicts of Interest: The authors declare no conflict of interest. The funders had no role in the design of the study; in the collection, analyses, or interpretation of data; in the writing of the manuscript, or in the decision to publish the results.

References

1. Ding, W.J. *Science and Technology of Magnesium Alloy*; Science Press: Beijing, China, 2007; pp. 1–10. (In Chinese)
2. Yi, A.H.; Du, J.; Wang, J.; Mu, S.L.; Zhang, G.G.; Li, W.F. Preparation and characterization of colored Ti/Zr conversion coating on AZ91D magnesium alloy. *Surf. Coat. Technol.* **2015**, *276*, 239–247. [CrossRef]

3. Li, O.; Tsunakawa, M.; Shimada, Y.; Nakamura, K.; Nishinaka, K.; Ishizaki, T. Corrosion resistance of composite oxide film prepared on Ca-added flame-resistant magnesium alloy AZCa612 by micro-arc oxidation. *Corros. Sci.* **2017**, *125*, 99–105. [CrossRef]
4. Zhang, C.Y.; Zeng, R.C.; Liu, C.L.; Gao, J.C. Comparison of calcium phosphatecoatings on Mg-Al and Mg-Ca alloys and their corrosion behavior in Hank's solution, *Surf. Coat. Technol.* **2010**, *204*, 3636–3640.
5. Cui, Z.Y.; Ge, F.; Lin, Y.; Wang, L.W.; Lei, L.; Tian, H.Y.; Yu, M.D.; Wang, X. Corrosion behavior of AZ31 magnesium alloy in the chloride solution containing ammonium nitrate. *Electrochim. Acta* **2018**, *278*, 421–437. [CrossRef]
6. Sadeghi, A.; Hasanpur, E.; Bahmani, A.; Shin, K.S. Corrosion behaviour of AZ31 magnesium alloy containing various levels of strontium. *Corros. Sci.* **2018**, *141*, 117–126. [CrossRef]
7. Qu, Q.; Li, S.L.; Li, L.; Zuo, L.M.; Ran, X.; Qu, Y.; Zhu, B.L. Adsorption and corrosion behaviour of Ttrichoderma harzianum for AZ31B magnesium alloy in artificial seawater. *Corros. Sci.* **2017**, *118*, 12–23. [CrossRef]
8. Arthanari, S.; Shin, K.S. A simple one step cerium conversion coating formation on to magnesium alloy and electrochemical corrosion performance. *Surf. Coat. Technol.* **2018**, *349*, 757–772. [CrossRef]
9. Wu, L.; Yang, D.N.; Zhang, G.; Zhang, Z.; Zhang, S.; Tang, A.T.; Pan, F.S. Fabrication and characterization of Mg-M layered double hydroxide films on anodized magnesium alloy AZ31. *Appl. Surf. Sci.* **2018**, *431*, 177–186. [CrossRef]
10. Zhang, R.F.; Zhang, S.F. Formation of micro-arc oxidation coatings on AZ91HP magnesium alloys. *Corros. Sci.* **2009**, *51*, 2820–2825. [CrossRef]
11. Yang, W.; Xu, D.P.; Wang, J.L.; Yao, X.F.; Chen, J. Microstructure and corrosion resistance of micro arc oxidation plus electrostatic powder spraying composite coating on magnesium alloy. *Corros. Sci.* **2018**, *136*, 174–179. [CrossRef]
12. Yamauchi, N.; Ueda, N.; Okamoto, A.; Sone, T.; Tsujikawa, M.; Oki, S. DLC coating on Mg-Li alloy. *Surf. Coat. Technol.* **2007**, *201*, 4913–4918. [CrossRef]
13. Yang, W.; Gao, Y.; Guo, P.; Xu, D.P.; Wang, A.Y. Adhesion, biological corrosion resistance and biotribological properties of carbon films deposited on MAO coated Ti substrates. *J. Mech. Behav. Biomed.* **2020**, *101*, 103448. [CrossRef] [PubMed]
14. Liu, D.J.; Jiang, B.L.; Liu, Z.; Ge, Y.F.; Wang, Y.M. Preparation and catalytic properties of Cu_2O-CoO/Al_2O_3 composite coating prepared on aluminum plate by microarc oxidation. *Ceram. Int.* **2014**, *40*, 9981–9987. [CrossRef]
15. Durdu, S.; Usta, M. Characterization and mechanical properties of coatings on magnesium by micro arc oxidation. *Appl. Surf. Sci.* **2012**, *261*, 774–782. [CrossRef]
16. Guo, H.F.; An, M.Z.; Huo, H.B.; Xu, S.; Wu, L.J. Microstructure characteristic of ceramic coatings fabricated on magnesium alloys by micro-arc oxidation in alkaline silicate solutions. *Appl. Surf. Sci.* **2006**, *252*, 7911–7916. [CrossRef]
17. Gao, Y.H.; Li, W.F.; Du, J.; Zhang, Q.L.; Jie, J. Preparation and micro-structures of yellow ceramic coating by micro-arc oxidation. *J. Mater. Sci. Eng.* **2005**, *23*, 542–545. (In Chinese)
18. Yan, F.Y.; Fan, S.Y.; Zhang, W.Q.; Zhang, Y.H. Preparation of green micro-arc oxidation ceramic coating on magnesium alloy. *Mater. Prot.* **2008**, *41*, 4–6. (In Chinese)
19. Han, J.X.; Cheng, Y.L.; Tu, W.B.; Zhan, T.Y.; Cheng, Y.L. The black and white coatings on Ti-6Al-4V alloy or pure titanium by plasma electrolytic oxidation in concentrated silicate electrolyte. *Appl. Surf. Sci.* **2018**, *428*, 684–697. [CrossRef]
20. Tu, W.B.; Cheng, Y.L.; Wang, X.Y.; Zhan, T.Y.; Han, J.X.; Cheng, Y.L. Plasma electrolytic oxidation of AZ31 magnesium alloy in aluminate-tungstate electrolytes and the coating formation mechanism. *J. Alloy. Compd.* **2017**, *25*, 199–216. [CrossRef]
21. Li, J.M.; Cai, H.; Jiang, B.L. Growth mechanism of black ceramic layers formed by micro arc oxidation. *Surf. Coat. Technol.* **2007**, *201*, 8702–8708. [CrossRef]
22. Yang, W.; Xu, D.P.; Chen, J.; Liu, J.N.; Jiang, B.L. Characterization of self-sealing MAO ceramic coatings with green or black color on an Al alloy. *RSC Adv.* **2017**, *7*, 1597–1605. [CrossRef]
23. Yang, W.; Wang, J.L.; Xu, D.P.; Li, J.H.; Chen, T. Characterization and formation mechanism of grey micro-arc oxidation coatings on magnesium alloy. *Surf. Coat. Technol.* **2015**, *283*, 281–285. [CrossRef]

24. Yang, W.; Xu, D.P.; Yao, X.F.; Wang, J.L.; Chen, J. Stable preparation and characterization of yellow micro arc oxidation coating on magnesium alloy. *J. Alloy. Compd.* **2018**, *745*, 609–616. [CrossRef]
25. Lee, S.J.; Do, L.H.T. Effects of copper additive on micro-arc oxidation coating of LZ91 magnesium-lithium alloy. *Surf. Coat. Technol.* **2016**, *307*, 781–789. [CrossRef]
26. Li, Q.B.; Yang, W.B.; Liu, C.C.; Wang, D.A.; Liang, J. Correlations between the growth mechanism and properties of micro-arc oxidation coatings on titanium alloy: Effects of electrolytes. *Surf. Coat. Technol.* **2017**, *316*, 162–170. [CrossRef]
27. Chen, W.W.; Wang, Z.X.; Sun, L.; Lu, S. Research of growth mechanism of ceramic coatings fabricated by micro-arc oxidation on magnesium alloys at high current mode. *J. Magn. Alloy.* **2015**, *3*, 253–257. [CrossRef]
28. Yang, W.; Xu, D.P.; Guo, Q.Q.; Chen, T.; Chen, J. Influence of electrolyte composition on microstructure and properties of coatings formed on pure Ti substrate by micro arc oxidation. *Surf. Coat. Technol.* **2018**, *349*, 522–528. [CrossRef]
29. Tao, X.J.; Li, S.J.; Zheng, C.Y.; Fu, J.; Guo, Z.; Hao, Y.L.; Yang, R.; Guo, Z.X. Synthesis of a porous oxide layer on a multifunctional biomedical titanium by micro-arc oxidation. *Mat. Sci. Eng. C Mater.* **2009**, *29*, 1923–1934. [CrossRef]
30. Veys-Renaux, D.; Barchiche, C.E.; Rocca, E. Corrosion behavior of AZ91 Mg alloy anodized by low-energy micro-arc oxidation: Effect of aluminates and silicates. *Surf. Coat. Technol.* **2014**, *251*, 232–238. [CrossRef]
31. Shokouhfar, M.; Allahkaram, S.R. Formation mechanism and surface characterization of ceramic composite coatings on pure titanium prepared by micro-arc oxidation in electrolytes containing nanoparticles. *Surf. Coat. Technol.* **2016**, *291*, 396–405. [CrossRef]
32. Yan, W.G.; Jiang, B.L.; Li, H.T.; Shi, W.Y. Exfoliation of ceramic layers formed by micro-arc oxidation under cathode environment. *Hot Working Technol.* **2017**, *46*, 158–161.
33. Shen, Y.; Wang, H.X.; Pan, Y.P. Effect of current density on the microstructure and corrosion properties of MAO coatings on aluminum alloy shock absorber. *Key Eng. Mater.* **2018**, *764*, 28–38. [CrossRef]

materials

MDPI

Article

Corrosion Resistance and Apatite-Forming Ability of Composite Coatings formed on Mg–Al–Zn–Ca Alloys

Anawati Anawati [1,*], Hidetaka Asoh [2] and Sachiko Ono [2]

[1] Department of Physics, Faculty of Mathematics and Natural Sciences, Universitas Indonesia, Depok 16424, Indonesia
[2] Department of Applied Chemistry, Kogakuin University, 2665-1 Nakano, Hachioji, Tokyo 192-0015, Japan
* Correspondence: anawati@sci.ui.ac.id; Tel./Fax: +62-21-3193-8136

Received: 15 June 2019; Accepted: 10 July 2019; Published: 14 July 2019

Abstract: The properties of composite coatings formed by plasma electrolytic oxidation (PEO) were affected by the alloy composition. The corrosion resistance and apatite-forming ability of PEO coatings formed on Mg–6Al–1Zn–xCa alloys with a variation of Ca content were investigated. Potentiodynamic polarization and electrochemical impedance spectroscopy (EIS) measurements showed an order magnitude improvement of corrosion resistance in the AZ61 alloy as a result of the coating. A higher enhancement in polarization resistance was obtained in the Mg–6Al–1Zn–1Ca and Mg–6Al–1Zn–2Ca alloys due to thicker coatings were formed as a result of the incorporation of calcium oxide/hydroxide. However, the underlying substrates were more prone to localized corrosion with increasing Ca content. The microstructure investigation revealed an enlargement in precipitates (Al_2Ca, Mg_2Ca) sizes with increasing Ca content in the alloys. The growth of larger size precipitates increased the danger to micro galvanic corrosion. Apatite layers were formed on all of the coatings indicating high apatite-forming ability, but the layers formed on the Mg–6Al–1Zn–1Ca and Mg–6Al–1Zn–2Ca alloys contained higher Mg, possibly due to the accumulation of corrosion product, than that on the Mg–6Al–1Zn alloy. The alloying element Ca should be limited to 1 wt.% as the excess tended to degrade the corrosion resistance and apatite-forming ability of the PEO coating.

Keywords: magnesium; microstructure; coating; corrosion; polarization; apatite

1. Introduction

The use of magnesium (Mg) and its alloys for biodegradable materials rely on the surface treatment such as plating, coating, and anodizing, due to the high corrosion rate of Mg in aqueous environments [1–3]. Among the available techniques, plasma electrolytic oxidation (PEO) becomes famous for corrosion protection of Mg alloys considering its flexibility to coat complex geometry and environmentally friendly process [4,5]. The PEO coating that forms as a result of high-voltage (hundreds volt) anodization in an alkaline electrolyte, with the incorporation of the electrolyte species, provides superior corrosion and wear resistance [6–8]. A ceramic-like composite layer consisting of crystalline and amorphous oxides is developed under the exposure of a high-temperature plasma discharge. The corrosion resistance of the PEO coating depends on the processing parameters [9], alloy composition [10], and the type of electrolyte used [11]. Among various alkaline electrolytes, the PEO coating formed in phosphate-based solution exhibited the highest corrosion resistance due to the significant formation of crystalline magnesium phosphate [12]. Magnesium phosphate is a biocompatible compound and has attracted much attention during the past few years as a material for bone replacement [13]. However, both the in vitro [7,14] and in vivo [15,16] tests have indicated that the deposition of bone mineral apatite ($Ca_{10}(PO_4)_6$) on the PEO coating was limited. The apatite-forming ability defines the bioactivity of biomaterials.

Various methods have been proposed to accelerate the bioactivity of the PEO coating in physiological solution such as by coating with apatite [17,18], incorporating Ca [19,20] or apatite [21,22] in the coating, and introducing Ca as an alloying element [23]. The unstable Ca compounds easily dissolves in the electrolyte during plasma discharge and therefore adding Ca in the electrolyte bath is not beneficial. Incorporation of apatite in the PEO coating improved the corrosion resistance, but long-term immersion in simulated body fluid (SBF) indicated no further growth of the apatite [19,20]. Apart from the coating modification during the PEO process, the effect of Ca as an alloying element in Mg in modifying the bioactivity of the coating has not been thoroughly investigated. Our previous result [23] showed an increase in the bioactivity of the PEO coating on Mg–6Al–0.26 Mn–xCa alloys with increasing Ca concentration in the alloys. An embodiment of Ca in the coating and its presence in the alloy accelerated the growth of apatite in simulated body fluid (SBF). However, short-term (8 min) grown coatings on Mg–6Al–1Zn–xCa alloys revealed no bioactivity in SBF and significantly high corrosion rate [24]. The reason for such behavior was still unclear. The alloying element Ca might have different effect on the microstructure, and hence the resulting PEO film of the Mg–Al–Zn alloys as compared to that of the Mg–Al–Mn alloys. The development of an Mg based-biodegradable implant included Zn as alloying element to improve its mechanical strength [25–27]. This work aims to throw light on explaining the corrosion behavior and apatite-forming ability of the coatings formed on the Mg–6Al–1Zn–xCa alloys as a result of alteration in the microstructure with a variation of Ca content.

2. Materials and Methods

2.1. Specimen Preparation

Rolled plates of Mg–6Al–1Zn–xCa alloys with the composition listed in Table 1 were used as substrates. For the sake of simplicity, the alloy was further designated as AZ61, AZX611, and AZX612 for the alloys containing 0, 1, and 2 wt.% Ca, respectively. The plate was cut into 5 cm^2 working area. For surface observation, the specimen was embedded in a resin and then ground to 1200-grit silicon carbide (SiC) paper. The specimen was then degreased in acetone in an ultrasonic bath for 3 min. The etching treatment was applied on the specimen using 4 vol.% HNO_3 in ethanol for 20 s to reveal the microstructure.

Table 1. Chemical composition of the alloys.

Element	AZ61	AZX611	AZX612
Mg	Bal.	Bal.	Bal.
Al	6.50	5.8–7.2	5.8–7.2
Zn	0.92	0.4–1.5	0.4–1.5
Mn	0.32	0.15–0.5	0.15–0.5
Cu	≤0.05	≤0.05	≤0.05
Ni	≤0.005	≤0.005	≤0.005
Fe	≤0.005	≤0.005	≤0.005
Si	≤0.1	≤0.1	≤0.1
Ca	-	1.0	2.0

2.2. Plasma Electrolytic Oxidation

To dissolve the natural oxide layer on the surface, the specimen was dipped in a mixed acid solution of 8 vol.% HNO_3-1 vol.% H_3PO_4 for 20 s, and then in 5 wt.% NaOH solution at 80 °C for 1 min. The PEO coating was developed under a galvanostatic mode at 200 Am^{-2} in 0.5 $mol{\cdot}dm^{-3}$ Na_3PO_4 solution at 25 °C for 20 min. A regulated DC power supply was used as the current source. The specimen was placed as an anode while a pair of carbon rod was used as cathode. The voltage output was measured by digital multimeter bench from Keithley series 2700. A coating thickness gauge of dual type (SME-1) from Sanko was used for determining the coating thickness.

2.3. Electrochemical Corrosion

The electrochemical corrosion measurement was performed by conducting potentiodynamic polarization and electrochemical impedance spectroscopy (EIS) tests in a physiological solution 0.9 wt.% NaCl solution at 37 °C based on ASTM G5 [28]. A defined surface with an area of 2.5 cm^2 was exposed to the solution. The electrochemical tests were performed by using a potentiostat instrument from IviumStat. Pt wire was used as a counter electrode, and silver chloride (Ag/AgCl) was used as a reference electrode. The electrochemical cell condition and arrangement were similar to as reported earlier [24]. Potentiodynamic polarization test was conducted from 100 mV below open circuit potential (OCP) and terminated when the current output reached 30 mA at a sweep rate of 1 $mV{\cdot}s^{-1}$. The corrosion potential and current density were estimated by using Tafel extrapolation. The EIS was performed on the uncoated substrates at an open circuit potential (OCP) over a frequency ranging from 10^{-2} Hz to 10^4 Hz. Prior to the tests, the specimen was left at an OCP for 40 min to stabilize the potential. The coated specimen did not give spectra at low frequency and therefore was analyzed at frequency range 10^2 to 10^7 Hz.

2.4. Apatite-Forming Ability Test

The apatite-forming ability test was performed by immersing the specimens individually in SBF at 37 °C with a surface-to-volume ratio of 20 mL/cm^2 for 14 days. An SBF10, with the ionic concentration shown in Table 2, was used. The solution preparation followed the Reference [29]. The fresh solution pH was adjusted to 7.4 at 37 °C. The solution was replaced after 1, 3, 5, 7, 10, and 12 days, and was collected each time after each replacement for further analysis. The Mg concentration dissolved in the solution was analyzed by using the titration method. A digital titration kit from Hach, which included a digital titrator, buffer solutions, and indicators, was used. The solution was titrated with 0.08 M of sodium ethylenediaminetetraacetic acid (EDTA) using a digital titrator. The method was able to detect Mg concentrations within a 1 ppm margin of error.

Table 2. Ionic composition of simulated body fluid (SBF).

Ion	Na^+	K^+	Mg^+	Ca^+	Cl^-	HCO_3^-	HPO_4^{2-}	SO_4^{2-}
Concentration (mM)	142	5	1	2.5	126	10	1	1

2.5. Surface Analyses

The surface microstructure and the elemental composition was studied by an energy dispersive X-ray spectroscopy (EDS, JEOL EX-54175JMU, Tokyo, Japan) attached to the SEM (JEOL JSM-6380LA, Tokyo, Japan). The crystalline phases in the specimens were analyzed using thin coating X-ray diffraction analysis (TF-XRD, Rint 2000 Rigaku type, Tokyo, Japan) at an incident angle of 1°. The phases existed in the specimens were analyzed by indexing the peaks in the XRD pattern by referring to the JCPDS cards. Depth profile analysis on the coatings was performed on a circular area with a diameter of 4 mm using glow-discharge optical emission spectroscopy (GDOES, Jobin-Yvon JY5000RF, Horiba, Ltd., Kyoto, Japan). Sputtering was done using Ar^+ ion at 40 W.

3. Results

3.1. Alloy Microstructure

Figure 1 shows the X-ray diffraction (XRD) pattern of AZ61, AZX611, and AZX612 alloys and the optical microscope images showing the microstructure of the alloys. All of the alloys consisted of primary α-Mg phase and secondary β-phase ($Al_{12}Mg_{17}$). Precipitation of Ca-containing intermetallic, Al_2Ca and Mg_2Ca, was detected in the AZX611 and AZX612 alloys. The peaks for Al_2Ca and Mg_2Ca phases were quite small and often overlapped with the peaks for other phases. As opposed to the microstructure of AM60 alloy which contained a low number of precipitates [23], the Mg matrix of the

AZ61 alloy exhibited an ultrafine equiaxed grain with the average grain size ~3 μm × 5 μm decorated by numerous spherical intermetallic $Al_{12}Mg_{17}$ phase with diameters approximately 0.5 μm as shown in Figure 1b. The presence of 1 wt.% Ca expanded the grain size about an order of magnitude, but no further enlargement with increasing Ca content to 2 wt.%. The XRD pattern of AZX611 and AZX612 alloys displayed a higher intensity in the Mg peaks confirming larger metallic grain sizes than that of the base alloy. The equiaxed grains size in both AZX611 and AZX612 alloy was approximately 50 μm × 250 μm. The grain boundaries became thicker with increasing Ca content in the alloys due to segregation of the intermetallic precipitates (Figure 1c,d). The XRD pattern of Ca-containing alloys revealed some additional β-phase peaks emerged at 23.7°, 40.0°, 42.0°, 43.7°, 61.6°, 63.3°, 64.9°, 66.4°, and 67.8° indicating a higher amount of β phase existed in the alloys.

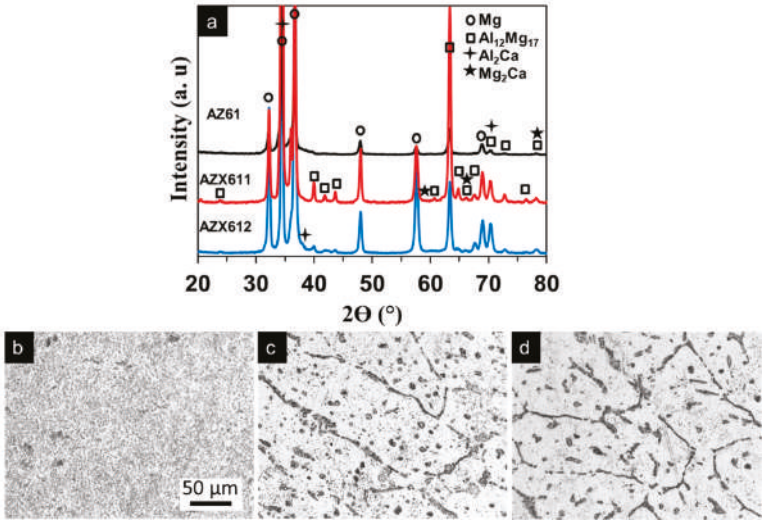

Figure 1. (**a**) X-ray diffraction pattern and surface microstructure of (**b**) AZ61, (**c**) AZX611, and (**d**) AZX612 alloys. The scale bar in image (b) applied to images (c) and (d).

Figure 2 shows the SEM images and the corresponding EDS maps for the elements Mg, Al, and Ca, showing the element composition of the three alloys. In the maps, blue represents Mg, red represents Al, and the green represents Ca. The AZ61 alloy shows a high density of precipitates on its surface. The maps displayed a nearly uniform blue and red maps corresponded to the β precipitate smeared in the matrix. The size of precipitates became larger with increasing Ca content in the alloys, and the matrix became clearer from precipitates. The maps for AZX611 and AZX612 showed that the intermetallic consisted of Mg, Al, and Ca. This analysis proved the unambiguous presence of Al_2Ca and Mg_2Ca precipitates besides the β phase in both AZX611 and AZX612 alloys. The amount of Al_2Ca phase dominated over Mg_2Ca phase.

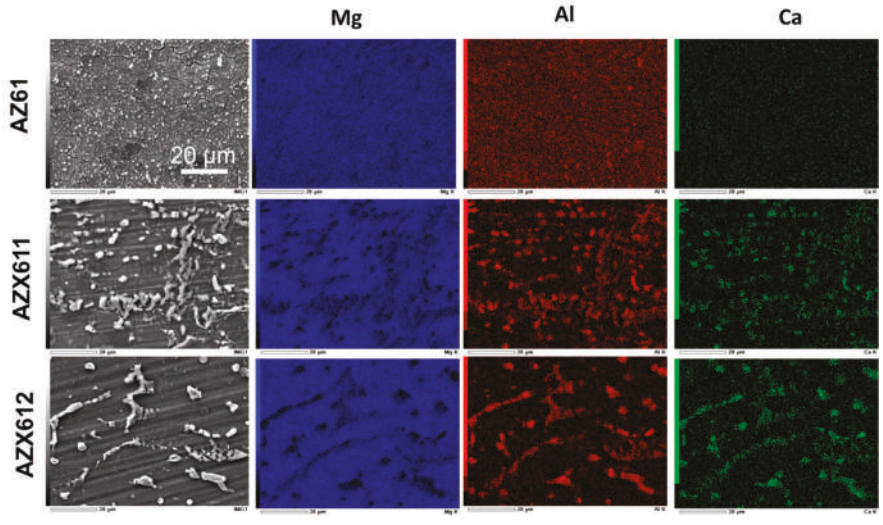

Figure 2. Plane-view SEM images and the corresponding EDS maps for Mg (blue), Al (red), and Ca (green), of AZ61, AZX611, and AZX612 alloys. The scale bar applied to all images.

3.2. PEO-Coating Structure and Composition

The voltage–time curves recorded during the PEO coating on the three alloys are depicted in Figure 3. Above the breakdown voltage (90 V), plasma discharge was developed at a few spots on the specimen surface, indicating the beginning of the electrolytic process. After the discrete plasma formed uniformly on the surface, the voltage stabilized at ~150 V. Strong plasma discharge began to occur at a critical voltage after about 9 min where large oscillation in the voltage (150–250 V) was attained. The presence of 1 wt.% Ca in the alloys shifted the critical voltage towards a longer time of approximately 2 min; however, the curve did not shift any further when the amount of Ca was increased to 2 wt.%.

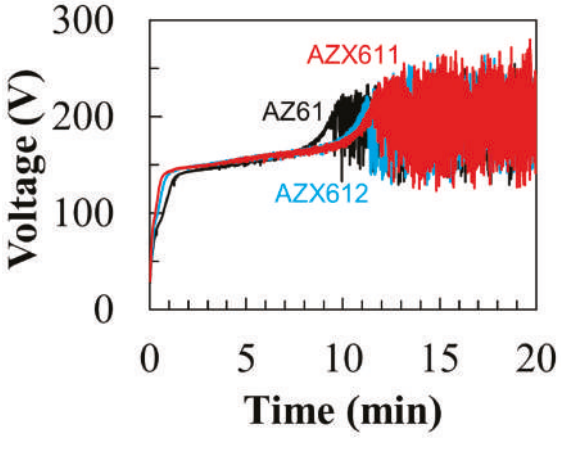

Figure 3. Voltage–time curves during 20 min anodization of AZ61, AZX611, and AZX612 alloys in 0.5 M Na_3PO_4 solution at 25 °C.

Figure 4 displays the XRD pattern of the resulting coatings formed on the three alloys and the cross-sectional FE-SEM images of the coatings. Most of the peaks for substrates no longer appeared in the XRD pattern of the coated specimens indicating an excellent blocking effect of the coatings from the X-ray. The composition of the coatings formed on the three alloys were similar, which were composed of both crystalline and amorphous phases as shown by the appearance of the broad peak between 20° and 40°, which attributed to the amorphous phase, and the small peaks inside the broad peak corresponded to the crystalline oxide phases of $Mg_3(PO_4)_2$ and $Mg(PO_3)_2$. The coatings that formed on all of the specimens exhibited a similar uneven structure, as shown in Figure 4b–d. Pores and cracks, which are the footprint of PEO coating, were observed on both the surface and inner part of the coating. Fine cracks were developed during the PEO process, while heavy cracks occurred unintentionally during specimen preparation. The coating formed on Ca-containing alloys was slightly thicker than that of the base alloy. In agreement with the cross-section images, the average coating thickness measured by coating thickness gauge were 25, 32, and 30 μm for the coating formed on AZ61, AZX611, and AZX612, respectively. The XRD analysis did not detect the presence of Ca in the coating, similar to the earlier result on AM60 [23]. The Ca compounds may have been present in an amorphous state.

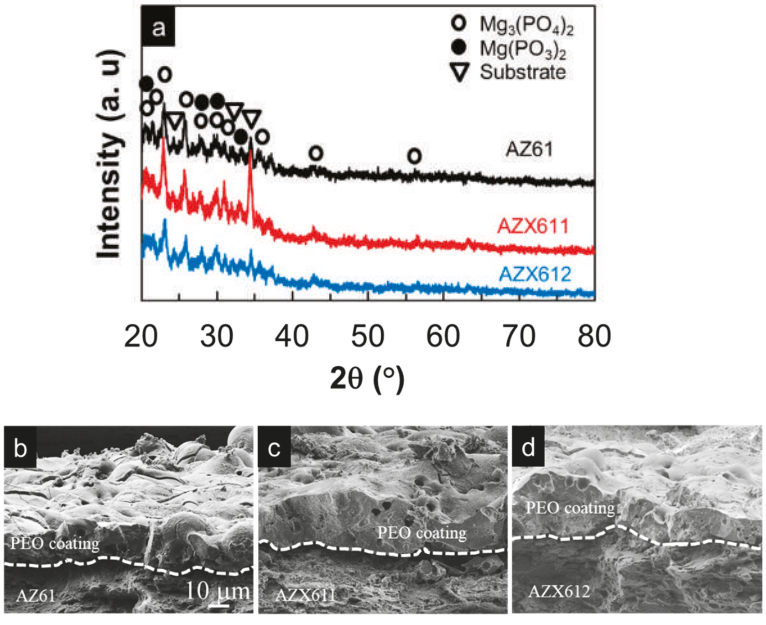

Figure 4. (**a**) X-ray diffraction pattern of plasma electrolytic oxidation (PEO) coatings and the corresponding cross-section FE-SEM images of the coating on (**b**) AZ61, (**c**) AZX611, and (**d**) AZX612 resulting from 20 min anodization in 0.5 M Na_3PO_4 solution at 25 °C. The scale bar applied to all images.

The coatings composition was further analyzed by depth profile GDOES, and the results are displayed in Figure 5. The dashed line marks the coating–metal interface at which the O and Mg profiles crossed each other. All of the coatings were composed of Mg, P, O, and Al. Confirming XRD results, the primary oxide phases in the coatings consisted of Mg–O compounds. The GDOES profile suggested the presence of other oxide phases, including MgO and Al_2O_3 in the amorphous state. The incorporation of Ca in the coating of AZX611 and AZX612 alloys was confirmed by the Ca profiles in Figure 5b,c. The intensities of Ca signal in the AZX611 and AZX612 coatings was about half of their bulk values, which verified the presence of calcium oxide/hydroxide phase in the coatings. The

coating-metal interface shifted twice towards longer sputtering times from 400 s for AZ61 to 950 s for AZX611 and 900 s for AZX612 specimens. The shift indicated an increase in coating thickness as the thicker coating needs longer sputtering time to reach the bulk substrate.

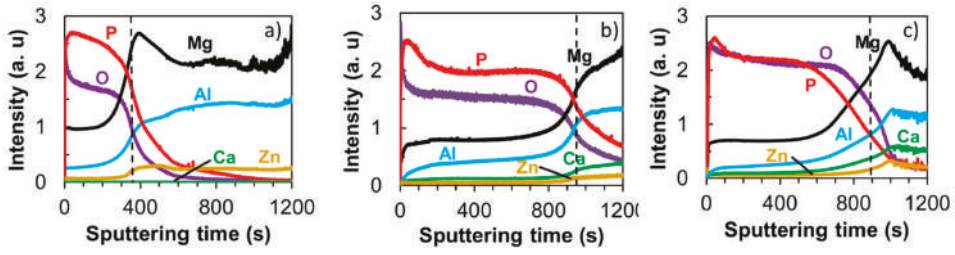

Figure 5. Glow-discharge optical emission spectroscopy (GDOES) elemental depth profiles of PEO coatings on (**a**) AZ61, (**b**) AZX611, and (**c**) AZX612 specimens after anodization in 0.5 mol·dm^{-3} Na_3PO_4 solution at 25 °C for 20 min. The dashed lines indicate the oxide–metal interface.

3.3. Electrochemical Corrosion

The corrosion behavior of the PEO coating was investigated by potentiodynamic polarization test in 0.9 wt.% NaCl solution at 37 °C. Figure 6 shows the corrosion potential and current densities data obtained from the polarization curves of the specimens before and after coating. The corrosion potentials of the substrates became slightly nobler from −1.49 to −1.45 $V_{Ag/AgCl}$ with increasing Ca content in the alloys. The behavior was preserved after coating that the corrosion potential increased with Ca content in the alloys from −1.66 to −1.64 $V_{Ag/AgCl}$ (Figure 6a). The corrosion current densities of the coated specimens were 10 times lower than that of the substrates. The substrates exhibited corrosion current densities in the range of 2.0×10^{-5} to 3.5×10^{-5} A·cm^{-2} while the coated specimens were in the range of 3.5×10^{-6} to 3.6×10^{-6} A·cm^{-2}. Depression of corrosion potential, which was accompanied by a reduction in corrosion current densities as a result of PEO coating, indicated an improvement in corrosion resistance of the alloys. The inhibition of cathodic reaction on the surface suppressed the corrosion potential of the coated specimens to the negative direction.

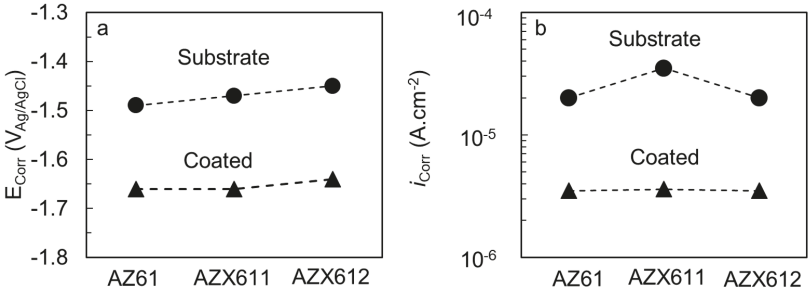

Figure 6. (**a**) Corrosion potentials and (**b**) corrosion current densities of the substrates and coated specimens of AZ61, AZX611, and AZX612 alloys.

The coating resistance was evaluated by EIS measurement in 0.9 wt.% NaCl solution at 37 °C. The results are displayed in Figure 7 for uncoated, and Figure 8 for the coated, specimens. The fitted parameters obtained from the EIS data are listed in Table 3. The n1 and n2 refers to constant phase for CPE1 and CPE2, respectively. The maximum n value is 1. The closer to 1 the n1 and n2 value is, indicates more capacitive behavior. The polarization resistance (R1) of the coated specimens was an order of magnitude higher than that of their substrates. The base alloy exhibited the highest polarization resistance in both uncoated and coated conditions relative to the Ca-containing alloys. The

impedance spectrum of AZ61 substrate exhibited one apparent capacitive loop, while the Ca-containing alloys showed an additional inductive loop at low frequency. The corresponding inductive loop is an indication of localized corrosion [5,8]. The presence of inductive loop lowered the n2 values for AZX611 and AZX612 specimens compared to the AZ611 specimen. The presence of a constant phase element (CPE) in parallel with a resistance indicates the presence of a faradaic reaction (charge transfer) and a non-Faradaic reaction (charge accumulation at the interface) occurring at the interface. All of the three PEO coatings exhibited a similar trend of impedance spectrum. The L and R_L loops did not exist in the model for the PEO coating (Figure 8), indicating high resistance to metal dissolution. Moreover, a much higher impedance at low and medium frequencies of the Bode plot and an enlarged diameter of the semicircle in the Nyquist plot of the coated specimens are evidence of remarkable higher corrosion resistance than that of the substrates. Moreover, the capacitance values of the coated specimens were a hundred times lower than that of the substrates. The effect of the alloying Ca in the coating impedance was displayed by the Bode plot in Figure 8. The impedance at high frequencies, which represents the outer PEO coating of all the coated specimens, was similar. However, the impedance at low frequencies displayed slightly lower impedance than that of the AZ61 specimen. The results implied that the coating–metal interface of the Ca-containing specimens was more prone to localized corrosion than that of the base specimen.

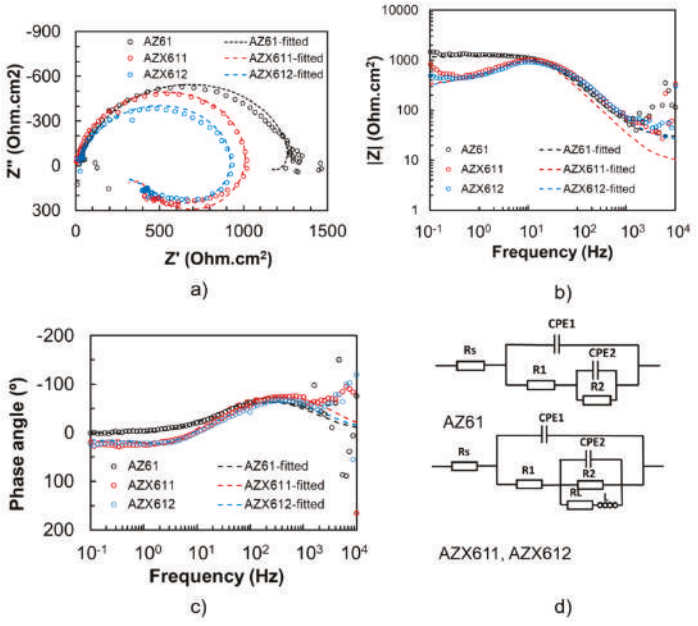

Figure 7. Electrochemical impedance spectra of uncoated specimens of AZ61, AZX611, and AZX612 specimens: (**a**) Nyquist plots, (**b**) bode plots, and (**c**) phase plots, and (**d**) the equivalent circuit.

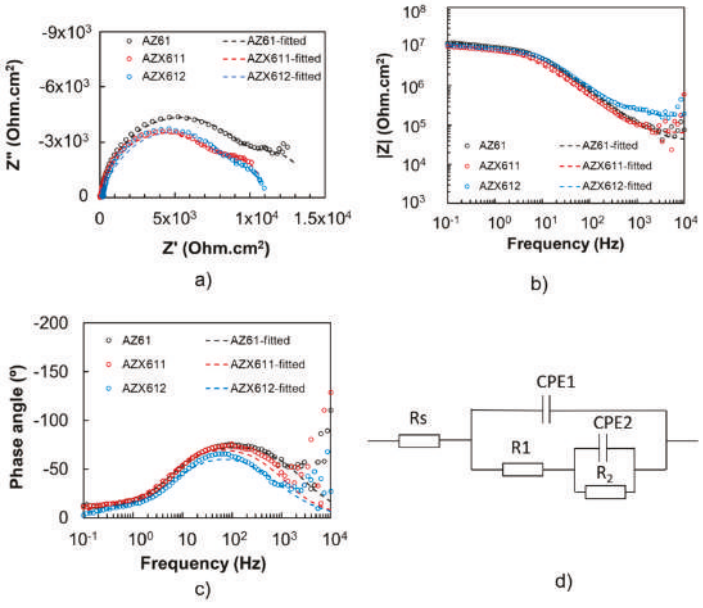

Figure 8. Electrochemical impedance spectra of coated specimens of AZ61, AZX611, and AZX612 specimens: (**a**) Nyquist plots, (**b**) bode plots, and (**c**) phase plots, and (**d**) the equivalent circuit.

Table 3. Parameter of the fitted plotting of EIS spectra.

Specimen	Rs (Ωcm^2)	CPE1 ($\Omega^{-1}s^n cm^{-2}$)	n_1	R1 (Ωcm^2)	CPE2 ($\Omega^{-1}s^n cm^{-2}$)	n_2	R2 (Ωcm^2)	L (H)	RL (Ωcm^2)
AZ61	28.25	9.78×10^{-6}	0.88	1.32×10^3	-1.00×10^{-3}	0.81	−200	-	-
AZX611	9.40	7.68×10^{-6}	0.94	1.10×10^3	-1.00×10^{-3}	0.75	−1000	15	700
AZX612	25.0	8.00×10^{-6}	0.88	1.00×10^3	-6.00×10^{-4}	0.75	−725	20	950
AZ61 (Coated)	40.5	1.09×10^{-9}	0.87	1.04×10^4	3.67×10^{-7}	0.91	3.61×10^3	-	-
AZX611 (Coated)	61.9	1.64×10^{-9}	0.87	8.4×10^3	2.48×10^{-7}	0.96	2.61×10^3	-	-
AZX612 (Coated)	163.8	1.97×10^{-9}	0.82	9.45×10^3	3.67×10^{-7}	0.99	1.41×10^3	-	-

3.4. Apatite-Forming Ability

The apatite-forming ability of the coated specimens was evaluated by immersion test in XRD. The concentration of Mg dissolved from the surface, and the pH solution during the immersion test in SBF was monitored. Figure 9 displays the concentration of Mg detected in the solution and the pH solution during 14 days of immersion. The AZ61 alloy released the lowest Mg concentration in the range of 100–150 mg/L indicating the lowest corrosion rate relative to the two Ca-containing alloys, which released 100–500 mg/L Mg into the solution (Figure 9a). The solution pH of the three alloys increased from 7.4 to 8 after one-day immersion indicating high corrosion activities (Figure 9c). The increase in pH occurred due to the release of hydrogen gas during hydrolysis of Mg ions following the corrosion attack. The pH change was not significant as the solution was buffered. The solution pH of AZ61 alloy decreased, approaching the fresh SBF while that of the AZX611 and AZX612 alloys fluctuated with increasing immersion time. On average, the lowest pH was attained in the AZ61 alloy. The PEO-coated specimens released much lower Mg into the solution relative to their substrates (Figure 9b). In agreement, the solution pH of the coated specimen was relatively lower compared to the substrates during the 14-day immersion. The dissolved Mg in the solution was attributed to both corrosion of the underlying substrate and the coating dissolution. The coated AZ61 specimen released 110 to 200 mg/L Mg at the initial immersion time and then stabilized at day 7 to 12. Dissolution no longer occurred at day 14. The coating on AZX611 specimen exhibited a relatively constant dissolution rate during

1–12 days followed by passivation at the end period of the test. The AZX612 specimen exhibited a dynamic dissolution resulting in a highly fluctuating concentration of the dissolved Mg in the range 300–450 mg/L. All of the coatings exhibited the tendency for passivation at day 14 with solution pH at 7.7, which was presumably due to surface coverage by the apatite layers on their surfaces.

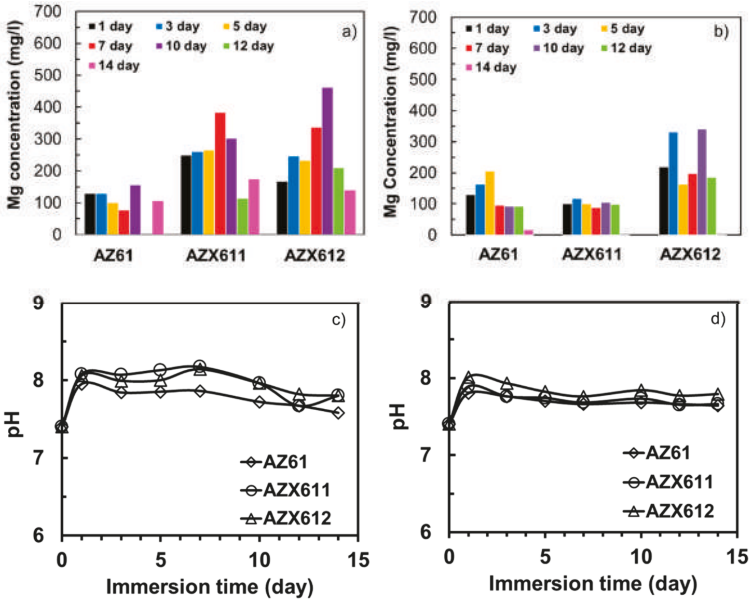

Figure 9. Concentration of Mg dissolved during immersion testing in SBF of the (**a**) substrates, (**b**) coated specimens, and the corresponding solution pH for (**c**) the substrates and (**d**) coated specimens.

The presence of apatite on the PEO coating was investigated by observing the surface morphology and analyzing the surface composition after the immersion test. Figure 10 shows the SEM images at different magnifications revealing the presence of uniform apatite layer on all of the three coatings. Most of the pores that existed in the coating of AZ61 specimen were no longer viewed, indicating surface coverage by thick apatite layer (Figure 10a). The layer formed uniformly following the coating structure, as shown clearly in Figure 10b. The spongy structure with scallop type of grain, which was a typical morphology of apatite formed in SBF was seen in a higher magnification image in the inset Figure 10b. The coating remained intact and protected by the apatite layer. Thinner apatite layers were formed on AZX611 and AZX612 specimens as inferred from the existence of open pores and cracks in the coating (Figure 10c,e). The scallop grain of apatite layer in the AZX611 and AZX612 specimens was smaller than that of formed in AZ61 specimen as shown in the inset image of Figure 9d,f. Localized coating damage was recognized at a few spots, pointed by arrows in the images. The AZX611 specimen showed relatively small coating deterioration while larger coating damage on an area approximately 150 μm × 300 μm was observed on AZX612 specimen.

Figure 11 shows the results of EDS analysis from the areas shown in Figure 10 as compared to that of fresh PEO coating. The observation areas for both cases were kept identical by using similar magnification scale. Prior to the immersion test, calcium was not detected in any of the coatings (Figure 11a). The signal attributed to the calcium oxide phase in the coating was weak relative to the other elements. After 14 days immersion in SBF, the Ca signal was detected as high as 8.0, 7.2, and 3.1 at.% in AZ61, AZX611, and AZX612 specimens, respectively, attributed to the apatite layer shown in Figure 10. The Mg concentration increased from 6.8 at.% in the AZ61 to 12.5 at.% in the AZX611 specimens. The concentration of P was relatively not altered at 12–13 at.%. The ratios of Ca/P of the

apatite layers were 0.65, 0.60, and 0.24 for the layers formed on AZ61, AZX611, and AZX612 specimens, respectively. The ratio was half of the stoichiometry apatite, 1.67 [30]. The apatite layer that formed in the coating of AZX611 and AZX612 alloys contained more Mg than that of the AZ61 alloy. Moreover, the strong signal of P derived from the underlying PEO coating lowered the Ca/P ratio.

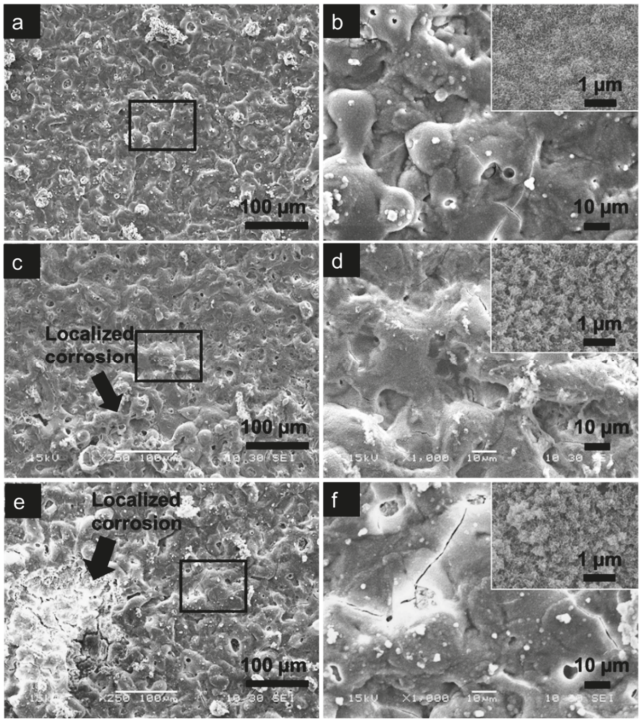

Figure 10. SEM images of PEO coatings on (**a**) and (**b**) AZ61, (**c**) and (**d**) AZX611, and (**e**) and (**f**) AZX612 specimens after 14 days of immersion in SBF showing the corrosion morphology. (b), (d), (f) are higher magnification images of the area inside the rectangle in images (a), (c), (e), respectively. The inset image shows the apatite layer structure.

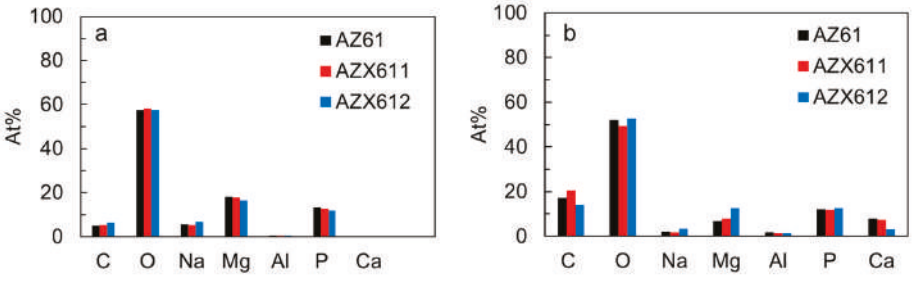

Figure 11. Atomic fraction of elements detected by EDS analysis on PEO coatings of AZ61, AZX611, and AZX612 specimens (**a**) before and (**b**) after 14 days immersion in SBF.

4. Discussion

Surface characterization showed that the coatings formed on all the three alloys exhibited similar uneven structure decorated with pores and cracks, but the composition and thickness were altered

by the presence of Ca in the alloys. The coatings composed of a mixed crystalline and amorphous phase. The $Mg_3(PO_4)_2$ and $Mg(PO_3)_2$ existed in both crystalline and amorphous states as confirmed by XRD analysis, while MgO and Al_2O_3 were present in an amorphous state as detected by GD-OES and EDS analysis. The presence of Ca in the alloys induced the formation of amorphous calcium oxide/hydroxide phase in the coatings. The depth profile analysis by GD-OES (Figure 5) confirmed the presence of calcium oxide/hydroxide from the surface throughout the coating-metal interface. At identical anodization time, the resulting coating on the AZX611 alloy was 7 μm thicker than that of the base alloy. The coating did not thicken any further in the AZX612 alloy, as no further substantial change in the Ca content of the solid solution matrix.

The microstructure observation revealed that the alloying element Ca decreased the density of intermetallic precipitates in the AZ61 alloys by inducing larger precipitates size and enlarging the metallic grain. The grain size expanded about 30–50 times by the presence of 1 wt.% Ca in the alloy. The substitute Ca atom with atomic diameter larger than Mg atom [31] caused expansion in the matrix grain size. The high number of submicron-sized precipitates in the AZ61 alloy transformed into a low number of 10 micron-sized precipitates as a result of alloying with 1 wt.% Ca (Figure 2). The precipitates grew slightly larger, but the metallic grain size remained the same, with increasing Ca concentration to 2 wt.%. The enlargement of grain size was controlled by the amount of dissolved Ca in the solid solution matrix. The precipitates continued to grow as more excess of Ca existed in the AZX612 alloy. The limited solubility of Ca in Mg, which is only 0.8 wt.% [32], induced the formation of Al_2Ca precipitates. With increasing Ca content, the bigger precipitates grew larger at the expense of the smaller ones following Ostwald ripening [33]. Another intermetallic phase Mg_2Ca also existed in the AZX611 and AZX612 alloys, but only in a small number. The large misfit in atomic size between Ca and Mg in which the diameter of the Ca atom is 20% larger than Mg, is less favorable for the formation of Mg_2Ca phase [31]. The presence of heat-resistant Al_2Ca and Mg_2Ca phases delayed the formation of strong plasma discharge during electrolytic process resulting in a less crystalline oxide phases in the coatings. Moreover, the presence of Mg_2Ca phase is not beneficial from the corrosion viewpoints as it is more anodic than the Mg matrix [2].

During the PEO formation, Mg and Ca in the solid solution matrix was selectively oxidized. From thermodynamic viewpoints, Ca is easier to oxidize as it has lower Gibbs free energy than Mg [33]. However, since the concentration of Ca in the solid solution matrix was limited by its solubility, the resulting calcium oxide/hydroxide in the coating was relatively small compared to the magnesium phosphate/oxide phases. The GD-OES depth profile was proved to be a sensitive technique in detecting the calcium oxide/hydroxide. The calcium oxide/hydroxide phases presumably occurred during the 12 min exposure in fine plasma discharge. The strong discharge, which occurred in the latter stage, tended to dissolve the calcium oxide/hydroxide to the solution. The incorporation of calcium oxide/hydroxide contributed to the thickening of the coating formed on AZX611 and AZX612 alloys relative to the AZ61 alloy.

The higher resistivity offered by the thicker coating formed on the AZX611 and AZX612 alloys was counteracted by the vulnerability of their metal substrates to localized corrosion relative to the AZ61 alloy. The polarization coating resistance of the coated AZ61 specimen was higher than that of the AZX611 and AZX612 specimens. The enlargement of precipitates in the AZX611 and AZX612 alloys increased the contact area of galvanic coupling between the precipitates and the matrix, and therefore increased the danger to micro galvanic corrosion when exposed to the corrosive solution. Ennoblement of corrosion potentials in the polarization curves of the AZX611 and AZX612 alloys due to the increase number of cathodic intermetallic was balanced by the increased susceptibility to localized corrosion. The presence of inductive loop in the EIS spectra of AZX611 and AZX612 alloys (Figure 7a), which was not present in the spectra of AZ61 alloy, was attributed to the localized corrosion. A small amount of big precipitates accelerates corrosion, whereas finely distributed precipitates retarded corrosion [34]. The coating–metal interface in the vicinity of the precipitates was less protective. Once the corrosive solution penetrated the coatings, pockets of the solution were developed at the interface. Corrosion of

the metal substrate occurred immediately as it was exposed to the solution inside the pockets. The increase in intermetallic precipitates size with Ca content in the alloys contributed to the enlargement of the attacked areas (Figure 10).

The higher corrosion rate of the underlying substrate limited the apatite-forming ability of the coatings on the AZX611 and AZX612 specimens. Even though a uniform apatite layer grew on all of the three coatings as a result of immersion in SBF, the layers that formed on the AZX611 and AZX612 coatings was thinner and contained higher Mg than that formed on the AZ61 coating. The incorporation of calcium oxide/hydroxide in the coatings did not necessarily enhance the bioactivity of the coatings, similar to that reported in Reference [19]. The corrosion rate of the underlying substrate is a more important factor in supporting the growth of apatite. An alternate corrosion rate of the underlying substrate, which released fluctuated hydrogen gas, tends to disturb the deposition of apatite on the coatings. In the case of AM60 alloys [23], the corrosion resistance of the PEO-coated specimens were relatively unaltered, and therefore the formation of apatite was not affected by the variation of Ca content in the alloys. During initial immersion time, thinning of the PEO coating occurred selectively at the amorphous part, leaving a rough crystalline oxide phase. The resulting sub-micron surface roughness became a preferential site for nucleation of apatite [14]. The apatite layer was likely to form on the coatings during 7–14 days immersion time where a constant dissolution rate of Mg was attained (Figure 9b). The released substances from the specimens contributed to increasing the degree of supersaturation of the SBF and the local pH, which triggered the deposition of apatite [30].

The following discussion led to the conclusion that the corrosion resistance of the PEO coatings formed on the AZ61 alloys was influenced by the concentration of alloying element Ca, in particular the concentration of the dissolved Ca in the solid solution matrix. Therefore, it is not necessary to add Ca above its solubility in Mg matrix. The Ca-containing precipitates that tended to shorten the lifetime of strong discharge during the PEO process resulted in the formation of lower crystalline oxide phases in the coating. A thinner PEO coating with a high-volume ratio of crystalline to amorphous phases gives much better corrosion resistance than a thicker coating with a lower ratio [12]. Addition of Ca above the solubility limit did not have a beneficial effect on the coating properties. On the contrary, the excess of Ca in the alloys resulted in the enlargement of Al_2Ca and Mg_2Ca precipitates, which tended to accelerate localized corrosion.

5. Conclusions

The PEO coating significantly enhanced the corrosion resistance of the Mg-6Al-1Zn-xCa (AZX) alloys relative to their substrates. The presence of 1 and 2 wt.% Ca in the alloys resulted in the formation of thicker coating, which contributed in higher enhancement of the coating resistance. However, the EIS spectra and the surface observation after the immersion test indicated an increased danger to localized corrosion with increasing Ca content in the alloys. The coating formed on AZX alloys exhibited lower polarization resistance than that which formed on the AZ61 alloy. After the 14-day immersion tests in SBF, the coating on AZ61 alloy remained intact while the coatings on AZX611 and AZX612 showed noticeable local damage. The microstructure investigation revealed that the alloying element Ca caused enlargement of metallic grain size and intermetallic precipitates relative to the AZ61 alloy. The increase in corrosion activities underneath the coatings lowered the apatite-forming ability of the AZX coatings, resulting in a thinner apatite layer formed during immersion in SBF.

Author Contributions: Conceptualization, A.A.; Methodology, A.A. Software, A.A. and S.O.; Validation, S.O.; Formal Analysis A.A., H.A. and S.O.; Investigation, A.A.; Resources, A.A. and S.O.; Data Curation: A.A.; Writing-Original Draft Preparation, A.A.; Writing-Review & Editing, A.A., H.A. and S.O.; Visualization, A.A.; Supervision, S.O.; Project Administration, A.A. and S.O.; Funding Acquisition, A.A. and S.O.

Funding: This research was supported by Direktorat Riset dan Pengabdian Masyarakat (DRPM) Universitas Indonesia through Q1Q2 Research grant 2019 (NKB-0266/UN2.R3.1/HKP.05.00/2019). Grant-in-Aid for Scientific Research from the Japan Society for the Promotion of Science and the Light Metal Education Foundation of Japan is acknowledged. We also thank a Strategic Research Foundation Grant-aided Project for Private Universities matching fund subsidy from the Ministry of Education, Culture, Sports, Science, and Technology of Japan.

Conflicts of Interest: The authors declare no conflict of interest.

References

1. Song, G. Control of biodegradation of biocompatable magnesium alloys. *Corros. Sci.* **2007**, *49*, 1696–1701. [CrossRef]
2. Kirkland, N.; Lespagnol, J.; Birbilis, N.; Staiger, M.; Kirkland, N. A survey of bio-corrosion rates of magnesium alloys. *Corros. Sci.* **2010**, *52*, 287–291. [CrossRef]
3. Witte, F.; Hort, N.; Vogt, C.; Cohen, S.; Ulrich, K.; Willumeit, R.; Feyerabend, F. Current Opinion in Solid State and Materials Science Degradable biomaterials based on magnesium corrosion. *Curr. Opin. Solid State Mater. Sci.* **2008**, *12*, 63–72. [CrossRef]
4. Patel, J.L.; Saka, N. Microplasmic ceramic coating. *Int. Ceram. Rev.* **2001**, *50*, 398–401.
5. White, L.; Koo, Y.; Neralla, S.; Sankar, J.; Yun, Y. Enhanced mechanical properties and increased corrosion resistance of a biodegradable magnesium alloy by plasma electrolytic oxidation (PEO). *Mater. Sci. Eng. B* **2016**, *208*, 39–46. [CrossRef] [PubMed]
6. Echeverry-Rendon, M.; Duque, V.; Quintero, D.; Robledo, S.M.; Harmsen, M.C.; Echeverria, F. Improved corrosion resistance of commercially pure magnesium after its modification by plasma electrolytic oxidation with organic additives. *J. Biomater. Appl.* **2018**, *33*, 725–740. [CrossRef] [PubMed]
7. Matykina, E.; Garcia, I.; Arrabal, R.; Mohedano, M.; Mingo, B.; Sancho, J.; Merino, M.; Pardo, A. Role of PEO coatings in long-term biodegradation of a Mg alloy. *Appl. Surf. Sci.* **2016**, *389*, 810–823. [CrossRef]
8. Lu, J.; He, X.; Li, H.; Song, R. Microstructure and Corrosion Resistance of PEO Coatings Formed on KBM10 Mg Alloy Pretreated with $Nd(NO_3)_3$. *Materials* **2018**, *11*, 1062. [CrossRef]
9. Li, L.; Gao, J.; Wang, Y.; Srinivasan, P.B.; Liang, J.; Blawert, C.; Störmer, M.; Dietzel, W.; Asoh, H.; Ono, S.; et al. Effect of current density on the microstructure and corrosion behaviour of plasma electrolytic oxidation treated AM50 magnesium alloy. *Surf. Coat Technol.* **2015**, *272*, 182–189. [CrossRef]
10. Hussein, R.; Northwood, D.; Nie, X. The effect of processing parameters and substrate composition on the corrosion resistance of plasma electrolytic oxidation (PEO) coated magnesium alloys. *Surf. Coat. Technol.* **2013**, *237*, 357–368. [CrossRef]
11. Ono, S.; Moronuki, S.; Mori, Y.; Koshi, A.; Liao, J.; Asoh, H. Effect of Electrolyte Concentration on the Structure and Corrosion Resistance of Anodic Films Formed on Magnesium through Plasma Electrolytic Oxidation. *Electrochim. Acta* **2017**, *240*, 415–423. [CrossRef]
12. Asoh, H.; Matsuoka, S.; Sayama, H.; Ono, S. Anodizing under sparking of AZ31B magnesium alloy in Na3PO4 solution. *J. Jpn. Inst. Light Met.* **2010**, *60*, 608–614. [CrossRef]
13. Kanter, B.; Vikman, A.; Brückner, T.; Schamel, M.; Gbureck, U.; Ignatius, A. Bone regeneration capacity of magnesium phosphate cements in a large animal model. *Acta Biomater.* **2018**, *69*, 352–361. [CrossRef] [PubMed]
14. Anawati; Asoh, H.; Ono, S. Enhanced uniformity of apatite coating on a PEO film formed on AZ31 Mg alloy by an alkali pretreatment. *Surf. Coatings Technol.* **2015**, *272*, 182–189. [CrossRef]
15. Han, Y.; Hong, S.H.; Xu, K. Structure and in vitro bioactivity of titania-based films by micro-arc oxidation. *Surf. Coatings Technol.* **2003**, *168*, 249–258. [CrossRef]
16. Gu, X.; Li, N.; Zhou, W.; Zheng, Y.; Zhao, X.; Cai, Q.; Ruan, L. Corrosion resistance and surface biocompatibility of a microarc oxidation coating on a Mg–Ca alloy. *Acta Biomater.* **2011**, *7*, 1880–1889. [CrossRef] [PubMed]
17. Kannan, M.B.; Mathan, B.K. Electrochemical deposition of calcium phosphates on magnesium and its alloys for improved biodegradation performance: A review. *Surf. Coat. Technol.* **2016**, *301*, 36–41. [CrossRef]
18. Gao, Y.; Yerokhin, A.; Matthews, A. Deposition and evaluation of duplex hydroxyapatite and plasma electrolytic oxidation coatings on magnesium. *Surf. Coat. Technol.* **2015**, *269*, 170–182. [CrossRef]
19. Srinivasan, P.B.; Liang, J.; Blawert, C.; Stormer, M.; Dietzel, W. Characterization of calcium containing plasma electrolytic oxidation coatings on AM50 magnesium alloy. *Appl. Surf. Sci.* **2010**, *256*, 4017–4022. [CrossRef]
20. Yang, J.; Lu, X.; Blawert, C.; Di, S.; Zheludkevich, M.L. Microstructure and corrosion behavior of Ca/P coatings prepared on magnesium by plasma electrolytic oxidation. *Surf. Coat. Technol.* **2017**, *319*, 359–369. [CrossRef]

21. Lederer, S.; Sankaran, S.; Smith, T.; Fürbeth, W. Formation of bioactive hydroxyapatite-containing titania coatings on CP-Ti 4+ alloy generated by plasma electrolytic oxidation. *Surf. Coat. Technol.* **2019**, *363*, 66–74. [CrossRef]
22. Adeleke, S.; Ramesh, S.; Bushroa, A.; Ching, Y.; Sopyan, I.; Maleque, M.; Krishnasamy, S.; Chandran, H.; Misran, H.; Sutharsini, U. The properties of hydroxyapatite ceramic coatings produced by plasma electrolytic oxidation. *Ceram. Int.* **2018**, *44*, 1802–1811. [CrossRef]
23. Anawati, A.; Asoh, H.; Ono, S. Effects of alloying element ca on the corrosion behavior and bioactivity of anodic films formed on AM60 mg alloys. *Materials* **2017**, *10*, 11. [CrossRef] [PubMed]
24. Anawati, A.; Asoh, H.; Ono, S. Degradation Behavior of Coatings Formed by the Plasma Electrolytic Oxidation Technique on AZ61 Magnesium Alloys Containing 0, 1 and 2 wt.% Ca. *Int. J. Technol.* **2018**, *9*, 622. [CrossRef]
25. Jun, J.H.; Park, B.K.; Kim, J.M.; Kim, K.T.; Jung, W.J. Effects of Ca Addition on Microstructure and Mechanical Properties of Mg-RE-Zn Casting Alloy. *Mater. Sci. Forum* **2009**, *488*, 107–110. [CrossRef]
26. Jang, Y.; Tan, Z.; Jurey, C.; Xu, Z.; Dong, Z.; Collins, B.; Yun, Y.; Sankar, J. Understanding corrosion behavior of Mg–Zn–Ca alloys from subcutaneous mouse model: Effect of Zn element concentration and plasma electrolytic oxidation. *Mater. Sci. Eng. C* **2015**, *48*, 28–40. [CrossRef] [PubMed]
27. Brady, M.P.; Fayek, M.; Leonard, D.N.; Meyer, H.M.; Thomson, J.K.; Anovitz, L.M.; Rother, G.; Song, G.L.; Davis, B. Tracer Film Growth Study of the Corrosion of Magnesium Alloys AZ31B and ZE10A in 0.01% NaCl Solution. *J. Electrochem. Soc.* **2017**, *164*, C367–C375. [CrossRef]
28. Channing, S. *Annual Book of ASTM Standards*; ASTM International: Conshohocken, PA, USA, 1991.
29. Müller, L.; Müller, F.A. Preparation of SBF with different HCO3-content and its influence on the composition of biomimetic apatites. *Acta Biomater.* **2006**, *2*, 181–189. [CrossRef]
30. Lu, X.; Leng, Y. Theoretical analysis of calcium phosphate precipitation in simulated body fluid. *Biomaterials* **2005**, *26*, 1097–1108. [CrossRef]
31. Pekguleryuz, M.; Kainer, K.; Kaya, A. *Fundamentals of Magnesium Alloy*; Woodhead Publishing Ltd.: Cambridge, UK, 2013.
32. Massalski, T.; Okamoto, H.; Subramanian, P.; Kacprzak, L. *Binary Alloy Phase Diagrams*, 2nd ed.; ASM: Materials Park, OH, USA, 1990.
33. Hosford, W.F. *Physical Metallurgy*, 2nd ed.; Taylor and Francis Group: Boca Raton, FL, UAS, 2010.
34. Lunder, O.; Nordien, J.; Nisancioglu, K. Corrosion Resistance of Cast Mg-Al Alloys. *Corros. Rev.* **1997**, *15*, 439–470. [CrossRef]

materials

MDPI

Article

Influence of Micro-Arc Oxidation Coatings on Stress Corrosion of AlMg6 Alloy

Lesław Kyzioł [1,*] and Aleksandr Komarov [2]

[1] Faculty of Marine Engineering, Gdynia Maritime University, 81-225 Gdynia, Poland
[2] Joint Institute of Mechanical Engineering of the National Academy of Sciences of Belarus, The State Scientific Institution, 220072 Minsk, Belarus; al_kom@tut.by
* Correspondence: leslawkyziol@gmail.com; Tel.: +48-694-476-390

Received: 16 December 2019; Accepted: 10 January 2020; Published: 12 January 2020

Abstract: This paper shows results of a study on the corrosion behavior of micro-arc oxidation (MAO) coatings sampled from the AlMg6 alloy. The alloy was simultaneously subjected to a corrosive environment and static tensile stress. For comparative purposes, the tests were run for both coated samples and samples without coatings. The research was conducted at a properly prepared stand; the samples were placed in a glass container filled with 3.5% NaCl aqueous solution and stretched. Two levels of tensile stress were accepted for the samples: $\sigma_1 = 0.8R_{0.2}$ $\sigma_2 = R_{0.2}$, and the tests were run for two time intervals: $t_1 = 480$ h and $t_2 = 1000$ h. Prolonged stress corrosion tests (lasting up to 1000 h) showed that the samples covered with ceramic coatings demonstrated significantly higher corrosion resistance than the samples without the coatings. Protective properties of the coating could be explained by its structure. Surface pores were insignificant, and their depth was very limited. The porosity level of the main coating layer was 1%. Such a structure of coating and its phase composition provided high protective properties.

Keywords: aluminum alloy AlMg6; Al_2O_3 coating; phase composition; corrosion; stress corrosion; micro-arc oxidation

1. Introduction

Al-Mg alloys combine good formability, rather high strength, corrosion resistance, and weldability. Therefore, such alloys are used in many structures exposed to weathering, and especially in shipbuilding and offshore structures. It should be noted that studies carried out on samples made of the AlMg6 alloy showed a good resistance to stress corrosion for this alloy, but one much lower than for alloy 5083 [1,2]. However, the strength of alloy 5083 containing 5% Mg is noticeably inferior to the strength of AlMg6 alloy.

Stress corrosion of materials manifests itself through the formation of cracks in the metal when exposed to corrosive environment and static tensile stress. The cracks appearing on the metal surface are perpendicular to the direction of tensile stress and can be of intercrystalline or mixed nature. Studies have shown that before the appearance of pronounced cracks, there is often an incubation period. The intensity of microcracks can be determined on the basis of changes in mechanical properties after time intervals of the stress corrosion test [1–6].

Studies have also shown that Al-Mg alloys with a content of Mg ≤ 3, 5% exhibit a low susceptibility to stress corrosion. This is due to the discontinuity of β-phase molecules at the grain boundaries, which in turn results from the low supersaturation of the solid solution [7–10].

Al-Mg alloys with a content of Mg ≥ 3, 5%, especially above 5% (AlMg5, AlMg6), with a certain state of the structure and under specific external conditions may be resistant to intercrystalline, layer, and stress corrosion [3–5]. The study has shown that Al−Mg alloys with a content of more than 6 wt. % of Mg can be obtained, and they show good weldability and high mechanical properties [1,9–11]. An

increase in the Mg content results in an increase in strength, but leads to higher susceptibility to local corrosion and reduced resistance to corrosion under stress [12]. It is assumed that the grain boundaries are a favorable place for β-phase formation due to their low diffusion barrier (presence of defects such as dislocations and vacancies) [13]. In many cases, overexposure of Al–Mg sheets or other products to a temperature range of 70 °C to 200 °C may impede production, causing precipitation of the β-phase rich in Mg at the grain boundaries. These alloys are susceptible to intercrystalline, stress, or pitting corrosion, because the β-phase is electrochemically more active than the aluminum matrix [14–18].

Structures with a high Mg content resistant to corrosion are obtained through the use of complex manufacturing methods [4]. The goal of the research was to determine the impact of the protective ceramic coating on the corrosion resistance of the tested alloy. Micro-arc oxidation (MAO) is a very promising process in making tight coatings and curing of metal elements. This is a coating technique capable of forming ceramic coatings on metals such as Al, Mg, Ti, and their alloys [17–22]. This environmental friendly technique allows ceramic layers to be grown, giving the pieces high level mechanical and tribological properties and good corrosion protection in a single step of processing [23–26]. A number of studies have shown that the coatings obtained by micro-arc oxidation are an effective means of protecting aluminum alloys from corrosion [27–33]. The corrosion properties of the MAO coating of the BS 6082 Al alloy were tested against different immersion periods in a 0.5M NaCl solution for up to 48 h [28]. The research has shown the importance of sealing the pores in MAO coatings with the use of the sol–gel technique, enhancing the short-term corrosion resistance in 0.6M NaCl solution. The above investigation also revealed that the MAO coatings improved the corrosion resistance of the Al alloy because of the lack of defects in coatings [29].

Despite numerous studies on the protective properties of coatings, their effectiveness in protecting aluminum–magnesium alloys from stress corrosion has not been scrutinized. The major objective of the present study is to evaluate the overall effectiveness of MAO coatings in terms of resistance to aqueous stress corrosion. Regarding the above objective, MAO coatings were deposited on a AlMg6 alloy and their corrosion behavior was evaluated in 3.5% NaCl solution. In the available literature, there are only a few sources referring to the importance of protective coatings for stress corrosion [34,35]. These tests are very important because often the material is subject simultaneously to corrosive environments and stresses. In this paper the stress corrosion resistance has been evaluated using a change of mechanical properties of samples with coatings and without coatings.

2. Materials and Methods

Samples of AlMg6 alloy without coating and coated with a ceramic coating by MAO were subjected to stress corrosion. The tests were carried out on identical samples without coatings and with coatings to determine the effectiveness of the ceramic coating that protects the material against stress corrosion.

Samples for the static tensile test and the stress corrosion were made from a sheet with a thickness of g = 3 mm. The samples were cut down in a direction transverse to the rolling direction. The chemical composition and parameters of heat treatment of the AlMg6 alloy plates are presented in Table 1. The shape and dimensions of the samples for the determination of mechanical and stress corrosion properties are shown in Figure 1.

Table 1. Chemical composition and heat treatment parameters of the AlMg6 alloy sheet.

Material	Sheet Thickness, mm	Parameters of Production Technology	Chemical Composition, %							
			Mg	Mn	Ti	Zn	Si	Fe	Cu	Al
AlMg6	6	annealing at temp. 319 °C/10 h	6.15	0.61	0.05	0.05	0.16	0.27	0.05	rest

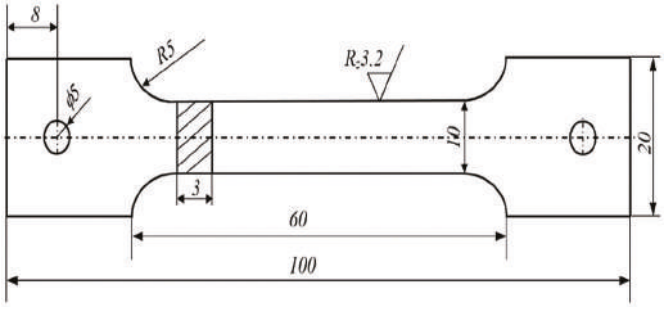

Figure 1. The shape and dimensions of samples for static and stress corrosion tests of the AlMg6 alloy.

The samples were polished with abrasive paper 600# and degreased with acetone followed by rinsing with distilled water before coating formation. The electrolyte was an aqueous solution of 2 g/L KOH and 5 g/L Na_2SiO_3. The electrolyte was agitated with compressed air. A forty litter bath from stainless steel was used. The specimen was served as the anode and the bath wall was served as the contrary electrode. The system was cooled by cold water pumped through double walls of the bath. The electrolyte temperature was controlled at 25−30 °C throughout the process. The MAO treatment was carried out using a pulsed AC power source. The current density, voltage, frequency, duty cycle, and duration time were 25A/dm^2, 280 V, 50 Hz, 50% and 60 min, respectively. After the treatment, the samples were rinsed in distilled water and dried in air.

Then, using abrasive paper 600#, the upper loose porous layer of about 20 μm thickness was removed from the surface of the samples, after which the samples were washed in distilled water with an ultrasonic bath SONOREX for 15 min and dried in air. The thickness of the coating on the samples prepared for testing was 150 ± 5 μm. The surface morphologies and cross-section morphologies of the coatings were examined with an optical microscope Axiovert 25 as well as with a scanning electron microscope (ZEISS, Jena, Germany). X−ray diffraction studies were carried out on a DRON−3M X−ray diffractometer (S. Petersburg, Russia) in scanning mode in 0.1 increments using Cu−Kα radiation in the Bragg–Brentano mode. The time of a set of pulses at a point was 15 s.

Stress corrosion tests of the AlMg6 alloy were carried out on samples for σ = const. The samples were placed in a glass container filled with 3.5% NaCl aqueous solution and stretched. Samples with and without coatings were subjected to stress corrosion tests for two levels of stress:

1—$\sigma_1 = 0.8R_{0.2}$, 2—$\sigma_2 = 1.0R_{0.2}$, where $R_{0.2}$ is the average value of the experimentally determined yield strength of samples without coating and with coating equal to 212 MPa and 217 MPa, respectively.

The corrosion tests were conducted for two time intervals: 1—480 h, 2—1000 h. Figure 2 presents a stand for testing stress corrosion resistance.

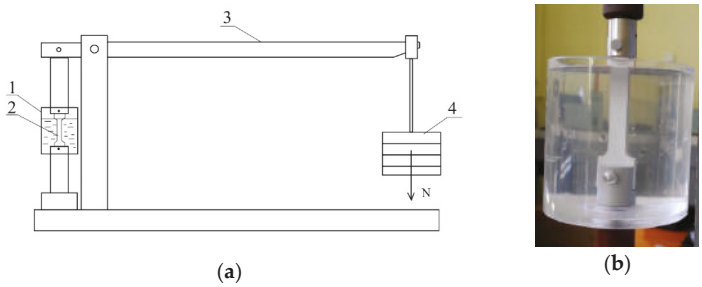

(**a**) (**b**)

Figure 2. Stand for testing the stress corrosion resistance of AlMg6 alloy, (**a**) test bench scheme for σ = const., 1—container filled with 3.5% of NaCl, 2—sample, 3—lever arm, 4—load, (**b**) container filled with 3.5% of NaCl in which the sample is located.

After stress corrosion tests the samples were subjected to a static tensile test to determine the mechanical changes of the AlMg6 test material. A static tensile test on samples without coatings and with coatings was carried out on a ZwickRoell testing machine (Ulm, Germany). The research was carried out at the Faculty of Mechanical Engineering of the Gdańsk University of Technology (Gdańsk, Poland).

3. Research Results and Their Analysis

Figure 3 presents images of samples for mechanical and stress corrosion tests without coating and coated. The formed coating has a light gray color and a uniform surface. The study of the surface morphology of the samples showed that the surface layer of the coating is characterized by the presence of pores up to 10 microns in size (Figure 4). Such a structure is typical for coatings obtained with the use of the micro-arc oxidation method, in which there is an upper loose porous layer and a dense, low porosity basic coating layer [5,6].

(**a**) (**b**)

Figure 3. Images of samples for stress corrosion tests of AlMg6 alloy with sheet thickness g = 6 mm, (**a**) without coating, (**b**) with coating.

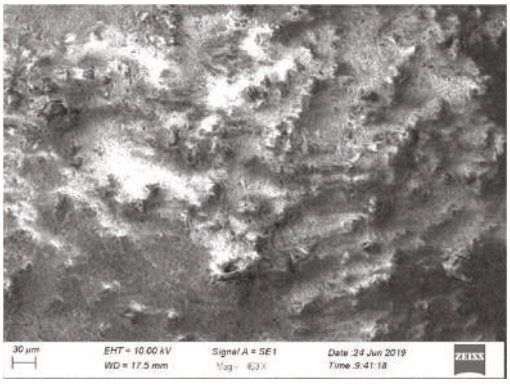

Figure 4. SEM image of the coating surface prior to testing.

Figure 5 presents images of samples without coating and coated after mechanical and stress corrosion tests. On samples without coatings, there are visible deposits and small corrosion centers (Figure 5a). There is no evidence of corrosion on samples with coating (Figure 5b). Studies performed on the cross-section of the coating after corrosion tests also showed no signs of corrosion (Figure 6).

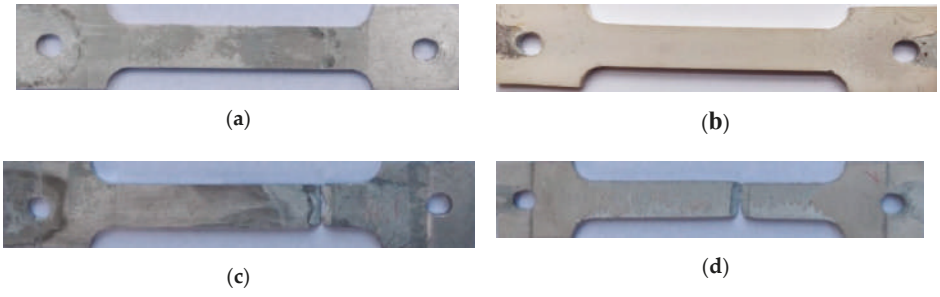

(**a**) (**b**)

(**c**) (**d**)

Figure 5. Images of samples after stress corrosion tests of AlMg6 alloy with sheet thickness g = 6 mm, (**a**) without coating, (**b**) with coating, (**c**) without cover after breaking, (**d**) with a coating after breaking.

High protective properties of the coating can be explained by its structure. As follows from the Figure 6, the pores on the surface of the coating have an insignificant size and depth and are limited to a loose surface layer. The main coating layer has a very low porosity (less than 1%), while the permeable porosity is absent. Such coating structures, as well as its phase composition, represented by chemically resistant aluminum oxide in the $\gamma-Al_2O_3$ and $\alpha-Al_2O_3$ modifications (Figure 7), provide high protective properties.

On the contrary, the surface of uncoated specimens of AlMg6 alloy was subjected to intense corrosion, as evidenced by the sources of material etching and corrosion products (Figure 5a,c).

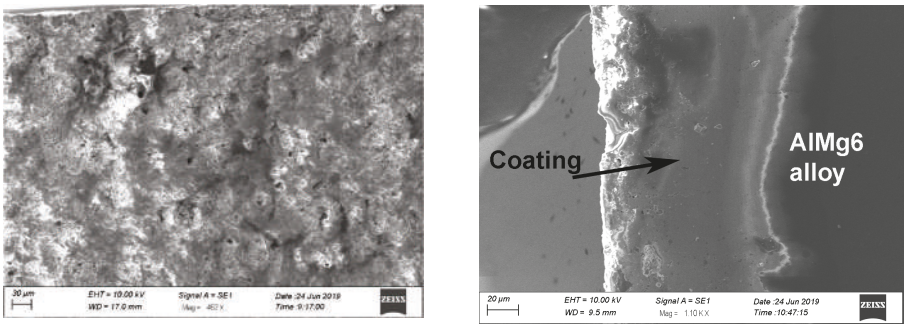

(**a**) (**b**)

Figure 6. SEM image of the surface (**a**) and cross-section (**b**) of the sample with coating after stress corrosion tests.

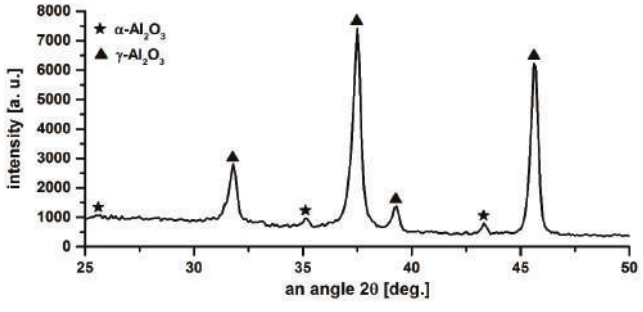

Figure 7. A fragment of the X−ray diffraction pattern of coating on a sample for the stress corrosion test.

Table 2 shows results of the test for static tensile stress of the AlMg6 alloy without coatings and with coatings. The obtained results indicate identical mechanical properties of the tested materials. A very thin layer of ceramics (about 150 μm), in relation to the thickness of the sample (g_s = 3 mm) has no influence on the mechanical properties of the tested materials.

Table 2. Mechanical properties of AlMg6 alloy samples without coatings and with coatings.

State of the Samples.	Yield Strength $R_{0.2}$	Tensile Strength R_m	Relative Elongation A_5
	MPa	MPa	%
without coatings	211	373	13.25
	215	372	13.45
	210	371	13.20
average	212	372	13.30
with coatings	215	369	13.65
	218	371	13.45
	218	370	13.40
average	217	370	13.50

The stress corrosion test is very rigorous because the material is simultaneously subject to a corrosive environment and stress. None of the 24 samples tested broke. The results of the tensile test of samples after exposure to stress corrosion for two time intervals and two stress levels are presented in Tables 3 and 4.

Table 3 shows results of the test for static tensile stress in samples with and without coatings at t = 480 h exposed to stress corrosion at the level of $\sigma = 0.8R_{0.2}$ and $\sigma = R_{0.2}$.

The results of the tests showed that for the level of stress $\sigma = 0.8R_{0.2}$:

- The samples without coating exhibited a decline of $R_{0.2}$ by 15%, R_m by 6%, and A_5 by over 20%;
- The samples with coating did not exhibit any deterioration of mechanical properties. The protective coating served its purpose well, protecting the material against corrosion.

For the level of stress $\sigma = R_{0.2}$:

- The samples without coating exhibited a decline of $R_{0.2}$ by 20%, R_m by 8%, and A_5 by over 36%;
- The samples with coating exhibited an insignificant decline of $R_{0.2}$ by 5%, no change, and A_5 by 7%.

For such a high level of stress the samples without coating exhibited a significant decline in mechanical properties caused by simultaneous exposure to stress and a corrosive environment.

In the case of the coated samples, there was an insignificant decline in mechanical properties caused by the high level of stress. The coating very tightly protected the sample surface, and thus the material of the sample was not subjected to corrosive environment.

Table 3. Mechanical properties of samples with and without coatings of AlMg6 alloy after exposure to stress corrosion at time t = 480 h.

State of the Samples	Stress Level	$R_{0.2}$	R_m	A_5
		MPa	**MPa**	**%**
Without coatings	$\sigma = 0.8R_{0.2}$	185	352	10.25
		182	351	10.32
		178	347	10.33
Average		180	350	10.30
With coatings		212	365	12.85
		209	374	13.18
		209	371	12.97
Average		210	370	13.00
Without coatings	$\sigma = 1.0R_{0.2}$	167	338	8.45
		171	343	8.65
		172	339	8.40
Average		170	340	8.50
With coatings		208	368	12.40
		210	361	12.65
		206	366	12.45
Average		208	365	12.50

Table 4 shows the results of the samples exposed to stress corrosion at similar levels of stress, i.e., $\sigma = 0.8R_{0.2}$ and $\sigma = R_{0.2}$ after the time of t = 1000 h.

For the level of stress $\sigma = 0.8R_{0.2}$:

- the samples without coating exhibited a decline of $R_{0.2}$ by 25%, R_m by 18%, and A_5 by over 50%;
- the samples with coatings exhibited a decline of $R_{0.2}$ by 3%, R_m by 6%, and A_5 by 14%.

With the amount of stress corrosion time, a further decline in the mechanical properties of uncoated AlMg6 alloy was observed.

The coated samples showed an insignificant decline in mechanical properties. The decline was not caused by the corrosive environment, but rather by crawling of the material, which was subjected to a high level of stress.

For the level of stress $\sigma = R_{0.2}$:

- The samples without coating exhibited a decline of $R_{0.2}$ by over 30%, R_m by 23%, and A_5 by nearly 60%;
- The samples with coatings exhibited a decline of $R_{0.2}$ by 4%, R_m by 8%, and A_5 by 18%.

For such a high level of stress and a long exposure to a corrosive environment, a further decline in mechanical properties was observed in the samples with no protective coatings. The decline occurred due to a simultaneous concurrence of high stress and corrosion caused by the 3.5% NaCl solution.

Having been exposed to a corrosive environment for t = 1000 h and highly stressed for up to $\sigma = R_{0.2}$, the coated samples sustained an insignificant decrease in mechanical properties. The limited decline is caused by the high level of stress.

Table 4. Mechanical properties of samples with and without coatings of AlMg6 alloy after exposure to stress corrosion at time t = 1000 h.

State of the Samples	Stress Level	$R_{0.2}$	R_m	A_5
		MPa	**MPa**	**%**
Without coatings	$\sigma = 0.8R_{0.2}$	155	303	6.48
		162	307	6.54
		163	305	6.48
Average		160	305	6.50
With coatings		213	354	11.62
		209	342	11.48
		208	348	11.40
Average		210	348	11.50
Without coatings	$\sigma = 1.0R_{0.2}$	140	288	5.48
		148	280	5.53
		147	287	5.55
average		145	285	5.52
With coatings		208	341	10.98
		205	336	11.12
		202	341	10.90
Average		205	340	11.00

Figures 8–10 shows the influence of corrosive environment and stress level on the reduction of mechanical properties of AlMg6 alloy samples with and without a ceramic coating. The research shows that there was almost a 30% reduction in yield strength and tensile strength, and nearly a 60% reduction in the plasticity of AlMg6 alloy samples without a ceramic coating for stress level $\sigma = R_{0.2}$ and corrosion exposure time t = 1000 h. For identical corrosion conditions and stress levels, there was a 4% decrease in yield strength and tensile strength as well as a 8% decrease in plasticity of AlMg6 alloy samples coated with ceramic coating.

The samples of AlMg6 alloy without coatings showed a concurrence of static tensile stress and corrosive environment. This kind of corrosion−stress synergy is the very reason for the accelerated degradation of the material. However, the samples with ceramic coatings showed a high resistance to simultaneous corrosion and stress factors as the coatings protected the material against corrosion. An insignificant decrease in mechanical properties occurred due to the high level of stress. Figures 8–10 shows a very narrow area of the decline in mechanical samples of coated AlMg6 alloys.

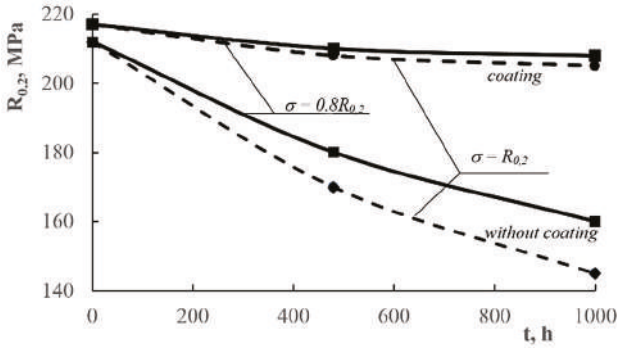

Figure 8. Influence of the corrosive environment and stress level on the yield strength reduction of AlMg6 alloy samples without coatings and with coatings.

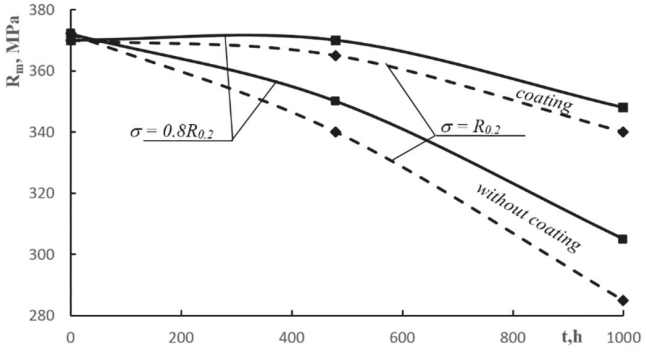

Figure 9. Influence of the corrosive environment and stress level on the tensile strength reduction of AlMg6 alloy samples without coatings and with coatings.

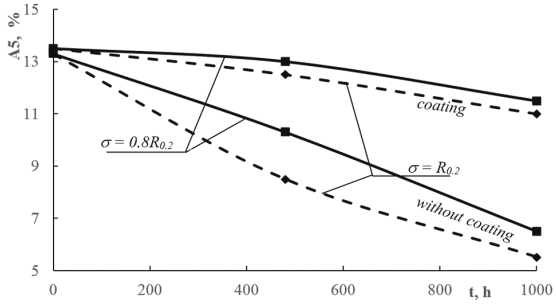

Figure 10. Influence of the corrosive environment and stress level on the relative elongation reduction of AlMg6 alloy samples without coatings and with coatings.

4. Summary

Studies have been carried out to evaluate the protective properties of the coating obtained by micro-arc oxidation on aluminum alloy AlMg6 from stress corrosion. The protective properties of the coating were evaluated by changing the mechanical characteristics (yield strength $R_{0.2}$, tensile strength R_m and relative elongation A_5) after holding the samples without coating and coated in a 3.5% NaCl solution under a stress of $\sigma_1 = 0.8R_{0.2}$ and $\sigma_2 = R_{0.2}$ for 480 h and 1000 h. The results have showed that the MAO coating provides a fairly effective protection of the aluminum alloy from stress corrosion if the

selected test conditions are met. No corrosive centers were observed on samples with a ceramic coating, but small corrosion centers may be observed on samples without a coating. The effect of corrosion led to a decrease in the mechanical characteristics of the uncoated samples. So, after the 480-hour experiment at both stress levels, there was no noticeable decrease in the mechanical characteristics of coated samples, while the mechanical characteristics of uncoated samples decreased 1.1 (R_m) to 1.5 (A_5) times. After holding the samples for 1000 h, a more noticeable difference in mechanical characteristics was observed. In this case, the decrease in the characteristics of coated samples did not exceed 1.07 times (R_m) to 1.12 times (A_5), while the decrease in the properties of uncoated samples reached 1.3 (R_m) to 2.4 times (A_5). The high protective properties of the coating can be explained by the chemical inertness of its composition ($\gamma-Al_2O_3$ and $\alpha-Al_2O_3$) and low porosity (less than 1%) in the absence of through porosity.

Author Contributions: Conceptualization, L.K. and A.K.; methodology, L.K. and A.K.; formal analysis, L.K. and A.K.; investigation, L.K. and A.K.; resources, L.K and A.K.; data curation, L.K. and A.K.; writing—original draft preparation, L.K. and A.K.; writing—review and editing, L.K. and A.K.; visualization, L.K and A.K.; supervision, L.K. and A.K.; funding acquisition, L.K. All authors have read and agreed to the published version of the manuscript.

Funding: This research received no external funding.

Conflicts of Interest: The authors declare no conflict of interest.

References

1. Kyzioł, L. Wpływ obróbki cieplnej na odporność na korozje naprężeniową i wytrzymałość zmęczeniowo−korozyjną stopów AlMg6 i AlZn5Mg2CrZr przeznaczonych na kadłuby okrętów. Ph.D. Thesis, Akademia Marynarki Wojennej, Gdynia, Poland, August 1990.
2. Kyzioł, L.; Zganiacz, F. Wstępne badania korozji naprężeniowej stopów AlMg6 i AlMg4.5Mn. *Zeszyty Naukowe AMW, Gdynia* **1988**, *2*, 85–104.
3. Cudny, K.; Jasiński, R.; Kyzioł, L. Badanie stopów AlMg6 i AlZn5Mg2CrZr w celu ich zastosowania w budownictwie okrętowym. *Budownictwo Okrętowe i Gospodarka Morska, Gdańsk* **1991**, *9*, 10–14.
4. Sinavskij, V.S.; Volov, V.D.; Kalinin, V.D. *Korrozja i zaŝĉita aluminievych splavov*; Izdatielstvo Metallurgija: Moskva, Russia, 1986.
5. Jones, R.H.; Vetrano, J.S.; Windisch, C., Jr. Stress corrosion cracking of Al-Mg and Mg-Al alloys. *Corrosion* **2004**, *60*, 1144–1154. [CrossRef]
6. Torkan, A.; Rabiei, B.A.; Khakpour, I. Corrosion Behavior of AA5038 Nanostructured Aluminum Alloy Produced by Accumulative Roll-Bonding. *Nanosci. Nanometr.* **2018**, *4*, 34–40. [CrossRef]
7. Gao, J.; David, J.Q. Enhancement of the Stress Corrosion Sensitivity of AA5083 by Heat Treatment. *Metall. Mater. Trans. A* **2011**, *42A*, 356–364. [CrossRef]
8. Goswami, G.; Spanos, P.S.; Paoa, R.; Holtz, L. Precipitation behavior of the phase in Al-5083. *Mater. Sci. Eng.* **2010**, *527*, 1089–1095. [CrossRef]
9. Choi, D.-H.; Ahn, B.-W.; Quesnel, D.J.; Seung, B.J. Behavior of β-phase (Al_3Mg_2) in AA 5083 during friction stir welding. *Intermetallics* **2013**, *35*, 120–127. [CrossRef]
10. Radović, L.; Bučko, M.; Miladinov, M. Corrosion Behavior of TIG Welded AlMg6Mn Alloy. *Sci. Tech. Rev.* **2016**, *66*, 10–17. [CrossRef]
11. Romhanji, E.; Popović, M.; Radmilović, V. Room temperature deformation behaviour of AlMg6.5 alloy sheet. *Z. Metallkunde* **1999**, *90*, 305–310.
12. Timoshenko, Y.B. On the relation between the Luders deformation and grain boundary structure in aluminium alloy. *Revue Phys. Appl.* **1990**, *25*, 1001–1004. [CrossRef]
13. Radović, L.J.; Nikačević, M.; Jordović, B. Deformation behaviour and microstructure evolution of AlMg6Mn alloy during shear spinning. *Trans. Nonferrous Met. Soc. China* **2012**, *22*, 991–1000. [CrossRef]
14. Radović, L.J.; Nikačević, M. Microstructure and properties of cold rolled and annealed Al-Mg alloys. *Sci. Tech. Rev.* **2008**, *58*, 14–20.
15. Zhu, Y. Characterization of Beta Phase Growth and Experimental Validation of Long Term Thermal Exposure Sensitization of AA5xxx Alloys. Master's Thesis, The University of Utah, Salt Lake City, UT, USA, 2013.

16. Jones, R.H.; Baer, D.R.; Danielson, M.J.; Vetrano, J.S. Role of Mg in the Stress Corrosion Cracking of an Al-Mg Alloy. *Metall. Mater. Trans. A* **2001**, *32A*, 1699–1711. [CrossRef]
17. Yerokhin, A.L.; Voevodin, A.A.; Lyubimov, V.V.; Zabinski, J.; Donley, M. Plasma Electrolytic Fabrication of Oxide Ceramic Surface Layers for Tribotechnical Purposes on Aluminium Alloys. *Surf. Coat. Technol.* **1998**, *110*, 140–146. [CrossRef]
18. Vityaz', P.A.; Komarov, A.I.; Komarova, V.I. Triboengineering properties of ceramic oxide coatings under boundary friction against steel. *J Frict. Wear.* **2008**, *29*, 325–329. [CrossRef]
19. Nie, X.; Leyland, A.; Song, H.W.; Yerokhin, A.L.; Dowey, S.J.; Matthews, A. Thickness Effects on the Mechanical Properties of Micro-arc Discharge Oxide Coatings on Aluminium alloys. *Surf. Coat. Technol.* **1999**, *116–119*, 1055–1060. [CrossRef]
20. Gnedenkov, S.V.; Khrisanfova, O.A.; Zavidnaya, A.G.; Sinebrukhov, S.L.; Kovryanov, A.N.; Scorobogatova, T.M.; Gordienko, P.S. Production of Hard and Heat-Resistant Coatings on Aluminium Using a Plasma Micro-discharge. *Surf. Coat. Technol.* **2000**, *123*, 24–28. [CrossRef]
21. Wang, Y.K.; Sheng, L.; Xiong, R.Z.; Li, B.S. Study of Ceramic Coatings Formed by Microarc Oxidation on Al Matrix Composite Surface. *Surf. Eng.* **1999**, *15*, 112–114. [CrossRef]
22. Butyagin, P.I.; Khokhryakov, Y.V.; Mamaev, A.I. Microplasma Systems for Creating Coatings on Aluminium Alloys. *Mater. Lett.* **2003**, *57*, 1748–1751. [CrossRef]
23. Zhang, Y.; Yan, C.; Wang, F.; Lou, H.; Cao, C. Study on the Environmentally Friendly Anodizing of AZ91D Magnesium Alloy. *Surf. Coat. Technol.* **2002**, *161*, 36–43. [CrossRef]
24. Rama Krishna, L.; Somaraju, K.R.C.; Sundararajan, G. The Tribological Performance of Ultra-hard Ceramic Composite Coatings Obtained Through Microarc Oxidation. *Surf. Coat. Technol.* **2003**, *163–164*, 484–490. [CrossRef]
25. Voevodin, A.A.; Yerokhin, A.L.; Lyubimov, V.V.; Donley, M.S.; Zabinski, J.S. Characterization of Wear Protective Al-Si-O Coatings Formed on Al-based Alloys by Micro-arc Discharge Treatment. *Surf. Coat. Technol.* **1996**, *86–87*, 516–521. [CrossRef]
26. Tian, J.; Luo, Z.; Qi, S.; Sun, X. Structure and Antiwear Behavior of Micro-arc Oxidized Coatings on Aluminum Alloy. *Surf. Coat. Technol.* **2002**, *154*, 1–7. [CrossRef]
27. Kuhn, A.T. Plasma anodized aluminum-A 2000/2000 Ceramic Coating. *Met. Fnish.* **2002**, *100*, 44. [CrossRef]
28. Nie, X.; Meletis, E.I.; Jiang, J.C.; Leyland, A.; Yerokhin, A.L.; Matthews, A. Abrasive Wear/Corrosion Properties and TEM Analysis of Al_2O_3 Coatings Fabricated Using Plasma Electrolysis. *Surf. Coat. Technol.* **2002**, *149*, 245–251. [CrossRef]
29. Barik, R.C.; Wharton, J.A.; Wood, R.J.K.; Stokes, K.R.; Jones, R.L. Corrosion, Erosion and Erosion-Corrosion Performance of Plasma Electrolytic Oxidation (PEO) Deposited Al_2O_3 Coatings. *Surf. Coat. Technol.* **2005**, *199*, 158–167. [CrossRef]
30. Nitin Wasekar, P.; Jyothirmayi, A.; Rama Krishna, L.; Sundararajan, G. Effect of Micro Arc Oxidation Coatings on Corrosion Resistance of 6061-Al Alloy 2008. *J. Mater. Eng. Perform.* **2008**, *17*, 708–713. [CrossRef]
31. Sundararajan, G.; Rama Krishna, L. Mechanisms Underlying the Formation of Thick Alumina Coatings Through the MAO Coating Technology. *Surf. Coat. Technol.* **2003**, *167*, 269–277. [CrossRef]
32. Guangliang, Y.; Xianyi, L.; Yizhen, B.; Haifeng, C.; Zengsun, J. The Effects of Current Density on the Phase Composition and Microstructure Properties of Micro-arc Oxidation Coating. *J. Alloy Compd.* **2002**, *345*, 196–200. [CrossRef]
33. Sobolev, A.; Kossenko, A.; Zinigrad, M.; Borodianskiy, K. Comparison of plasma electrolytic oxidation coatings on Al alloy created in aqueous solution and molten salt electrolytes. *Surf. Coat. Technol.* **2018**, *344*, 590–595. [CrossRef]
34. Hua, S.; Song, R.G.; Zong, Y.; Cai, S.W.; Wang, C. Effect of solution pH on stress corrosion and electrochemical behavior of aluminum alloy with micro-arc oxidation coating. *Mater. Res. Express* **2019**, *6*, 096441. [CrossRef]
35. Lianxi, C.; Yinying, S.; Hanyu, Z.; Zhibin, L.; Xiaojian, W.; Wei, L. Influence of a MAO + PLGA coating on biocorrosion and stress corrosion cracking behavior of a magnesium alloy in a physiological environment. *Corros. Sci.* **2019**, *148*, 134–143.

materials

MDPI

Article

Enhanced Erosion–Corrosion Resistance of Tungsten by Carburizing Using Spark Plasma Sintering Technique

Yan Jiang [1], Junfeng Yang [2,*], Zhuoming Xie [2] and Qianfeng Fang [2,*]

[1] International Institute of Vanadium and Titanium, Panzhihua University, Panzhihua 617000, China; jiangyanzky@163.com

[2] Key Laboratory of Materials Physics, Institute of Solid State Physics, Chinese Academy of Sciences, Hefei 230031, China; zmxie@issp.ac.cn

* Correspondence: jfyang@issp.ac.cn (J.Y.); qffang@issp.ac.cn (Q.F.)

Received: 11 May 2020; Accepted: 12 June 2020; Published: 15 June 2020

Abstract: The biggest obstacle for the application of tungsten as the target materials in the spallation neutron source is its serious corrosion in the coolant of flowing water. For this reason, W–Cr–C clad tungsten was developed by tungsten carburizing in a spark plasma sintering device, with superior corrosion resistance in the static immersion and electrochemical corrosion test. This work focused on its erosion and corrosion performance in a flowing water system, based upon test parameters simulated under the service conditions. W–Cr–C clad tungsten showed superior corrosion resistance to that of bare tungsten due to the corrosion form changing from the intergranular corrosion of bare tungsten to pitting corrosion of W–Cr–C coating. The corrosion rate of tungsten was as high as tenfold that of the coated sample at 20 °C, and at most fourfold at 60 °C after testing for 360 h. Effects of water velocity and temperature on pitting and intergranular corrosion were investigated in detail and their corresponding corrosion mechanisms were analyzed and discussed.

Keywords: tungsten; W–Cr–C coating; carburization; intergranular corrosion; pitting corrosion

1. Introduction

Tungsten is being chosen as the most favorable spallation target material for the spallation neutron source (SNS) due to its obvious advantages including high melting point, high neutron yield, and superior thermal conductivity [1,2]. However, on the issue of compatibility with flowing water coolant, tungsten has long been challenged because of its serious corrosion in water, especially in the case of flowing water where both erosion and corrosion occur simultaneously [3–6].

To improve the corrosion resistance, tungsten cladding with high temperature and corrosion resistance coatings have been developed as a target material such as HIPed tantalum-clad tungsten [7,8]. However, it suffers from issues of interface defects [7] and the high decay heat of tantalum [8,9]. Alternatively, coatings such as tungsten carbide and chromium carbide have been generally adopted to protect the substrate from corrosion under harsh environments in engineering and industrial fields [10–15]. In the conventional preparation of cemented carbides, cobalt as binder phase is commonly introduced to densify the particles, which is known as a poorly resistant element to corrosion [16]. However, the development of binder-free tungsten carbide coatings needed to solve two problems: density and brittleness. To this end, carburizing by spark plasma sintering (SPS) technology was employed to produce tungsten carbide coatings on tungsten [17]. SPS is a high-temperature and fast-process sintering technique that provides a fast heating/cooling rate, short consolidation time, and controllable pressure, having been widely used in densification fabrication of nanomaterials, gradient functional materials, and ceramic materials. By SPS, the carburized layer over 20 μm thick was

quickly achieved at 1600 °C, holding for 10 min with a pressure of 45 MPa [17], and a double thick layer was available when 20 min and 30 min were tried. On this basis, W–xCr–C (x = 0.5, 1, 2, 3, and 6 wt.%) composite layers with higher compactness and uniform grain size distribution were fabricated in the same way [18]. Electrochemical corrosion measurements on a WC clad tungsten system and W–Cr–C clad tungsten system indicated that the W–1%Cr–C clad tungsten sample performed well and exhibited the lowest corrosion current density [19].

As a result of these findings, W–1%Cr–C (W–Cr–C for short in the following text) clad tungsten by the SPS method was chosen as the potential material to undergo the following dynamic corrosion test in flowing water; flowing water (pH: 6~8) was adopted as the coolant in service condition to remove the heat in the target chamber. According to the simulation for the 100 kW neutron spallation source, a flow velocity of about 2 ms^{-1} is enough for the heat to be removed from the target, under which the highest target temperature is around 60 °C [2,20]. Therefore, this work investigated the corrosion performance of W–Cr–C clad tungsten at such conditions with the main purpose to explore and understand the behavior and mechanism in the erosion–corrosion process. Bare tungsten was taken into comparison.

2. Materials and Methods

A commercial grade tungsten disc (density: 18.48 g/cm^3, Zhuzhou Cemented Carbide Group Co. Ltd., Zhuzhou, China; the main elements included are listed in Table 1) with cylindrical form (Ø16 mm × 3 mm) was embedded in the mixed powder of graphite (99.95%, 8000 mesh, Aladdin) and 1 wt.% chromium (99.5%, ≥325 mesh, Aladdin, Shanghai, China), and then placed in a graphite mold and sintered in a SPS furnace (HPD 5, FCT Systeme GmbH, Rauenstein, Germany), as shown in Figure 1a. A target temperature of 1600 °C holding for 10 min with a pressure of 45 MPa was exploited on the graphite die (Ø20 mm). The diameter of the die could change from 10 mm to 100 mm according to the sample dimensions. Pressure was used to bring the powder and disc into full contact. The heating and cooling rates of SPS were both 100 °C/min. After sintering, the disc was taken out and cleaned ultrasonically in acetone. A scanning electron microscopy (SEM)(Sirion 200, FEI, Hillsboro, OR, USA) and electron backscatter diffraction (EBSD) detector (Aztec Nordlys Max3, Oxford Instruments, Oxford, UK, incorporated in the SEM device) was applied to characterize the surface morphology, phase composition, and distribution. The samples for the EBSD measurements were mechanically polished with W0.5 diamond paste and then electropolished in 2% NaOH solution. Phase identification was derived from the crystal structure database (HKL, ICSD, and NIST) installed on the EBSD system.

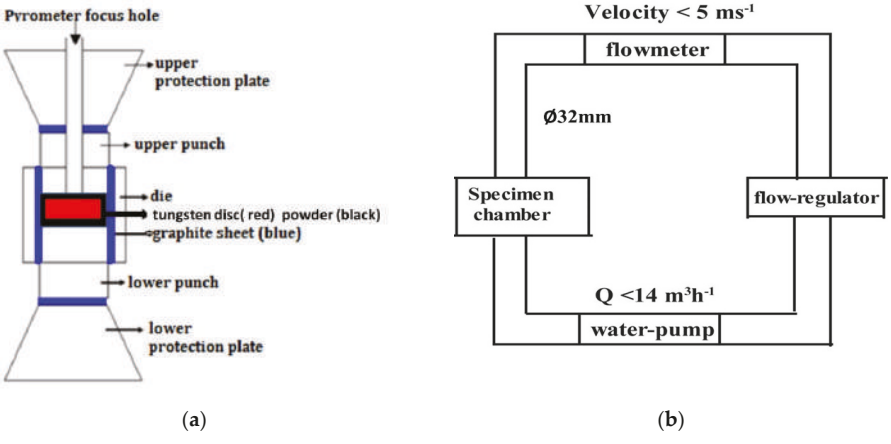

Figure 1. The schematic diagram of the sample placement in the spark plasma sintering setup (**a**) and the self-designed water flowing device (**b**).

The erosion–corrosion experiments were conducted in a home-made pipe flow circulating system as illustrated in Figure 1b. Diameter of all water passages was 32 mm. The water-pump was placed into an improved thermostatic water-container (0.6 × 0.6 × 1 m) where the water circulated. PH of the water was about 6~7. The oxygen content in the passages can be regarded as a saturation value since the water-container is a semi-open vessel. The tested samples were side by side fixed on the inner upper wall of the specimen chamber, leaving only one exposed surface (Ø16 mm) parallel to the flow direction.

Table 2 lists the test parameters with reference to the simulated service conditions. The flowing velocity and temperature was controlled by the flow regulator and the thermostatic bath, respectively. The error is also marked out at Table 2. The temperature value 20 °C was the entrance temperature of the flowing water. At the relative low temperature of 20 °C, a test at the largest velocity of 2 ms^{-1} was conducted, in light of the small difference in the corrosion behavior between 1 and 2 ms^{-1}. After the experiments, the corrosion performance was evaluated by analyzing the corrosion rate and the corroded morphology.

The weight was recorded every 12 h in the erosion–corrosion test, using a balance with an accuracy of 0.01 mg. The average corrosion rate ν ($g/cm^2 \cdot h$) was calculated from the following equation:

$$\nu = (m_0 - m_t)/s \cdot t \quad (1)$$

where m_0 is the original mass of specimen, m_t the mass of specimen after corrosion for t hours, s (cm^2) the exposure area before corrosion and t (h) the corrosion time. As the change in s after corrosion is very small, it is considered as a constant. It is worth pointing out in the gravimetric measurements that it was not easy to accurately clean up the corrosion deposits of the corroded specimens without damaging the matrix. Therefore, after the tests, the specimens were directly dried in a vacuum oven at 100 °C for 12 h without any surface treatment, and then their mass m_t was measured. If $\nu > 0$, it means a mass loss and removal of the corrosion products from the surface. According to the variation of the ν value, one can judge what happened to each specimen in the corrosion process. The corroded surface morphology was studied by means of SEM observations.

Table 1. The impurities with concentration over 0.001 wt.% in tungsten bulk.

Mo	Fe	Al	Si	P	C	N	O	W
0.009	0.001	0.001	0.001	0.001	0.001	0.001	0.0014	Bal

Table 2. The parameters set in the flowing water test.

Sample	Temperature (±3 °C)	Velocity (±0.1 ms^{-1})	Characterization
Tungsten and W–Cr–C coated tungsten	20 60	2 1, 1.5, 2	Corrosion rate and Morphology

3. Results

3.1. Morphology and Phases

Before corrosion measurement, the morphology, compositions, and phase distribution of the coated sample were characterized by the EBSD system. The fractured surface of the coatings showed good bonding with the substrate and high compact structures with a uniform thickness of around 25 μm (Figure 2a). The coating consisted of external W–Cr–C (hexagonal WC (ICSD [15406]) and $WC_{0.98}$ (ICSD [77738]) plus dispersed Cr_7C_3 (ICSD [52289]) (Figure 2b,c) and intermediate hexagonal W_2C (ICSD [77567]) (Figure 2e). Close to the carbon and chromium-rich zone, tungsten carbide reached stoichiometry WC (nonstoichiometric $WC_{0.98}$ is also commonly designated as WC) with an average grain size of 800 nm (Figure 2c,d), and chromium carbide is indexed as Cr_7C_3. Along the

diffusion path, the composition becomes the carbon-depleted W_2C and nearly no chromium carbides are detected in the intermediate layer due to the preferential diffusion of carbon. The W_2C phase accounts for more than 95 vol.% of the coating due to its much lower Gibbs free energy than WC at high temperature [21]. Furthermore, a small fraction of $WC_{0.98}$ precipitates were found in the W_2C grains (Figure 2e), which were derived from the partial solid-state decomposition of W_2C below 1250 °C [22]. The vast majority of the W_2C phase remained stable due to the fast cooling rate (100 °C /min). Figure 2f shows the pole figures and inverse pole figures with respect to the growth direction of the W_2C layer. Interestingly, the W_2C layer presented obvious crystallographic preferred orientations: the <001>//Y axis (the sintering pressure direction). Strong fiber texture <001> suggests the formation of a columnar structure of W_2C coating via spark plasma sintering.

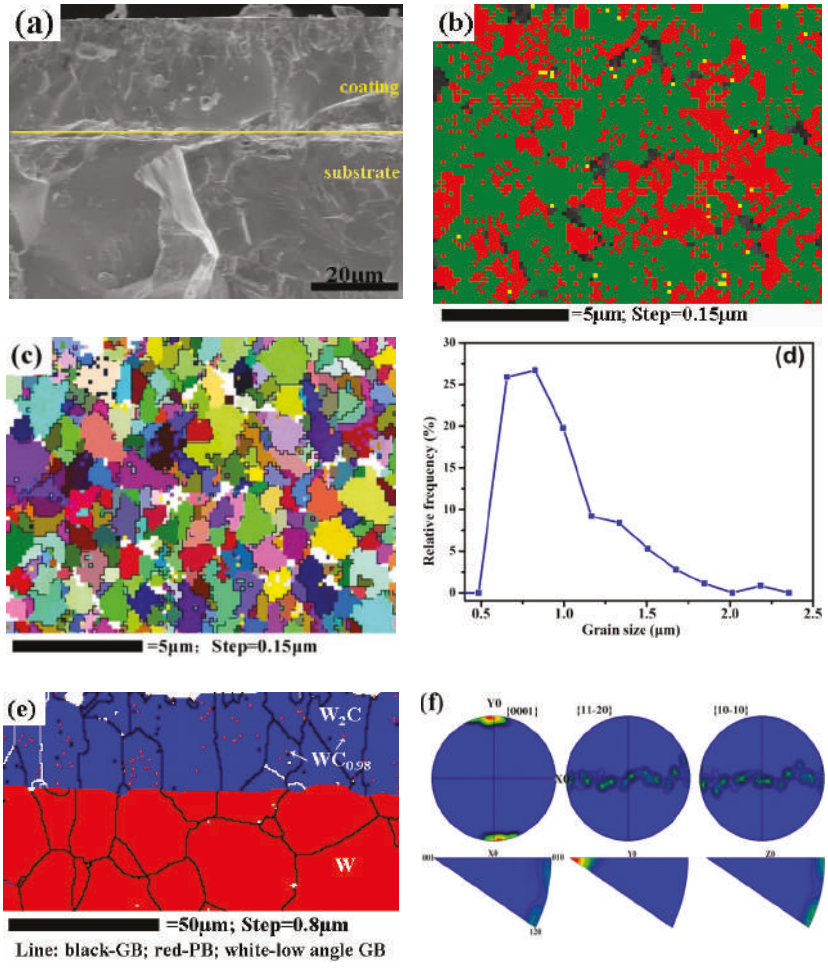

Figure 2. (**a**) Scanning electron microscopy (SEM) image of the cross-section of coating; (**b**) phase distribution of the coating surface (an indexing rate of about 91%, the black refers to the unindexed sites, the red to the WC phase, the green to $WC_{0.98}$, the yellow to Cr_7C_3); (**c**) Euler image and (**d**) grain size distribution of the WC and $WC_{0.98}$ phases; (**e**) phase distribution of the inner coating (the blue refers to the W_2C phase, the red to the W substrate, the pink dots are the $WC_{0.98}$ phases; GB: grain boundary; PB: phase boundary); (**f**) pore figure and inverse pore figure of the inner coating.

Such a gradient structure from base to bottom by carburizing through SPS technology could release thermal stress and avoid cracks in the coating. Other technology like HVOF (high velocity oxygen fuel) spray can also be applied in creating nano WC-based coatings made of powders [23]. The spray process acts like the high temperature sintering of the raw powders, and micro-cracks are caused by thermal stress in the spray process. More importantly, like other conventional preparations of a WC coating, the bonding phase of cobalt is commonly introduced to densify the WC, which is known as in-resistant element to corrosion.

3.2. Corrosion Rate

Under a water temperature of 20 °C, the corrosion rate as a function of time is shown in Figure 3. In general, the corrosion rate for tungsten clad with W–Cr–C decreased with increasing time and gradually went to a steady state after many fluctuations. The fluctuations imply that the accumulation and breakaway of the corrosion products occurred alternatively, namely coexistence of chemical and mechanically driven corrosion. The remarkable maximum corrosion rate belongs to bare tungsten, which was located uppermost over the entire time range and finally reached as high as tenfold that of the coated sample, which was relatively stable around the zero line.

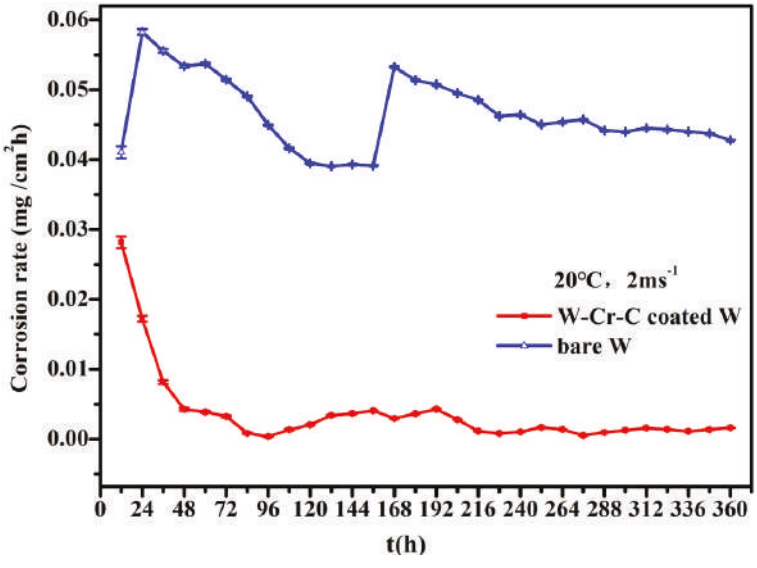

Figure 3. Variation of the corrosion rate with time for samples at the velocity of 2 ms^{-1} under the water temperature of 20 °C.

The corrosion rates under the water temperature of 60 °C are shown in Figure 4. The change in corrosion rate was positively related to the flow rate. When the flow velocity was 1 ms^{-1} and 1.5 ms^{-1}, the corrosion rate of the W–Cr–C coated W sample was less than 0.01 $mg{\cdot}cm^{-2}{\cdot}h^{-1}$. The corrosion rate of bare tungsten sample almost doubled and its fluctuation with time was larger. When the flow velocity increased to 2 ms^{-1}, the corrosion rates of all samples increased to higher values, varying in the range of 0.25–0.05 $mg{\cdot}cm^{-2}{\cdot}h^{-1}$ during the experiment time of 360 h.

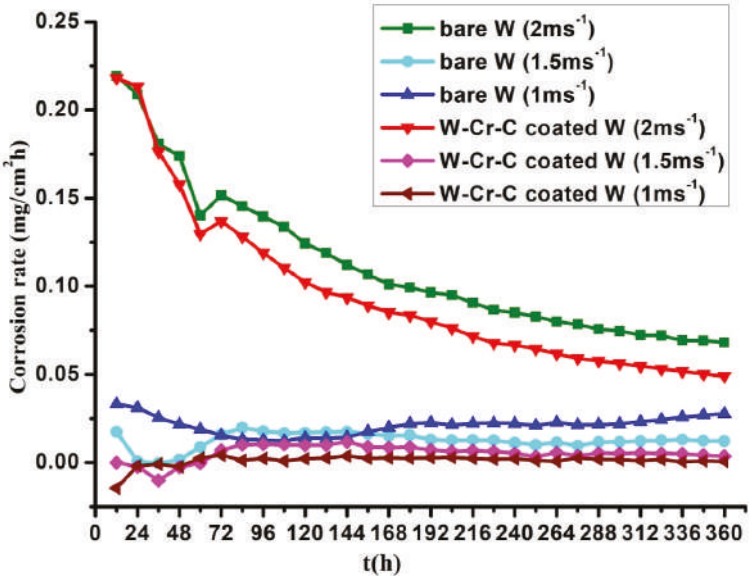

Figure 4. Variation of corrosion rate with time for samples at various flow velocities under the water temperature of 60 °C.

3.3. Corrosion Mechanism

The corroded appearances of tungsten clad with W–Cr–C are shown in Figure 5. The initial surface of the W–Cr–C coating (Figure 5a) presented deficiencies of small scattered pores left by SPS fabrication. After the 360 h test, the morphology changed slightly, but increased pores with increasing velocity or temperature, displaying a dominant feature of pitting corrosion (Figure 5b–e). Depth and the number of pores are difficult to quantify, so Figure 5f counts the area fraction of pores using image software (based upon the difference in primary contrast of images) by collecting six SEM graphs with the same magnification to describe the changes of pitting. Under the water temperature of 60 °C, the area fraction of the pores increased from the initial 0.4 ± 0.1% up to 4.5 ± 1% when the flow velocity varied from 0 to 2 ms^{-1}. However, there was no single linear or parabolic law between the pore area fraction and flow velocity for a remarkable rise at the flow velocity of 2 ms^{-1}. When the water temperature dropped to 20 °C, the reduction in pore area fraction reached 60%, almost close to the rate of temperature decline. Pitting area dependent upon velocity and temperature agreed well with the corrosion rate curves.

The corrosion behavior of bare tungsten was totally different, as shown in Figure 6. A rough metallographic structure with bimodal grain-size distribution appeared as a consequence of remarkable intergranular corrosion (Figure 6b–e) as well as slight dissolution of the tungsten grains (Figure 6f). The intergranular corrosion at high flow velocity (2 ms^{-1}) was serious, accompanied by the formation of deep groove and micro corrosion pits caused by grain exfoliation, indicating that a mechanical effect would promote intergranular corrosion, weakening the GBs cohesion and loosening the GBs, especially at the triple junction.

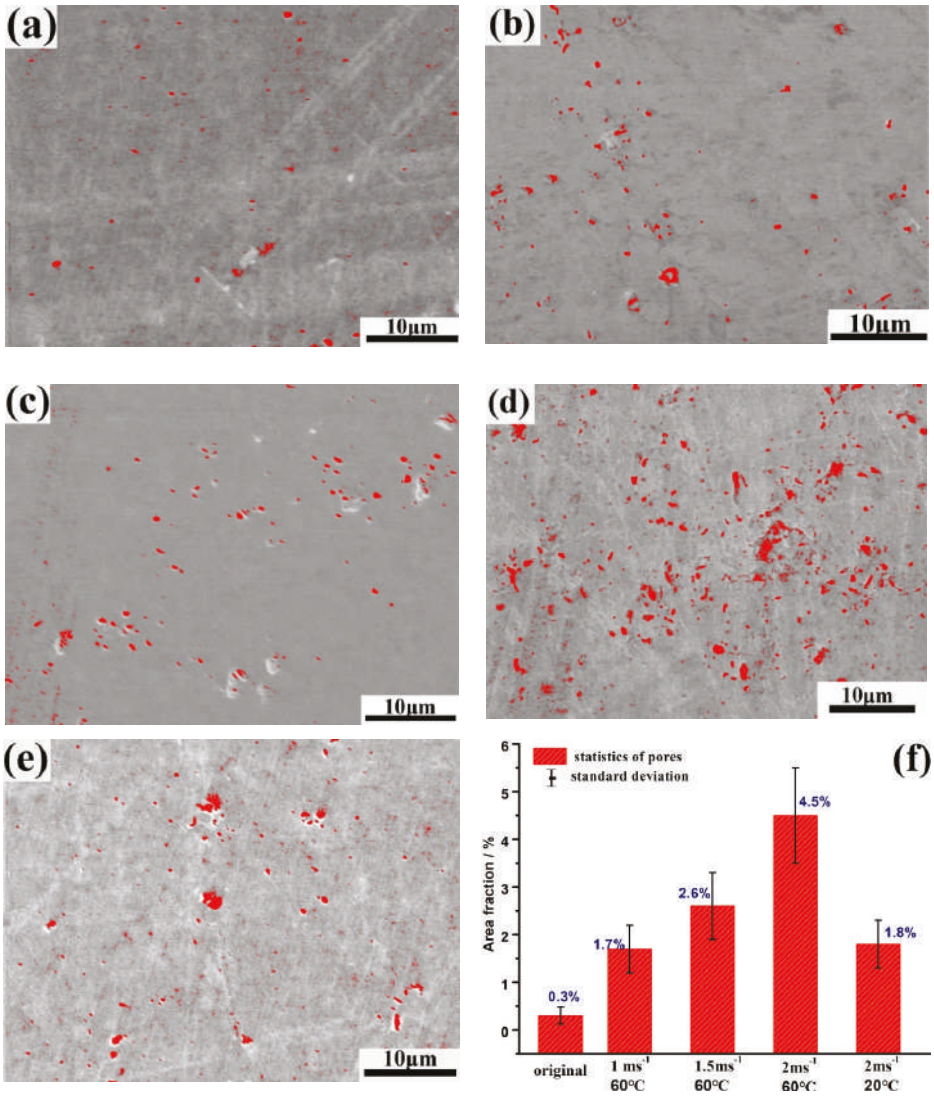

Figure 5. SEM image of the W–Cr–C coated tungsten samples (the red refers to the pores): (**a**) before corrosion; (**b**) corrosion at 1 ms^{-1}, 60 °C; (**c**) corrosion at 1.5 ms^{-1}, 60 °C; (**d**) corrosion at 2 ms^{-1}, 60 °C; (**e**) corrosion at 2 ms^{-1}, 20 °C; and (**f**) the bar chart of pitting fraction with velocity and temperature.

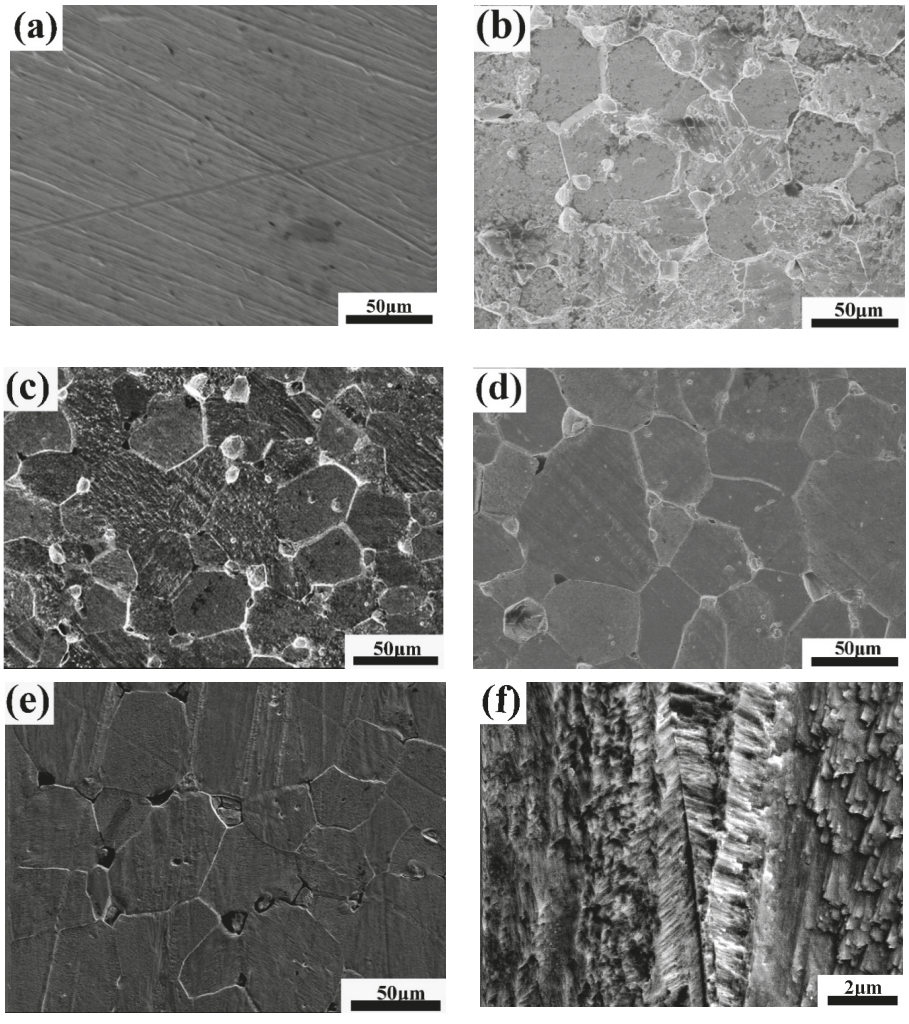

Figure 6. SEM images of bare tungsten: (**a**) before corrosion; (**b**) corrosion at 1 ms^{-1}, 60 °C; (**c**) corrosion at 1.5 ms^{-1}, 60 °C; (**d**) corrosion at 2 ms^{-1}, 60 °C; (**e**) corrosion at 2 ms^{-1}, 20 °C; and (**f**) corrosion on grains.

4. Discussion

Based upon the above results, the corrosion rate of W–Cr–C clad tungsten is much lower than that of bare tungsten due to the corrosion form changing from the intergranular corrosion of bare tungsten to the pitting corrosion of W–Cr–C coating. Pitting corrosion is a unique form of anodic reaction in the electrochemical reaction as well as a local corrosion. It causes less weight loss, so the change in corrosion rate with time gradually moves to a relatively steady state, as shown in Figures 3 and 4. The occurrence of pitting corrosion is known to be closely related to the environment and surface morphology and composition of materials. The medium used in this test containing special ions of oxygen and chlorine become the necessary trigger for pitting corrosion. In the service condition, chlorine and oxygen concentrations need to be controlled to reduce the pitting corrosion. Furthermore,

reducing the porosity of W–Cr–C coating by fine polishing will help decrease the nucleation sites of pitting.

Occurrence of the intergranular corrosion on tungsten is essentially induced by the impurities, as listed in Table 1. It was already understood that the impurities were prone to segregate at grain boundaries (GBs), which resulted in a large composition difference between the GBs and tungsten grains. The nonmetal impurities such as phosphorus, silicon, oxygen, nitrogen, and their compounds acted as intergranular embrittlement elements and mild acidic electrolyte. The impurities iron, aluminum, and silicon, due to lower potential than tungsten, became the anode, which constituted a corrosion cell with tungsten around and induced pitting corrosion at the GBs. With the exacerbation and development of pitting corrosion, it evolved into macroscopic corrosion along the GBs, namely electrochemically-driven intergranular corrosion. In the regions away from GBs, chemically driven dissolution of tungsten proceeds through the interaction with oxygen and water. Understandably, the dissolution rate at the grain boundary is much higher than that on the tungsten grains. Temperature has an accelerated effect on both types of dissolution.

Intergranular corrosion at the triple junction was much more remarkable. From the perspective of defects, the volume percentage of the GBs and defect density at a triple or multiple-junction are much larger than that at conventional GBs, so corrosion would occur more easily at such regions. From the aspect of interface energy, the corrosion behavior of fine grains at the trigeminal boundaries is analogous to the pinning behavior of the second particles occupying similar sites of matrix. The pinning interaction of the second particles with the matrix grains depends on the contact area of the particles with boundaries. The smaller the second particle, the less the boundary area is occupied. For particles with a smaller size, there is a stronger unpinning tendency of the boundaries because of the lower decreased interface energy [24]. Once the pits at the triple junction of GBs are produced, it leads to a noticeable change in weight. This accounts for the large fluctuations of the corrosion rate for tungsten.

Regardless of whether it is intergranular corrosion or pitting corrosion, the effect of flow velocity on corrosion is complex. When flow velocity is elevated, on one hand, corrosion might be further exacerbated on account of sufficient oxygen supply and dissolution of the underlying metal caused by accelerated mechanical damage; on the other hand, corrosion may also be retarded due to the replenishment of inhibitors (corrosion products) to some dead spaces (grooves or pores), which hinder further corrosion [25]. Thus, in the low flow velocity range, the competition between the above-mentioned two effects approaches a balance and the corrosion rate increases slowly with increasing flow velocity. However, when flow velocity exceeds a critical value, the protruding mechanical action overshadows the inhibitors replenishing, and the materials are allowed to deteriorate at a higher corrosion rate, for instance, the corrosion at 2 ms^{-1}.

Evidently, temperature imposes a greater and nearly liner impact in promoting intergranular and pitting corrosion than velocity within 60 °C. Increase in temperature caused the acceleration of ion mobility and a corresponding rise in electrochemical reaction activity. Despite this, there is a critical corrosion temperature for materials. For instance, the corrosion rate of iron begins to decrease above 80 °C [26], while the corrosion rate of P110 steel reaches the maximum at 60 °C and then decreases [27]. For tungsten and W–Cr–C coatings in this study, the critical temperatures should be higher than 60 °C. Therefore, in the service temperature range, temperature promoted the corrosion rate of both samples.

In the test duration, W–Cr–C endures less weight loss and corrosion rate than intergranular corrosion of tungsten, showing an expected protective role. However, it is worth pointing out that pitting corrosion occurred on the W–Cr–C layer. With an increase in time, the pores will grow gradually, and when the pores stretch to the W_2C layer, the columnar crystal structure of W_2C will lead the corrosion mechanism to change into intergranular corrosion, which is not conducive to protecting the substrate. Furthermore, the W_2C phase is less stable than WC in neutral solution [28]. Therefore, changing the microstructure of the W_2C layer and increasing the proportion of the W–Cr–C layer by adjusting the carburizing parameters is the topic of ongoing work.

5. Conclusions

This work studied the corrosion behavior of tungsten, with and without W–Cr–C cladding prepared by the SPS technique, in a flowing water system, and the main results can be concluded as the follows:

(1) The commercial bare tungsten showed an electrochemically-driven type of intergranular corrosion, with a larger corrosion rate due to impurities segregated at the grain boundaries. After W–Cr–C cladding, the corrosion rate of tungsten dropped significantly due to the change of corrosion type from intergranular corrosion to pitting corrosion.

(2) The simultaneous increase of water temperature and flow velocity accelerated corrosion of the samples with and without the W–Cr–C cladding. The corrosion rate of the W–Cr–C coating was slower than that of tungsten under the same parameters, demonstrating its better corrosion-erosion resistance than that of pure tungsten.

Author Contributions: Data Curation and Formal Analysis, Z.X.; Methodology, J.Y.; Writing—original draft, J.Y.; Writing—review & editing, Y.J. and Q.F. All authors have read and agreed to the published version of the manuscript.

Funding: This research was funded by the National Key Research and Development Program of China (Grant No. 2017YFA0402800), the National Natural Science Foundation of China (Grant Nos. 51601189, 11674319, 11475216), the Central Government Guides Local Science and Technology Development Projects (2019ZYD026), and the Sichuan Key Laboratory of Comprehensive Utilization of Vanadium and Titanium Resources (2018FTSZ44).

Acknowledgments: The authors sincerely thank the National Natural Science Foundation of China for their support of this work.

Conflicts of Interest: The authors declare no conflicts of interest.

References

1. Zhang, J.J.; Yan, Q.W.; Zhang, C. Recent Progress of the Project of the Chinese Spallation Neutron Source. *J. Neutron Res.* **2005**, *13*, 11–14. [CrossRef]
2. Yan, Q.W.; Yin, W.; Yu, B.L. Optimized concept design of the target station of Chinese spallation neutron source. *J. Nucl. Mater.* **2005**, *343*, 45–52. [CrossRef]
3. Kawai, M.; Furusaka, M.; Kikuchi, K.; Kurishita, H.; Watanabe, R.; Li, J.F.; Sugimoto, K.; Yamamura, T.; Hiraoka, Y.; Abe, K. R&D of A MW-class solid-target for a spallation neutron source. *J. Nucl. Mater.* **2003**, *318*, 38–55.
4. Kawai, M.; Kikuchi, K.; Kurishita, H.; Li, J.F.; Furusaka, M. Fabrication of a tantalum-clad tungsten target for KENS. *J. Nucl. Mater.* **2001**, *296*, 312–320. [CrossRef]
5. Noji, N.; Kashiwagura, K.; Akao, N. Corrosion resistance of tungsten and tungsten alloys for spallation target in stagnant and flowing water. *J. Jpn. Inst. Met.* **2002**, *66*, 1107–1115. [CrossRef]
6. Maloy, S.A.; Lillard, R.S.; Sommer, W.F.; Butt, D.P.; Gac, F.D.; Willcutt, G.J.; Louthan, M.R., Jr. Water corrosion measurements on tungsten irradiated with high energy protons and spallation neutrons. *J. Nucl. Mater.* **2012**, *431*, 140–146. [CrossRef]
7. Nelson, A.T.; O'Toole, J.A.; Valicenti, R.A.; Maloy, S.A. Fabrication of a tantalum-clad tungsten target for LANSCE. *J. Nucl. Mater.* **2012**, *431*, 172–184. [CrossRef]
8. Yu, Q.Z.; Lu, Y.L.; Hu, Z.L.; Zhou, B.; Yin, W.; Liang, T.J. Decay heat calculations for a 500 kW W-Ta spallation target. *Nucl. Instrum. Methods B* **2015**, *351*, 41–45. [CrossRef]
9. Nio, D.; Ooi, M.; Takenaka, N.; Furusaka, M.; Kawai, M.; Mishima, K.; Kiyanagi, Y. Neutronics performance and decay heat calculation of a solid target for a spallation neutron source. *J. Nucl. Mater.* **2005**, *343*, 163–168. [CrossRef]
10. Espallargas, N.; Berget, J.; Guilemany, J.; Benedetti, A.V.; Suegama, P. Cr_3C_2–NiCr and WC–Ni thermal spray coatings as alternatives to hard chromium for erosion–corrosion resistance. *Surf. Coat. Technol.* **2008**, *202*, 1405–1417. [CrossRef]

11. Alzouma, O.M.; Azman, M.-A.; Yung, D.-L.; Fridrici, V.; Kapsa, P. Influence of different reinforcing particles on the scratch resistance and microstructure of different WC–Ni composites. *Wear* **2016**, *352*, 130–135. [CrossRef]
12. Chen, J.; Liu, W.; Deng, X.; Wu, S. Tool life and wear mechanism of WC–5TiC–0.5VC–8Co cemented carbides inserts when machining HT250 gray cast iron. *Ceram. Int.* **2016**, *42*, 10037–10044. [CrossRef]
13. Zhang, D.Q.; Liu, T.; Joo, H.G.; Gao, L.X.; Lee, K.Y. Microstructure and corrosion resistance of the brazed WC composite coatings in aerated acidic chloride media. *Int. J. Refract. Met. Hard Mater.* **2012**, *35*, 246–250. [CrossRef]
14. He, Y.Z.; Si, S.H.; Xu, K.; Yuan, X.M. Effect of Cr_3C_2 Particles on Microstructure and Corrosion-Wear Resistance of Laser Cladding Co-based Alloy Coating. *Chin. J. Lasers* **2004**, *31*, 1143–1148.
15. Durst, O.; Ellermeier, J.; Trossmann, T.; Berger, C. Erosion corrosion of graded chromium carbide coatings in multi layer structure. *Materialwiss. Werkstofftech.* **2009**, *40*, 756–768. [CrossRef]
16. Gao, J.X.; Fan, J.L. Research developments on the binderless WC-based cemented carbide. *China Tungsten Ind.* **2011**, *26*, 22–26.
17. Jiang, Y.; Yang, J.F.; Zhuang, Z.; Liu, R.; Zhou, Y.; Wang, X.P.; Fang, Q.F. Characterization and properties of tungsten carbide coatings fabricated by SPS technique. *J. Nucl. Mater.* **2013**, *433*, 449–454. [CrossRef]
18. Jiang, Y.; Yang, J.F.; Xie, Z.M.; Gao, R.; Fang, Q.F. Corrosion resistance of W–Cr–C coatings fabricated by spark plasma sintering method. *Surf. Coat. Tech.* **2014**, *254*, 202–206. [CrossRef]
19. Jiang, Y.; Yang, J.F.; Fang, Q.F. Effect of chromium content on microstructure and corrosion behavior of W-Cr-C coatings prepared on tungsten substrate. *Front. Mater. Sci.* **2015**, *9*, 77–84. [CrossRef]
20. Du, J.H. The thermal design of tungsten target for 100 kW neutron spallation source. *Mach. Des. Manuf.* **2008**, *10*, 86.
21. Tan, J.; Zhou, Z.J.; Liu, Y.Q.; Qu, D.D.; Zhong, M.; Ge, C.C. Effect of carbon nanotubes on the microstructure and mechanical properties of W. *Acta Metall. Sin.* **2011**, *47*, 1555–1560.
22. Kurlov, A.S.; Gusev, A.I. Tungsten carbides and W-C phase diagram. *Inorg. Mater.* **2006**, *42*, 121–127. [CrossRef]
23. Guzanová, A.; Brezinová, J.; Draganovská, D.; Maruschak, P.O. Properties of coatings created by HVOF technology using micro-and nano-sized powder. *Koroze A Ochr. Mater.* **2019**, *63*, 86–93. [CrossRef]
24. Grácio, J.J.; Picu, C.R.; Vincze, G.; Mathew, N.; Schubert, T.; Lopes, A.; Buchheim, C. Mechanical behavior of Al-SiC nanocomposites produced by ball milling and spark plasma sintering. *Metall. Mater. Trans. A* **2013**, *44*, 5259–5269. [CrossRef]
25. Copson, H.R. Effect of velocity on corrosion by water. *Ind. Eng. Chem.* **1952**, *44*, 1745–1752. [CrossRef]
26. Revie, R.W. *Corrosion and Corrosion Control*, 4th ed.; John Wiley & Sons: Hoboken, NJ, USA, 2008.
27. Zhu, S.D.; Yin, Z.F.; Bai, Z.Q.; Wei, J.F.; Zhou, G.S.; Tian, W. Influences of temperature on corrosion behavior of P110 steel. *J. Chin. Soc. Corros. Prot.* **2009**, *29*, 493–497.
28. Weidman, M.C.; Esposito, D.V.; Hsu, Y.C.; Chen, J.G. Comparison of electrochemical stability of transition metal carbides (WC, W2C, Mo2C) over a wide pH range. *J. Power Sources* **2012**, *202*, 11–17. [CrossRef]

materials

MDPI

Article

Investigations of the Deuterium Permeability of As-Deposited and Oxidized Ti_2AlN Coatings

Lukas Gröner [1,*], Lukas Mengis [2], Mathias Galetz [2], Lutz Kirste [3], Philipp Daum [1], Marco Wirth [1], Frank Meyer [1], Alexander Fromm [1], Bernhard Blug [1] and Frank Burmeister [1]

1 Department of Tribology, Fraunhofer-Institut für Werkstoffmechanik IWM, Woehlerstrasse 11, 79108 Freiburg, Germany; philipp.daum@iwm.fraunhofer.de (P.D.); marco.wirth@iwm.fraunhofer.de (M.W.); frank.meyer@iwm.fraunhofer.de (F.M.); alexander.fromm@iwm.fraunhofer.de (A.F.); bernhard.blug@iwm.fraunhofer.de (B.B.); frank.burmeister@iwm.fraunhofer.de (F.B.)

2 Department of High Temperature Materials, DECHEMA-Forschungsinstitut, Theodor-Heuss-Allee 25, 60486 Frankfurt am Main, Germany; lukas.mengis@dechema.de (L.M.); mathias.galetz@dechema.de (M.G.)

3 Department of Epitaxy, Fraunhofer-Institut für Angewandte Festkörperphysik IAF, Tullastraße 72, 79108 Freiburg, Germany; lutz.kirste@iaf.fraunhofer.de

* Correspondence: lukas.groener@iwm.fraunhofer.de; Tel.: +49-761-5142-488

Received: 31 March 2020; Accepted: 23 April 2020; Published: 1 May 2020

Abstract: Aluminum containing $M_{n+1}AX_n$ (MAX) phase materials have attracted increasing attention due to their corrosion resistance, a pronounced self-healing effect and promising diffusion barrier properties for hydrogen. We synthesized Ti_2AlN coatings on ferritic steel substrates by physical vapor deposition of alternating Ti- and AlN-layers followed by thermal annealing. The microstructure developed a {0001}-texture with platelet-like shaped grains. To investigate the oxidation behavior, the samples were exposed to a temperature of 700 °C in a muffle furnace. Raman spectroscopy and X-ray photoelectron spectroscopy (XPS) depth profiles revealed the formation of oxide scales, which consisted mainly of dense and stable α-Al_2O_3. The oxide layer thickness increased with a time dependency of $\sim t^{1/4}$. Electron probe micro analysis (EPMA) scans revealed a diffusion of Al from the coating into the substrate. Steel membranes with as-deposited Ti_2AlN and partially oxidized Ti_2AlN coatings were used for permeation tests. The permeation of deuterium from the gas phase was measured in an ultra-high vacuum (UHV) permeation cell by mass spectrometry at temperatures of 30–400 °C. We obtained a permeation reduction factor (PRF) of 45 for a pure Ti_2AlN coating and a PRF of ~3700 for the oxidized sample. Thus, protective coatings, which prevent hydrogen-induced corrosion, can be achieved by the proper design of Ti_2AlN coatings with suitable oxide scale thicknesses.

Keywords: MAX phase; Ti_2AlN; PVD coating; oxidation; hydrogen permeation

1. Introduction

The increasing number of applications in which hydrogen is being used as a storage medium in energy conversion technologies demands the consideration of new construction materials, or at least a profound surface conditioning of established materials to prevent, e.g., hydrogen diffusion induced embrittlement or other forms of corrosion, especially the development of so-called "white etching cracks" [1]. One route for corrosion protection is the development and application of temperature-resistant coatings with excellent barrier properties for hydrogen. Recently performed studies indicate that MAX phase materials might fulfill these requirements [2–6]. The general formula, $M_{n+1}AX_n$, (short MAX) describes a family of materials consisting of an early transition metal (M), mostly a group 13 or 14 element (A) and nitrogen and/or carbon (X) with the stoichiometry of n = 1,2,3 [7].

The MAX phases crystallize in a hexagonal lattice within the space group D46h (P63/mmc) in which the octahedral $M_{n+1}X_n$ layers are separated by atomic monolayers of pure A-atoms. MAX phase materials are known to have a good oxidation resistance [3,8,9], a high damage tolerance as well as a high electrical and thermal conductivity [10].

The good oxidation resistance of Al containing MAX phases usually stems from the formation of dense and thermodynamically stable thermal grown oxides (TGO) consisting of α-Al_2O_3 on the coatings surface at relatively low temperatures of 600–700 °C. For comparison, the direct physical vapor deposition (PVD) of an α-Al_2O_3 in an industrial scale deposition process usually requires temperatures above 1000 °C [11]. Lower deposition temperatures of 500–600 °C have also been observed but at the expense of a brittle fracture behavior [12,13]. A further advantage of α-Al_2O_3 oxide scales thermally grown on MAX phase coatings is the well-known self-healing effect whereby small defects or cracks in the coating, which might serve as diffusion pathways, are blocked by oxide growth [2]. For this purpose, the oxidation kinetics of the TGO has to allow for a quick healing and oxidation of the surface, but has to prevent fast oxygen diffusion to the coating–substrate interface. The oxidation kinetics of Ti_2AlC at 1200 °C were modelled by G.M. Song et al. in [3]. This model contains the growth of oxide grains and assumes that the diffusion paths along the grain boundaries increase with time. This results in a time dependency for the increase in the thickness of the oxide scale $d_{Ox}(t)$ of:

$$d_{Ox}(t) = 2\sqrt{k_n} \times t^{1/4} \quad (1)$$

The growth factor $k_n = \Omega D_{GB} \Delta C \frac{3\delta}{d_0}$ contains a constant prefactor Ω, the diffusion coefficient for oxygen along the grain boundaries D_{GB}, the size of the grain boundaries δ, the initial lateral grain size d_0 and the gradient in the oxygen concentration ΔC.

This model of α-Al_2O_3-formation, as well as the structural properties of MAX phases, i.e., the sequence of dense MX-layers, motivated the present investigation on their barrier properties against hydrogen diffusion.

Although little information about the diffusion of hydrogen in MAX phases exists, similarly composed carbides or nitrides of early transition metals are already used as diffusion barriers for hydrogen [4,14]. It is expected that the anisotropic structure of MAX phases will induce a directional anisotropy of the hydrogen diffusion. In [5], F. Colonna and C. Elsässer presented the findings of an atomistic simulation of diffusion processes in Ti_2AlN using density-functional theory (DFT). Therein, interstitial diffusion paths of hydrogen and oxygen were examined. It was found that, for hydrogen, the migration perpendicular to the basal planes has a maximum barrier of ~3 eV, whereas the migration barrier parallel to the basal plane is one order of magnitude lower. The high migration barrier parallel to the c axis was explained by the presence of the Ti_2N double layer, where the interstitial octahedral sites of Al_3Ti_3 are already occupied by nitrogen atoms.

An experimental study on the hydrogen barrier properties of MAX phase coatings was presented by C. Tang et al. in [6]. Therein, ZrY-4 alloy cylinders were coated with Ti_2AlC and Cr_2AlC by a multilayer deposition followed by a subsequent annealing step. This process led to a {0001}-textured polycrystalline growth which could also be detected in [15] for Ti_2AlN. After loading the specimens in an Ar+H_2 atmosphere the cylinders were investigated by neutron radiography. It could be shown that a 5 µm thick Ti_2AlC and Cr_2AlC reduced the penetration of hydrogen under the detection limit.

To evaluate coatings in terms of their capability to reduce the hydrogen permeation a permeation reduction factor (PRF) can be calculated using the mass specific ion current j:

$$\mathrm{PRF} = \frac{j_{uncoated}}{j_{coated}}. \quad (2)$$

D. Levchuk et al. investigated Al-Cr-O coatings [16] and Er_2O_3 coatings [17] as hydrogen permeation barrier. Both coatings tend to form a dense crystalline structure, which is capable of effectively reducing the hydrogen permeation up to a PRF(Al-Cr-O) = 3500 and PRF(Er_2O_3) = 800.

2. Experimental Details

2.1. Deposition of Ti_2AlN

The Ti_2AlN MAX coatings were deposited on AISI 430 ferritic stainless-steel substrates (Fe81/Cr17/Mn/Si/C/S/P), which were polished (1400 grit) and cleaned in acetone and isopropanol using an ultrasonic bath prior to deposition. A custom build industrial sized magnetron sputter chamber SV400/S3 (FHR Anlagenbau GmbH, Ottendorf-Okrilla, Germany) equipped with rectangular titanium (purity 99.8%) and aluminum targets (99.999%) was utilized. To obtain a pronounced {0001}-texture with a parallel orientation of the basal planes and the substrate surface, we alternately deposited 150 single layers of Ti and AlN on the substrate, beginning with Ti. During the radio frequency-sputtering of the aluminum target, nitrogen (purity 99.9999%) was introduced in the chamber. A final subsequent annealing at 700 °C for 1 h in vacuum led to the formation of textured Ti_2AlN MAX phase coatings. Details of the deposition process are described elsewhere [15]. The coatings thickness was in the 2 µm–3 µm range.

2.2. Oxidation Procedure and Analysis

To investigate the oxidation kinetics of the Ti_2AlN coatings, comparable samples originating from the same batch were oxidized at 700 °C for 5 h, 10 h, 20 h and 100 h in a muffle furnace (Nabertherm GmbH, Lilienthal, Germany) in air. The samples were afterwards removed from the furnace and cooled in air. The crystallographic orientation and phase composition of oxidized and non-oxidized coatings were investigated by X-ray diffractometry (XRD) using a PANalytical Empyrean in parallel beam geometry (Empyrean, PANalytical, Almelo, The Netherlands) and Cu $K\alpha_1$ radiation with a 2-bounce Ge 220 monochromator. The samples were irradiated with primary X-rays using a line focus. The diffracted X-rays were detected using a PIXel-3D detector with a 1 mm slit for the phase analysis.

A surface sensitive phase analysis was performed using a confocal Raman spectrometer (Model inVia, Renishaw plc., Gloucestershire, United Kingdom) in backscatter geometry. The excitation wavelength $\lambda_{Nd:YAG}$ = 532 nm was used to determine possible changes in the Ti_2AlN phase upon thermal treatment whereas the wavelength λ_{HeNe} = 633 nm proofed to be suitable for exciting fluorescence bands in the thermally grown AlO_x phase. In all measurements, a 100-fold objective focused the laser on the surface to a spot diameter of about 2 µm.

XPS depth profiles were recorded with a PHI 5000 VersaProbe II (Ulvac-PHI, Inc., Chigasaki, Japan) equipped with an argon sputter option using Al Kα-rays. For analyzing the coarse elemental distribution close to the interface of coating and substrate a metallographic cross-section was prepared after an electrochemical deposition of Ni for protective purposes. The electron probe micro analysis (EPMA) was performed utilizing a JXA-8100 (Jeol, Akishima, Japan). The measurements were performed with an acceleration voltage of 15 kV and a dwell time of 30 ms.

2.3. Deuterium Permeation Setup

To investigate the diffusion of deuterium from the gas phase through coated and oxidized membranes, a permeation setup was developed following the works of C. Frank et al. [18], J. Gorman et al. [19] and D. Levchuk et al. [20]. The test rig consisted of two chambers separated by a thin steel membrane (see Figure 1). The high pressure side is filled with the diffusional species or the purging gas, the low pressure side is evacuated by a turbomolecular pump and an ion getter pump down to pressures of ~10^{-6} Pa. The latter is also equipped with a quadrupole mass spectrometer (Model PrismaPlus™ QMG 220, Pfeiffer Vacuum Technology AG, Aßlar, Germany) to determine the gas composition as well as the mass and time dependent ion current, which is detected by a secondary electron multiplier. With infrared transmissible windows on both sides, the membrane was heated by a focused halogen radiation heater and the temperature as well as the temperature distribution was recorded by a heat sensitive camera. The membranes, illustrated in Figure 1b, were water jet cut (Ø = 30 mm) from a 0.2 mm thick steel foil (AISI 430) and coated as described before. The uncoated

back sides were corundum blasted to increase the absorption of infrared radiation. The membrane was mounted with conical copper gaskets with the coating facing the high pressure side. After a minimum base pressure of 1×10^{-5} Pa was reached, the measurement was started.

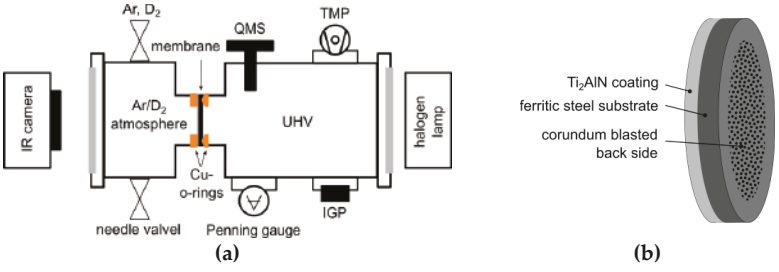

Figure 1. (**a**) Schematic illustration of the hydrogen permeation test rig with quadrupole mass spectrometer (QMS), turbomolecular pump (TMP) and ion getter pump (IGP). (**b**) Schematic illustration of the coated ferritic steel membrane.

To investigate the hydrogen barrier properties, the isotope deuterium was employed in order to avoid interpretation ambiguities due to contaminations with residual gases or water molecules. The permeation measurements were performed close to thermodynamic equilibrium. First, deuterium was injected on the atmospheric pressure side. Then the membrane temperature was set to a maximum and was reduced stepwise when a constant ion current was reached. The ion current of the atomic mass $m(D_2) = 4$ was recorded. The permeation reduction factor was calculated by (2) using the steady state values of the ion currents of a non-coated sample as a reference.

3. Results and Discussion

3.1. Oxidation

To investigate the influence of the oxygen exposure at high temperatures on the phase composition, XRD diffractograms were recorded for different exposure times and compared to the pristine sample. In Figure 2a, the diffractogram of the as-synthesized coating reveals an almost phase pure Ti_2AlN coating having a strong {0001}-texture. The peak at 42.5° is attributed to the (200) lattice plane of TiN. The Fe-bcc peaks at 44.6° and 65.0° are assigned to the steel substrate. Diffractograms of the oxidized samples are depicted in Figure 2 with an offset for better visibility.

These phase compositions appear almost unaltered upon thermal exposure. Only in the 2Θ-region between 42°–43° a slight change in the peak position is visible. This region is depicted in detail in Figure 2b. Due to broad peak widths and weak angle dependent interferences, the signals from TiN and α-Al_2O_3 cannot be clearly distinguished. Further ambiguities arise due to the small TGO layer thickness and its possibly amorphous structure. Hence, further surface sensitive Raman analysis was performed (see Figure 3). The Raman spectra of the coatings in Figure 3a still feature the characteristic Raman peaks for Ti_2AlN despite the oxidized surface, though an increase in the background is detected. The broad background and the peak between 500 cm^{-1}– 600 cm^{-1} might stem from the formation of surface oxides and/or oxycarbides [21] as well as from the formation of TiN close to the surface due to Al depletion [22]. Titanium oxides like anatase and rutile, which were reported in [23] after the oxidation of Ti_2AlN coatings at 750 °C, are not detected.

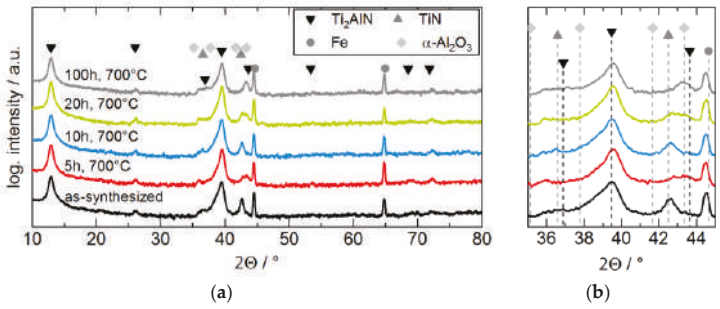

Figure 2. XRD diffractograms of as-synthesized and oxidized Ti_2AlN coatings on ferritic steel samples: (**a**) overview and (**b**) enlarged region around $2\theta° \approx 40°$.

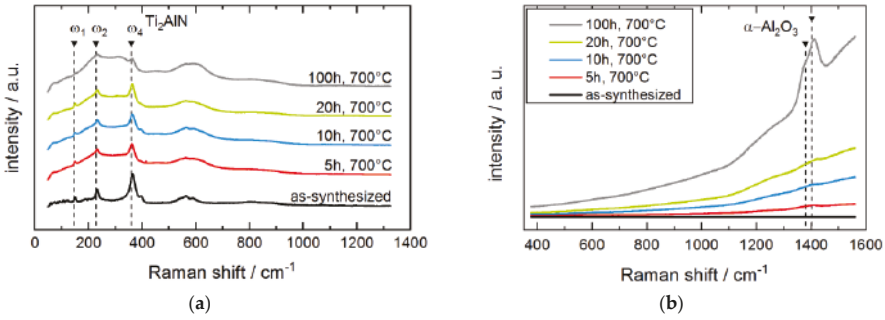

Figure 3. (**a**) Raman spectra ($\lambda_{Nd:YAG}$ = 532 nm) of the Ti_2AlN coatings before and after oxidation. (**b**) Raman fluorescence spectra (λ_{HeNec} = 633 nm) of the Ti_2AlN coatings before and after oxidation.

The fluorescence spectra in Figure 3b exhibit an increase in the background with an increasing oxidation time. Particularly after 100 h of oxidation, the formation of distinct peaks close to 1379 cm^{-1} and 1402 cm^{-1} can be detected. According to literature, these peaks are attributed to the fluorescence of Cr^{3+} and Fe^{3+} impurities in an α-Al_2O_3 environment [24–26].

After oxidation, XPS depth profiles of all coatings were created by convoluting the distribution of the binding energies. The underlying XPS spectra are not shown herein. In Figure 4 profiles of a sample oxidized for 100 h (a) and of an uncoated substrate (b) are presented for comparison. In the case of the MAX phase coating Figure 4a, oxidic Al2p bonds with a maximum in the energy of 74.3 eV were detected and ascribed to the formation of Al_2O_3 at the sample surface. To a smaller extend of about 8 at%, oxidic Ti2p bonds with a maximum in the energy of 458.2 eV were detected, which were distributed over two regional maxima located in a depth of ~45 nm in the Al_2O_3 scale and at the interface of Ti_2AlN/TGO. At the interface, the shift of the Ti2p-signal to nitridic binding energies of 454.3 eV and the shift of the Al2p-signal to metallic binding energies of 72.3 eV revealed the transition to the Ti_2AlN phase. With only ~16 at% of Al2p bonds and sustaining increasing signals at a depth of 200 nm, a transition regime close to the interface is observed where an Al depletion exists. The thickness d_{Ox} of the TGO scale was determined by the decrease of the O1s signal, and set to the sputter depth where the O-signal fell below 50% of the original ratio.

The numerical fit of the values for d_{Ox} according to (1) is plotted in Figure 5. The errors of the oxide thicknesses were estimated to 10 nm resulting from a temporal variation in the sputter rate during XPS measurements. The growth factor of the TGO was calculated to $k_n = 402 \pm 17 \frac{\text{mol}}{\text{m×s}}$ with a quality factor of $R^2 = 0.9794$. The quality of the fit argues for the suitability of the mathematical description by (1 for the oxidation kinetics. However, no conclusion can be drawn so far as to whether

the O or the Al diffuses along the grain boundaries to the oxidizing interface according to the above described model of G.M. Song et al.

The spectra of an uncoated ferritic steel substrate after 100h at 700 °C in Figure 4b revealed the formation of a TGO consisting of of Cr-, Mn- and Fe-oxides. The thickness of the TGO was calculated to 540 nm, which compares to approximately 100 nm in the case of a coated substrate.

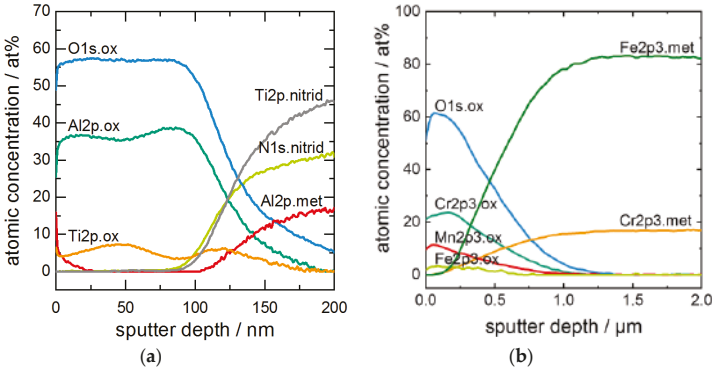

Figure 4. XPS depth profiles after oxidation for 100 h at 700 °C of (**a**) Ti_2AlN coating, and (**b**) uncoated ferritic steel substrate.

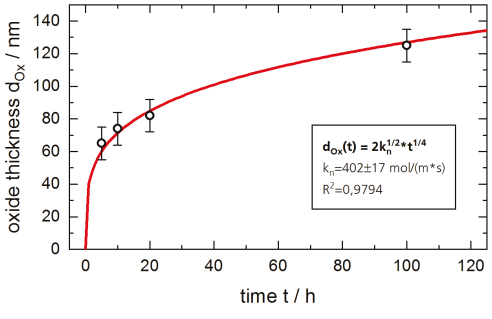

Figure 5. Measured oxide thicknesses by XPS depth profiles of the Ti_2AlN coatings after oxidation. Underlying fit was performed using (1).

The EPMA images of the sample oxidized for 100 h at 700 °C depicted in Figure 6 represent the elemental distributions of Ti (b), Al (c), N (d), O (e), Ni (f) and Fe (g), where the colors indicate the normalized elemental concentration. The measured distribution of Ti, Al and N across the coating thickness features a depletion in Ti and Al at the interface of Ti_2AlN/TGO and in the subsurface region. Accordingly, the substrate is locally enriched by Al and N and the formation of precipitates perpendicular to the surface is visible. In such areas, only a minor Fe-concentration is measured, as the microprobe signal is always to normalized 100% for all elements. The inward diffusion of Al and N is accompanying the outward diffusion of Fe into the coating according to the Fe elemental distribution map. Besides the thin oxide scale, which formed on top of the MAX phase coating, oxygen can be detected within the Ni-plating. This is caused by the formation of a longitudinal crack within the Ni-plating during the preparation of the cross-section.

The strong interdiffusion of the weakly bound A-element of MAX phases with the substrate is known to be a crucial aspect, when it comes to the chemical stability in high temperature applications [23]. Therefore, the interdiffusion should be suppressed by applying additional barrier films against Al diffusion between the substrate and coating. Further loss of the A-element also occurs during oxidation

and annealing in vacuum due to Al_2O_3 formation and evaporation. In [27], Zhang et al. calculated that the Ti_2AlN MAX phase lattice structure is capable of accommodating Al vacancies down to a $Ti_2Al_{0.75}N$ stoichiometry.

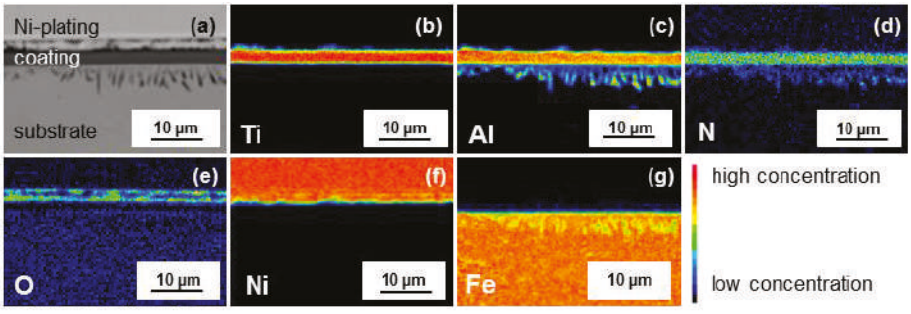

Figure 6. Scanning electron microscope image (**a**) and electron probe micro analysis (EPMA) scans of the cross-section after oxidation for 100 h at 700 °C for Ti (**b**), Al (**c**), N (**d**), O (**e**), Ni (**f**) and Fe (**g**).

3.2. Hydrogen Permeation

The D_2 ion current was measured by secondary ion mass spectrometry using the setup illustrated in Figure 1. The influence of the coatings on the permeation was investigated in a state close to the thermodynamic equilibrium. Three different membranes were investigated: the uncoated substrate material (substrate), the substrate coated with 2.7 µm of Ti_2AlN (substrate+Ti_2AlN) and the substrate coated with 2.7 µm of Ti_2AlN with a subsequent oxidation for 20 h at 700 °C (substrate+Ti_2AlN+TGO). In Figure 7, the D_2 ion currents are plotted in the temperature range from about 50 °C to 400 °C. Three measuring cycles were performed for each membrane. The results of the different cycles are denoted by the different symbols in the graph (square, circle and triangle). The small variance in the data points confirms the reproducibility of the permeation induced ion current.

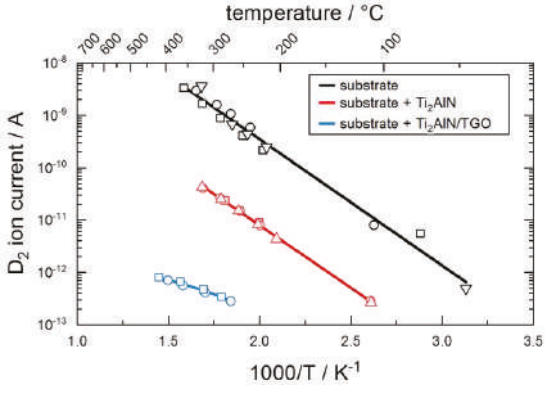

Figure 7. Arrhenius Plot of D_2 ion currents of ferritic membranes with and without Ti_2AlN or Ti_2AlN+thermal grown oxide (TGO) coating. The different symbols on each line refer to results of consecutive measuring cycles. The quasi-linear fit is performed to illustrate the Arrhenius type behavior.

The diffusion through all three membranes follows an Arrhenius type behavior, which confirms the assumption of a diffusion-controlled permeation. The deposition of a 2.7 µm thick Ti_2AlN coating already reduces the permeation of deuterium. The PRF at 300 °C is calculated to a factor of 45. As optical investigations on the coating after the measurements still revealed some minor cracks in the

coating, the PRF might still be lower for a defect-free MAX-phase coating. However, the formation of the oxide scale leads to a further, significant reduction of the permeation. With an oxidation of the coated steel membrane for 20 h at 700 °C, the formation of TGO of 80 nm thickness is expected, compare Figure 5. With respect to the uncoated steel membrane, a PRF of about 3700 was achieved. This reduction can be explained by the low solubility of hydrogen in the α-Al_2O_3 phase as well as by the potential healing of small defects in Ti_2AlN, which blocks alternative migration paths with low energy barriers. The reduction of three orders of magnitude strongly supports the initially assumed suitability of Ti_2AlN coatings as high temperature hydrogen diffusion barriers.

4. Conclusions and Outlook

Ti_2AlN coatings were synthesized on ferritic steel samples by a repeated deposition of Ti/AlN double layers and a subsequent annealing in vacuum. The oxidation experiments at 700 °C in air revealed the formation of a thin TGO at the sample surface consisting mainly of α-Al_2O_3. By analyzing the thickness of the TGO, the kinetic confirms the findings of G.M. Song et al., which are described by a growth in thickness with a time dependency of $\sim t^{1/4}$. Thereby, a thin protective oxide is quickly formed after exposure to air but further growth is strongly hindered by a slow diffusion of migrating particles through the dense oxide. It was shown that the TGO not only serves as an effective protective layer against further oxidation, but also serves as a diffusion barrier against hydrogen. Whereas a 2.7 µm thin Ti_2AlN coating reduces the permeation of deuterium to a factor of 45, the formation of an α-Al_2O_3 scale further reduces the permeation within three orders of magnitude. The healing of coating defects like pores and cracks at elevated temperatures upon oxidation is seen as an additional advantage of thermally grown diffusion barriers in comparison to directly deposited barrier coatings.

Further investigations need to focus on the interdiffusion process at the interface of coating and substrate in order to reduce the loss of the Al, which is required for the formation of α-Al_2O_3. Finding an optimum thickness of the TGO, which significantly reduces the hydrogen permeation and at the same time exhibits a sufficient thermal and mechanical stability is the crucial task for the utilization of Ti_2AlN as protective coatings in industrial applications.

In summary, Al containing MAX phase coatings, which tend to form a dense α-Al_2O_3 on the surface upon oxidation, seems to be effective protective coatings in high temperature applications, where oxygen and hydrogen corrode the substrate material.

Author Contributions: Conceptualization, L.G.; investigation, L.K., L.M., P.D. and L.G.; technical support, M.W.; writing—original draft preparation, L.G.; writing—review and editing, L.M., M.G., F.M. and B.B.; supervision, F.B.; funding acquisition, A.F. and F.B. All authors have read and agreed to the published version of the manuscript.

Funding: Financial support by the Baden-Württemberg-Stiftung gGmbH in the context of "CleanTech" (project CT-6 "LamiMat") is gratefully acknowledged.

Conflicts of Interest: The authors declare no conflict of interest.

References

1. Evans, M.-H. An updated review: White etching cracks (WECs) and axial cracks in wind turbine gearbox bearings. *Mater. Sci. Technol.* **2016**, *32*, 1133–1169. [CrossRef]
2. Farle, A.-S.; Kwakernaak, C.; van der Zwaag, S.; Sloof, W.G. A conceptual study into the potential of $M_{n+1}AX_n$-phase ceramics for self-healing of crack damage. *J. Eur. Ceram. Soc.* **2015**, *35*, 37–45. [CrossRef]
3. Song, G.M.; Schnabel, V.; Kwakernaak, C.; van der Zwaag, S.; Schneider, J.M.; Sloof, W.G. High temperature oxidation behaviour of Ti_2AlC ceramic at 1200C. *Mater. High Temp.* **2012**, *29*, 205–209. [CrossRef]
4. Hultman, L. Thermal stability of nitride thin films. *Vacuum* **2000**, *57*, 1–30. [CrossRef]
5. Colonna, F.; Elsässer, C. First principles DFT study of interstitial hydrogen and oxygen atoms in the MAX phase Ti_2AlN. *RSC Adv* **2017**, *7*, 37852–37857. [CrossRef]
6. Tang, C.; Grosse, M.K.; Trtik, P.; Steinbrück, M.; Stüber, M.; Seifert, H.J. H_2 Permeation Behavior Of Cr_2AlC And Ti_2AlC MAX Phase Coated Zircaloy-4 By Neutron Radiography. *Acta Polytech.* **2018**, *58*, 69. [CrossRef]

7. Barsoum, M.W. The $M_{n+1}AX_n$ phases: A new class of solids. *Prog. Solid State Chem.* **2000**, *28*, 201–281. [CrossRef]
8. Smialek, J.L. Oxidation of Al_2O_3 Scale-Forming MAX Phases in Turbine Environments. *Met. Mat Trans A* **2017**, *89*, 334. [CrossRef]
9. Zhang, Z.; Jin, H.; Chai, J.; Pan, J.; Seng, H.L.; Goh, G.T.W.; Wong, L.M.; Sullivan, M.B.; Wang, S.J. Temperature-dependent microstructural evolution of Ti_2AlN thin films deposited by reactive magnetron sputtering. *Appl. Surf. Sci.* **2016**, *368*, 88–96. [CrossRef]
10. Sokol, M.; Natu, V.; Kota, S.; Barsoum, M.W. On the Chemical Diversity of the MAX Phases. *Trends Chem.* **2019**, in press. [CrossRef]
11. Laimer, J.; Fink, M.; Mitterer, C.; Störi, H. Plasma CVD of alumina—Unsolved problems. *Vacuum* **2005**, *80*, 141–145. [CrossRef]
12. Gavrilov, N.V.; Kamenetskikh, A.S.; Tretnikov, P.V.; Chukin, A.V. High-rate low-temperature PVD of thick 10 µm α-alumina coatings. *J. Phys. Conf. Ser.* **2019**, *1393*, 12082. [CrossRef]
13. Kyrylov, O.; Kurapov, D.; Schneider, J.M. Effect of ion irradiation during deposition on the structure of alumina thin films grown by plasma assisted chemical vapour deposition. *Appl. Phys. A* **2005**, *80*, 1657–1660. [CrossRef]
14. Checchetto, R.; Bonelli, M.; Gratton, L.M.; Miotello, A.; Sabbioni, A.; Guzman, L.; Horino, Y.; Benamati, G. Analysis of the hydrogen permeation properties of TiN-TiC bilayers deposited on martensitic stainless steel. *Surf. Coat. Technol.* **1996**, *83*, 40–44. [CrossRef]
15. Gröner, L.; Kirste, L.; Oeser, S.; Fromm, A.; Wirth, M.; Meyer, F.; Burmeister, F.; Eberl, C. Microstructural investigations of polycrystalline Ti_2AlN prepared by physical vapor deposition of Ti-AlN multilayers. *Surf. Coat. Technol.* **2018**, 166–171. [CrossRef]
16. Levchuk, D.; Bolt, H.; Döbeli, M.; Eggenberger, S.; Widrig, B.; Ramm, J. Al–Cr–O thin films as an efficient hydrogen barrier. *Surf. Coat. Technol.* **2008**, *202*, 5043–5047. [CrossRef]
17. Chikada, T.; Suzuki, A.; Yao, Z.; Levchuk, D.; Maier, H.; Terai, T.; Muroga, T. Deuterium permeation behavior of erbium oxide coating on austenitic, ferritic, and ferritic/martensitic steels. *Fusion Eng. Des.* **2009**, *84*, 590–592. [CrossRef]
18. Frank, R.C.; Swets, D.E.; Fry, D.L. Mass Spectrometer Measurements of the Diffusion Coefficient of Hydrogen in Steel in the Temperature Range of 25–90 °C. *J. Appl. Phys.* **1958**, *29*, 892–898. [CrossRef]
19. Gorman, J.K.; Nardella, W.R. Hydrogen Permeation through Metals. *Vacuum* **1962**, *12*, 19–24. [CrossRef]
20. Levchuk, D.; Koch, F.; Maier, H.; Bolt, H. Gas-driven Deuterium Permeation through Al_2O_3 Coated Samples. *Phys. Scr.* **2004**, *T108*, 119–123. [CrossRef]
21. Tang, C.; Klimenkov, M.; Jaentsch, U.; Leiste, H.; Rinke, M.; Ulrich, S.; Steinbrück, M.; Seifert, H.J.; Stueber, M. Synthesis and characterization of Ti_2AlC coatings by magnetron sputtering from three elemental targets and ex-situ annealing. *Surf. Coat. Technol.* **2017**, *309*, 445–455. [CrossRef]
22. Ines, D. Raman Spectroscopy Analysis of CVD Hard Coatings Deposited in the $TiC_{1-x}Nx$, $TiB_xC_yN_z$ and Ti-B-N System. Ph.D. Thesis, Eberhard Karls Universität Tübingen, Tübingen, Germany, 2011.
23. Wang, Z.; Li, X.; Li, W.; Ke, P.; Wang, A. Comparative study on oxidation behavior of Ti_2AlN coatings in air and pure steam. *Ceram. Int.* **2019**, *45*, 9260–9270. [CrossRef]
24. Aminzadeh, A. Excitation Frequency Dependence and Fluorescence in the Raman Spectra of Al_2O_3. *Appl. Spectrosc.* **1997**, *51*, 817–819. [CrossRef]
25. Wang, X.H.; Zhou, Y.C. Oxidation behavior of Ti_3AlC_2 powders in flowing air. *J. Mater. Chem.* **2002**, *12*, 2781–2785. [CrossRef]
26. Luo, M.-F.; Fang, P.; He, M.; Xie, Y.-L. In situ XRD, Raman, and TPR studies of CuO/Al_2O_3 catalysts for CO oxidation. *J. Mol. Catal. A Chem.* **2005**, *239*, 243–248. [CrossRef]
27. Zhang, Z.; Jin, H.; Pan, J.; Chai, J.; Wong, L.M.; Sullivan, M.B.; Wang, S.J. Origin of Al Deficient Ti2AlN and Pathways of Vacancy-Assisted Diffusion. *J. Phys. Chem. C* **2015**, *119*, 16606–16613. [CrossRef]